INFORMATION TO USERS

This manuscript has been reproduced from the microfilm master. UMI films the text directly from the original or copy submitted. Thus, some thesis and dissertation copies are in typewriter face, while others may be from any type of computer printer.

The quality of this reproduction is dependent upon the quality of the copy submitted. Broken or indistinct print, colored or poor quality illustrations and photographs, print bleedthrough, substandard margins, and improper alignment can adversely affect reproduction.

In the unlikely event that the author did not send UMI a complete manuscript and there are missing pages, these will be noted. Also, if unauthorized copyright material had to be removed, a note will indicate the deletion.

Oversize materials (e.g., maps, drawings, charts) are reproduced by sectioning the original, beginning at the upper left-hand corner and continuing from left to right in equal sections with small overlaps. Each original is also photographed in one exposure and is included in reduced form at the back of the book.

Photographs included in the original manuscript have been reproduced xerographically in this copy. Higher quality 6" x 9" black and white photographic prints are available for any photographs or illustrations appearing in this copy for an additional charge. Contact UMI directly to order.

UMI

A Bell & Howell Information Company
300 North Zeeb Road, Ann Arbor MI 48106-1346 USA
313/761-4700 800/521-0600

A POSITRON 2D-ACAR STUDY OF THE SILICON-DIOXIDE/SILICON INTERFACE AND THE POINT DEFECTS IN THE SEMI-INSULATING GaAs

by

Jianping Peng

A dissertation submitted to the Graduate Faculty in Physics in partial fulfillment of the requirement for the degree of Doctor of Philosophy, The City University of New York

1996

UMI Number: 9630496

UMI Microform 9630496
Copyright 1996, by UMI Company. All rights reserved.

This microform edition is protected against unauthorized copying under Title 17, United States Code.

UMI
300 North Zeeb Road
Ann Arbor, MI 48103

This manuscript has been read and accepted for the Graduate Faculty in Physics in satisfaction of the dissertation requirement for the degree of Doctor of Philosophy.

3/21/96
Date

Leonard. O. Roellig Leonard O. Roellig
Chair of Examining Committee

3/21/96
Date

Joseph B. Krieger Joseph B. Krieger
Executive Officer

Kelvin G. Lynn Kelvin G. Lynn

Martin A. Kramer Martin Kramer

Kurt H. Becker

Ken E. Miyano
Supervisory Committee

The City University of New York

ABSTRACT

A POSITRON 2D-ACAR STUDY OF THE SILICON-DIOXIDE/SILICON INTERFACE AND THE POINT DEFECTS IN THE SEMI-INSULATING GaAs

by

Jianping Peng

Advisors: Dr. Kelvin G. Lynn and Professor Leonard O. Roellig

The SiO_2-Si system has been the subject of extensive study for several decades. Particular interest has been paid to the interface between Si single crystal and the amorphous SiO_2 which determines the properties and performances of devices. This is significant because of the importance of Si technology in the semiconductor industry. The development of the high-intensity slow positron beam at Brookhaven National Laboratory make it possible to study this system for the first time using the positron two-dimensional angular correlation of annihilation radiation (2D-ACAR) technique. 2D-ACAR is a well established and is a non-destructive microscopic probe for studying the electronic structure of materials, and for doing the depth-resolved measurements. Some unique information was obtained from the measurements performed on the SiO_2-Si system: Positronium (Ps) atoms formation and trapping in microvoids in both oxide and interface regions; and positron annihilation at vacancy-like defects in the interface region which can be attributed to the famous P_b centers. The discovery of the microvoids in the interface region may have some impact on the fabrication of the next generation electronic devices.

Using the conventional 2D-ACAR setup with a ^{22}Na as positron source, we also studied the native arsenic (As) vacancy in the semi-insulating gallium-arsenide (SI-GaAs), coupled with *in situ* infrared light illumination. The defect spectrum was obtained by comparing the spectrum taken without photo-illumination to the spectrum taken with photo-illumination. The photo-illumination excited electrons from valence band to the defect level so that positrons can become localized in the defects.

The two experiments may represent a new direction of the application of positron 2D-ACAR technique on the solid state physics and materials sciences.

Acknowledgements

I would like to express my deep gratitude to my advisors Dr. Kelvin G. Lynn and Professor Loenard O. Roellig for their help in my four years of Ph.D research, especially to Dr. K. G. Lynn for his day-to-day guidance, support and help. It is impossible to finish this work without Dr. Lynn's help. I would like to thank Dr. P. Asoka-Kumar and Dr. B. Nielsen for their involvement in the SiO_2-Si experiment and invaluable discussion. Also, the invaluable discussion and encouragement from Dr. F. M. Jacobson are highly appreciated.

I would like to express my special thanks to my friend Mr. D. P. Becker, who passed away just by the end of this work, for his help in the vacuum system and assistance in building and running the high flux positron beamline.

Thanks are extended to Dr. D. R. Harshman from AT&T Bell Laboratories and Professor D. J. Keeble from Michigan Technological University for their long time collaboration, Dr. I. R. Rosenberg for his work on the high flux beamline, Mr. M. Taylor for his help in designing the high flux beamline, Dr. L. P. Chan for her help in the initial stage of the 2D-ACAR measurement, Dr. X. Y. Wu for his help in writing this thesis.

It is my pleasure to thank everybody working in the group of Particle-Solids Interactions. They created an environment of study and research and make my four

years research at Brookhaven National Laboratory a wonderful time.

I would like to thank the other members of my thesis committee: Prof. K. H. Becker, Prof. M. A. Kramer, and Prof. K. E. Miyano, for their spending time in reading my thesis.

Finally, I want to thank my wife Ms. Tao Wang for her support, patience, love, and help in organizing this thesis. This work was done at Brookhaven National Laboratory and was supported by the U.S. Department of Energy under contract No. DE-AC02-76CH00016.

To my dear wife Tao Wang

and my parents

Contents

Acknowledgements v

1 Introduction 1

1.1 Interactions of Positron with Solids 3

1.1.1 Thermalization 3

1.1.2 Implantation Profile 4

1.1.3 After Thermalization 5

1.2 Positron Annihilation with Electrons 5

1.3 Two-Photon Annihilation 6

1.4 The Principle of Positron 2D-ACAR 7

1.5 The Doppler Broadening Measurement 11

1.6 Positronium 12

1.7 Point Defects in Semiconductors 14

1.8 Positron Trapping in Defects 15

2 The Momentum Density of the $e^+ - e^-$ Pair 19

2.1 Momentum Density Function 20

2.2 Some Typical 2D-ACAR Spectra 24

2.3 Comparison With Other Techniques 28

2.3.1 Techniques for Band Structure and Fermi Surface Measurement 28
2.3.2 Techniques for Defects Studies 32

3 Experimental Setup **37**

3.1 Conventional 2D-ACAR Setup–Bulk Chamber 39
3.2 High-Intensity Monoenergetic Slow Positron Beamline 43
3.2.1 The Positron Source and Moderator 43
3.2.2 Beamline-Transportation of the Slow Positrons 48
3.2.3 Sample Chamber 52
3.3 Anger Camera 54
3.4 Angular Resolution of the system 56

4 Procedure of Data Analysis **59**

4.1 The Basic Procedure of the Data Analysis 60
4.1.1 The Camera Correction Function 60
4.1.2 Centering the Spectrum 63
4.1.3 Rotation of the Spectrum 64
4.1.4 Gaussian Smoothing 64
4.1.5 Symmetrization 65
4.2 Data Analysis for the Bulk Measurement 67
4.3 Data Analysis for the Interface Measurement 68
4.4 Error Analysis 72
4.4.1 Statistical Error 72
4.4.2 Other Sources of Error 73
4.4.3 Extra Error in the Interface Study 74

5 The SiO_2-Si System **75**

5.1 Si Single Crystal 76
5.1.1 The Energy Bands of Si Single Crystal 78
5.1.2 The Surface of Si Single Crystal 79
5.2 SiO_2 Layer on the Si Surface 80
5.2.1 Oxidation Technology 81
5.2.2 'Dry' and 'Wet' oxide 82
5.2.3 Planar Process 83
5.3 SiO_2-Si Interface 84
5.3.1 Interfacial Model 84
5.3.2 Interfacial Traps 86
5.3.3 Interfacial Defects 88
5.4 Positron 2D-ACAR Study of the SiO_2-Si System 90
5.4.1 The SiO_2-Si Sample 90
5.4.2 Overture–Doppler Broadening Measurement 92
5.4.3 Positron 2D-ACAR Spectrum at Positron Beam Energy of 2.0 keV 95
5.4.4 2D-ACAR Spectrum for Bulk Si 98
5.4.5 Spectrum at Beam Energy of 4 keV– Sampling the Interface Region 101
5.5 Quantative Discussion-The Size and Concentration of the Defects . . 108
5.5.1 The Width of the Ps Signal–Three-Gaussian Fit 108
5.5.2 The Estimation of the Concentration of the Defects 113
5.6 Result on a p-Type SiO_2-Si Sample 116
5.7 Investigation on an n-Type MOS Sample 116
5.7.1 2D-ACAR Spectrum at Beam Energy of 6 keV 119

5.7.2 2D-ACAR Spectrum at Even Higher Beam Energies 127
5.8 2D-ACAR Study of a SiO_2-Si Sample with Thinner Oxide 128

6 Study of Native Point Defects in Bulk Semi-Insulating GaAs 133
6.1 The Physical Properties of GaAs 134
6.1.1 The GaAs Single Crystal 134
6.1.2 Reciprocal Space: The Brillouin Zone 135
6.1.3 Energy Bands and Gaps 137
6.1.4 Vacancy Defects in GaAs 139
6.2 Positron 2D-ACAR Study of the As Vacancy in GaAs 142
6.2.1 Experimental Setup 142
6.2.2 The Sample–Semi-Insulating GaAs 144
6.2.3 2D-ACAR Spectrum in Darkness 144
6.2.4 2D-ACAR Spectrum of GaAs with Photo-illumination 146
6.2.5 Difference between the Spectra with LED 'on' and with LED 'off' 149
6.2.6 The Effect of Other Defects on the Spectrum with LED 'on' . 159
6.2.7 Comparing the Experimental Result with the Theoretical Calculations 160

7 Summary and Future Work 164

Bibliography 170

List of Tables

5.1 The relation between the depth and the diameter of the finite-spherical-well 113

5.2 The size and the concentration of the defects in the oxide and the interface region 115

List of Figures

1.1 $e^+ - e^-$ pair annihilation 8

1.2 The principle setup of the 2D-ACAR experiment 10

1.3 The principle setup of Doppler broadening measurement 12

1.4 The atomic configurations of simple point defects. 16

2.1 The HMC contribution to the momentum density function 23

2.2 The calculated positron density in tungsten 25

2.3 Positron 2D-ACAR spectrum in a α-quartz single crystal 26

2.4 2D-ACAR spectrum in a fused silica 27

2.5 The geometry of CP measurement and its principle setup 30

2.6 The typical setup for EPR measurement 33

3.1 The block scheme of the two sample chambers and the detectors . . . 38

3.2 The top view of the bulk chamber setup 40

3.3 The side-view of the bulk chamber setup 41

3.4 The decay scheme of ^{22}Na and the β^+ spectrum 42

3.5 The outline of the beamlines in the slow positron facility 44

3.6 Decay scheme of ^{64}Cu isotope and the β^+ spectrum 46

3.7 The part of beamline inside the blockhouse 49

3.8 The sample chamber for the beamline 53

3.9 2D-ACAR spectrum of α-quartz measured from the beamline chamber 58
4.1 Camera's correct function 62
4.2 Plot of χ^2 versus angle of rotation 65
4.3 The effect of gaussian smoothing 66
4.4 The definition of the S-parameter 70
5.1 The conventional cubic cell of Si lattice 77
5.2 Constant-energy surfaces near the conduction band minima in silicon 78
5.3 The energy bands in silicon 79
5.4 The crystalline model of the SiO_2-Si interface 85
5.5 Charges in the SiO_2-Si interface 87
5.6 The model of the broken bond defect 89
5.7 The sample configuration and positron annihilation fractions 91
5.8 S-parameter *vs* positron Energy curve 94
5.9 2D-ACAR spectrum at 2.0 keV. 96
5.10 The fine structure at 2.0 keV. 97
5.11 2D-ACAR spectrum at 14.5 keV. 99
5.12 Anisotropy of bulk silicon. 100
5.13 The comparison of anisotropy of Si with other work's result 102
5.14 2D-ACAR spectrum at 4.0 keV 103
5.15 The 'pure' interface spectrum 104
5.16 The fine structure of 'pure' interface spectrum. 105
5.17 The model of the spherical well potential. 111
5.18 2D-ACAR spectrum at 2.0 keV for p-type sample. 117
5.19 The interface spectrum for the p-type sample. 118
5.20 The configuration of the n-type MOS sample. 120

5.21 S-parameter result on the n-type MOS. 121
5.22 The Spectrum at 0 V bias. 122
5.23 The spectrum at -15 V bias. 123
5.24 The difference between -15 V bias and 0 V bias. 125
5.25 The spectrum at +15 V bias. 126
5.26 The spectrum at -30 V bias. 127
5.27 S-E curve for the thinner oxide sample. 129
5.28 2D-ACAR spectra for the thinner oxide. 130
5.29 The interface spectrum for the thinner oxide sample. 131
6.1 Conventional unit cube for GaAs 135
6.2 First Brillouin zone for the GaAs lattice 136
6.3 Hexagonal (011) cross section of the GaAs first Brillouin zone 137
6.4 The electron energy vs reduced wave vector 139
6.5 Variation of energy with wave vector 139
6.6 The calculated energy levels of point defects in band gap for GaAs . . 141
6.7 Side view of the experimental setup-inside vacuum chamber 143
6.8 2D-ACAR spectrum for GaAs in darkness 145
6.9 The anisotropy of bulk GaAs 147
6.10 The comparison of the anisotropy spectrum with the first BZ 148
6.11 2D-ACAR spectrum with LED illumination 149
6.12 The difference spectrum 150
6.13 The saturation curve of the 2D-ACAR spectrum 151
6.14 The temperature dependence of the difference spectrum 152
6.15 The defects spectrum 158

6.16 The comparison of experimental data to theoretical calculation-bulk GaAs 161
6.17 The comparison with theory–defects spectrum 162

Chapter 1

Introduction

Recently, Positron Annihilation (PA) as a microscopic probe, has attracted more and more attention in the field of solid state physics and materials sciences, especially after it was realized that PA is a promising tool to study defects in materials. As the antiparticle of the electron, postulated by Dirac[1] in 1930 to be the "negative" energy solution of his relativistic wave equation (the Dirac equation for free electron) and discovered experimentally by Anderson[2] in 1932, positrons entered the field of condensed matter in the 1950s, this period also was marked by the discovery that the two γ-rays arising from the annihilation of a thermalized positron with an electron in a solid were not exactly collinear, and this phenomenon was attributed correctly to the electron's momentum[3, 4]. In the last three decades, solid-state investigations with positron annihilations predominantly concentrated on resolving the Fermi Surface and band structures of metals and superconductors [5, 6, 7, 8], initiated by the invention of the set-up for angular correlation of annihilation radiation (ACAR)[9, 10, 11]. In the early 1970s, it was clearly realized that positron is very sensitive to the defects in solids, especially open volume related neutral and negatively charged defects[12].

Based on this fact, the technique of positron lifetime measurement was developed, which strengthened our knowledge of positron trapping in defects. At that time, radioactive sources with β^+ decay and with a reasonable long lifetime (e.g.^{22}Na with a lifetime of 2.7 years, ^{58}Co with a lifetime of 78 days) were used and the positrons emitted from the source were guided onto samples directly. Due to the large energy spread of β^+ spectrum, ranging from 0 to 1 MeV, the PA investigations were limited to the studies of the averaged bulk properties.

Almost from the onset, Madanski and Rasetti[13] realized that the continuous energy distribution of positrons emitted from standard sources was a limitation in the capabilities of the probe. Since then, a reasonable amount of effort has been devoted to moderating positrons from a radioactive source to lower energies to obtain a source of positrons that were more or less monoenergetic. After a few decades of work on this direction, the slow positron beams with a reasonably high intensity came into being in the period of mid 70s to early 80s[14, 15, 16, 17], and were used mainly to diffraction or scattering related surface state studies. While PA related measurements with positron beam were delayed for a few years due to the requirement of high statistics which would require higher intensity beam, especially for positron ACAR measurements. Positron ACAR experiments using slow positron beam was first performed on the surface of materials at Lawrence Livermore National Laboratory by Howell *et al*[18] employing a high intensity positron beam produced by an accelerator. Similar researches were started at Brookhaven National Laboratory (BNL) by Lynn *et al*[19] using a high intensity positron beam based on the High Flux Beam Reactor (HFBR) at BNL at about the same time and the positron beam ACAR experiments continued at BNL[20, 21].

Although a slow positron beam was developed at BNL with a beam intensity of

$\sim 5 \times 10^5 e^+/sec$, to do routine positron Doppler broadening measurements, the work in developing a high intensity slow positron beam continues. A new high flux positron beam facility was built a few years ago, based on different ideas and consisting of magnetic guided and electrostatic guided beamlines, adapted for multipurpose researches. Up to the present, the beam intensity has reached $\sim 10^8 e^+/sec$ on the magnetic beamline which was constructed three years ago for positron two-dimensional ACAR (2D-ACAR) measurement in the studies of buried interfaces and other layered systems. The subject of this thesis fall into two parts: one is the study of point defects in semi-insulating gallium arsenide (SI-GaAs, Here semi-insulating means that the conductivity of the materials is between that of semiconductors and insulators.) using conventional positron 2D-ACAR methods (e.g. using a ^{22}Na source) and the other is using the high intensity slow positron beam 2D-ACAR method to study the buried SiO_2-Si interface. The unique and exciting results from these experiments shows that positron 2D-ACAR is a powerful and promising probe and may open a new direction in applying positron 2D-ACAR technique in solid state physics and materials sciences. In this chapter, a brief introduction will be given to the interactions of positron with solids and the principle of their measurement, before detailed discussion of the experimental results in the following chapters.

1.1 Interactions of Positron with Solids

1.1.1 Thermalization

As an energetic positron emitted from a radioactive source impinges into a material, it loses its energy by various inelastic processes, e.g. by atomic ionization at high energy, electron-hole creation at medium energy and positron-phonon interactions at low

energy; finally, the positron reaches thermal equilibrium with the surrounding crystal. The whole process of thermalization takes place only in a few tens of picoseconds (ps), which is considerably shorter than positron lifetime in materials which is about a few hundred ps. Positron thermalization is the basis of the application of PA techniques. It was investigated by several workers with different materials and at different temperatures[22, 23, 24, 25, 26]. A brief review on this topic was given recently by Puska and Nieminen[27].

1.1.2 Implantation Profile

The implantation profile of positrons from a radioactive source (with an energy spectrum in the range of $0 \sim 1$ MeV) can be well described by an exponential law, which has been investigated by Brandt and Paulin[28, 29].

$$I(z) = I_0 \exp[-\alpha_+ z] \tag{1.1}$$

The linear-absorption coefficient, α_+, in a wide variety of materials is given by

$$\alpha_+ \simeq 16 \frac{d[g/cm^3]}{E_{max}^{1.4}[MeV]} [cm^{-1}] \tag{1.2}$$

where d is the density of the material, and E_{max} is the endpoint energy of the β^+ spectrum. Typical implantation ranges in solids are thus of the order of a millimeter: conventional positron implantation always produces a bulk probe.

For a beam of monoenergetic positrons, the implantation profile can be closely modeled by a Makhovian distribution[30, 31, 32]:

$$P(z) = P_0 \frac{m z^{m-1}}{z_0^m} exp[-(\frac{z}{z_0})^m] \tag{1.3}$$

where m is a shape parameter. z_0 is the stopping length of the absorbing material

and is related to the mean stopping depth $\bar{z}$ and the beam energy E (in keV) by:

$$z_0 = \frac{\bar{z}}{\Gamma(1+\frac{1}{m})} \tag{1.4}$$

and,

$$\bar{z} = AE^n \tag{1.5}$$

The constants m, A, and n have been determined experimentally [33, 34, 35] to be

$$m \approx 1.9 \tag{1.6}$$

$$A = 400\frac{g}{cm^3 keV^n}d^{-1}[\text{Å}] \tag{1.7}$$

where n=1.6 for most of the materials, and d is the density of the absorbing material.

1.1.3 After Thermalization

Owing to the low e^+ density in the sample (at any one time there is, on the average, only one positron in the sample), the thermalized positron is in its ground state and its motion obeys the Boltzmann distribution,

$$f_+(E_+,T) = (\pi m^* k_B T)^{-3/2} \exp\left[-\frac{E_+}{k_B T}\right] \tag{1.8}$$

where E_+ denotes the positron's kinetic energy, m^* its effective mass, and k_B is the Boltzmann constant. The behavior of the thermalized positron before annihilation with electrons–its diffusion will be discussed in section 4.3, together with a discussion of positron S-parameter measurements.

1.2 Positron Annihilation with Electrons

Once the thermalized positrons are in their low-energy states as delocalized Bloch waves (positron forms its own "positron energy band" since there is no Pauli exclusion

between the positron and electrons), they will stay at the bottom of the conduction band with a crystal momentum, $\vec{K} \approx \vec{0}$, and diffuse with a characteristic mean free path until an annihilation takes place or they are trapped in defects. In a perfect crystal, the thermalized positrons in their delocalized states will annihilate with the valence electrons or with core electrons. The $e^+ - e^-$ pair will annihilate within a few hundred ps characteristic of the environment surrounding the pair. The discussion of the selection rule and other consideration that determine the probability of the various modes of annihilation of slow $e^+ - e^-$ pairs can be found in fundamental texts in Quantum Electrodynamics[36, 37] and the review paper[38].

The annihilation process will supply an energy $\sim 2m_0c^2$, the total rest mass energy of the annihilating pair. For slowly moving pairs, conservation of momentum demands that at least two bodies (particles or quanta) are involved in the process. Single-photon annihilation is only possible in the presence of a third body, an electron or nucleus which can absorb the recoil momentum.

The probability of two-photon annihilation is considerably greater than that for one or three photons; the ratios of the cross sections for the respective processes is:

$$\frac{\sigma_{(3)}}{\sigma_{(2)}} \approx \alpha \frac{\sigma_{(1)}}{\sigma_{(2)}} \approx \alpha^4 \tag{1.9}$$

where $\alpha = \frac{1}{137}$ is the fine structure constant. Thus, our following discussion will concentrate on the two-photon process.

1.3 Two-Photon Annihilation

The cross section for the two-photon annihilation of a free positron and a stationary electron was given by Dirac[1]:

$$\sigma_{(2)} = \frac{\pi r_0^2}{\gamma + 1}\{\frac{\gamma^2 + 4\gamma + 1}{\gamma^2 - 1} \ln[\gamma + \sqrt{\gamma^2 - 1}] - \frac{\gamma + 3}{\sqrt{\gamma^2 - 1}}\} \tag{1.10}$$

where $\gamma = (1 - v^2/c^2)^{-1/2}$, and $r_0 = e^2/m_0c^2$ is the classical electron radius.

The mean lifetimes of positrons in matter normally lie within the range of 100 ps to 10 nanosecond (ns) and provide a guide to the electron density at the annihilation site. In addition to the lifetime, two other characteristics of the two-photon annihilation process, the relative emission directions and the energies of the annihilation photons, can provide useful information about the initial state of the $e^+ - e^-$ system. Thus, there are three techniques based on positron annihilation:

(1) Angular Correlation of Annihilation Radiation (ACAR) technique measures the angle between the two annihilation γ-rays.

(2) Doppler broadening experiment measures the energy shift of the γ-rays.

(3) Lifetime experiment measures the positron lifetime in materials.

In the next two sections the principles of the first two techniques will be introduced; positron lifetime measurement are discussed elsewhere[39, 40]. Emphasis will be placed on ACAR technique, especially its prototype–two dimensional angular correlation of annihilation radiation (2D-ACAR), the main subject of this thesis.

1.4 The Principle of Positron 2D-ACAR

In the center-of-mass frame of the annihilation pair, the two photons are emitted in opposite direction (with an angle $\Psi = 180^o$ between them), each with an energy equal to one-half of the total energy of the system, *i.e.* $2E_0 = E_T = 2m_0c^2$-binding energy $\approx 2m_0c^2$. In the laboratory frame, moving at velocity $v \ll c$, the energies and emission directions are changed. Fig. 1.1 shows the annihilation process. The angle between the two photons is

$$\Psi \approx \frac{\vec{p}_\perp}{mc} \tag{1.11}$$

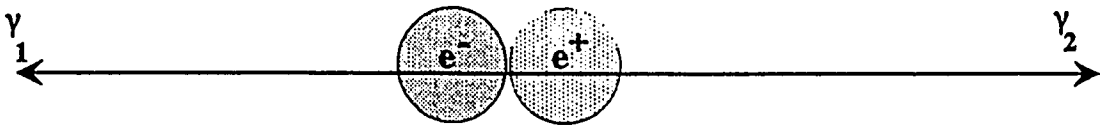

In the center-of-mass frame
The two γ–rays are collinear

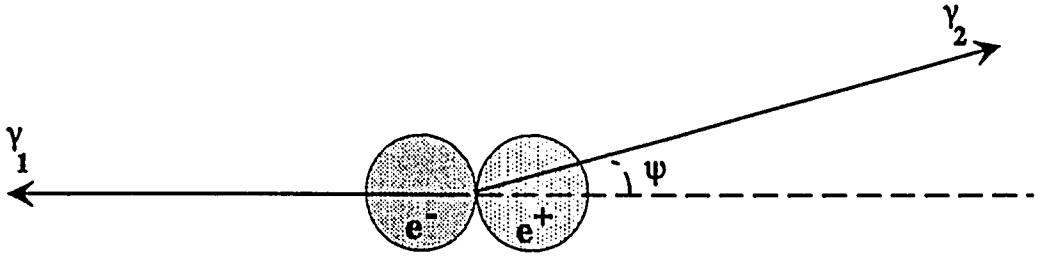

In the laboratory frame
The two γ-rays are non-collinear due to the motion of the pair

Figure 1.1: Schematic illustration of $e^+ - e^-$ pair annihilation into 2 γ-rays.

where mc is the momentum of the annihilation γ-rays with an energy of ~ 0.511 MeV and with $\vec{p}_\perp$ equal to the component of the $e^+ - e^-$ pair's momentum perpendicular to the direction of the annihilation photons. The ACAR technique measures the angle Ψ to reconstruct the motion (or momentum distribution) of the annihilating $e^+ - e^-$ pair. This is the principle of the so-called 1D-ACAR or ACAR because it measures only one of the two components of the transverse momentum. The invention of modern two dimensional position sensitive detectors by S. Berko[9] have made it possible to measure the two transverse components of the $e^+ - e^-$ momentum; this technique is called positron 2D-ACAR. Such measurements display the momentum distribution in two directions, *i.e.* the projection of the momentum distribution along a selected direction. Figure 1.2 shows the principle setup for 2D-ACAR experiment. The two components of the momentum in transverse plane are generally denoted as p_x, p_y, while the longitudinal component is denoted as p_z. The two angles, θ, ϕ, measured by 2D-ACAR are related to the transverse momentum, p_x, p_y, by:

$$\theta = \frac{p_x}{mc}, \qquad \phi = \frac{p_y}{mc} \tag{1.12}$$

The total 2D-ACAR spectrum, $N(\theta, \phi)$, is determined by the momentum density of the $e^+ - e^-$ pair, $\varrho^{2\gamma}(\vec{p})$:

$$N(\theta, \phi) = \int \varrho^{2\gamma}(\vec{p}) dp_z \tag{1.13}$$

Here we use $\varrho^{2\gamma}(\vec{p})$ to denote the pair momentum density to distinguish it from the "real" electron momentum density $\varrho(\vec{p})$. The calculation of the momentum density, $\varrho^{2\gamma}(\vec{p})$, and some example of 2D-ACAR spectra will be given in the next chapter.

By taking the projection along sufficient different directions, it is possible to reconstruct the three-dimensional momentum density from 2D-ACAR measurements, with an appropriate computer algorithm (mainly dealing with the Fourier transform

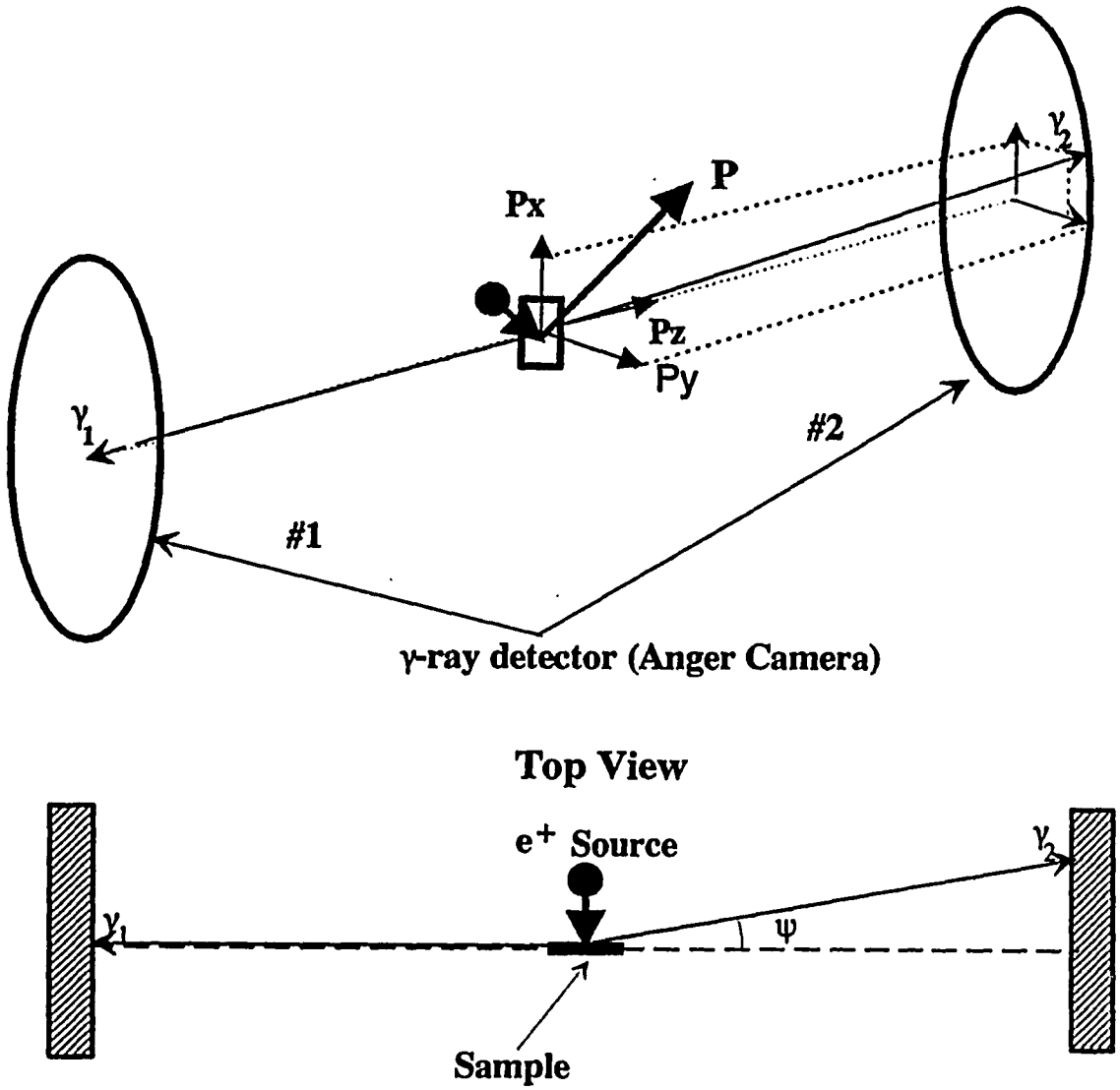

Figure 1.2: The principle setup of the 2D-ACAR experiment.

of each projection). One example is the three dimensional reconstruction of the momentum density of $e^+ - e^-$ pair in an La-214 high-T_c superconductor by Tanigawa *et al*[41].

The most of the application of this technique in solid state physics in the last two decades were to study the Fermi surface and band structure in metal, alloy[6], and the high-Tc superconductors[42, 8]. Recently, this technique proven to be a powerful tool to examine defects, their structure in the atomic scale, in solids[43, 44, 45]. Positron 2D-ACAR study of defects will be the main subject of this thesis.

1.5 The Doppler Broadening Measurement

Similar to eq. 1.11 and 1.12 the energies of the annihilation quanta in the laboratory frame can be expressed as

$$E_{1,2} = E_0 \pm \delta E \approx m_0 c^2 \pm \frac{c\vec{p}_{\|}}{2} \tag{1.14}$$

where $\vec{p}_{\|}$ or p_z is the component of the momentum 'along' the emission direction. Thus, by measuring the energy shift, δE, of the annihilation γ-rays, the longitudinal momentum p_z, can be reconstructed. This technique is called Doppler broadening measurement and is equivalent to the 1D-ACAR measurement. In principle, simultaneous measurements could be made of 2D-ACAR and Doppler broadening. In practice, such an ideal experiment is not feasible because of the restricted signal intensity which is limited by the detector's efficiency. Although a new technique employing Doppler broadening measurement was developed[46, 47] recently based on Lynn *et al*'s idea[48], from which the chemical composition at or near the annihilation site can be identified with fixed positron energy, the most successful application of Doppler broadening measurement in solid state physics or materials sciences was to observe

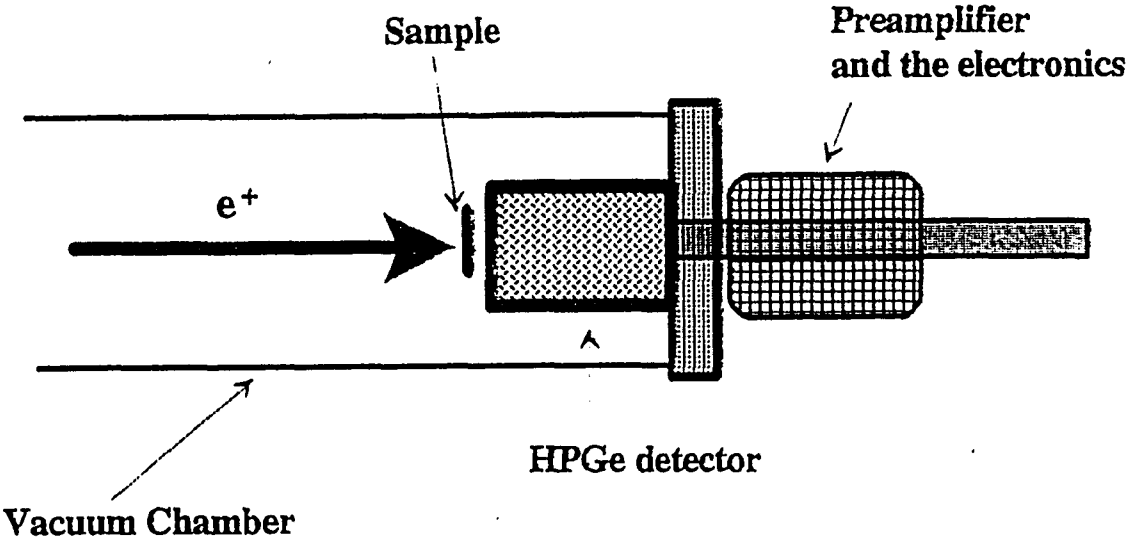

Figure 1.3: The principle setup of Doppler broadening measurement

the variations of the energy shift with positron energy (or implantation depth) for layered system, employing a variable energy positron beam[49, 50, 51]. In this case, the parameter measured is called S (line shape) parameter which will be discussed in detail in section 4.3. Thus, the Doppler broadening measurement is generally called S-parameter measurement.

1.6 Positronium

Positronium (Ps) is the bound state of the positron-electron pair. It is a hydrogen-like atom with the bounding energy of 6.8 eV at ground state in vacuum (instead, the energy is 13.6 eV for hydrogen and the difference reflects the fact that the reduced mass of the nucleus of the hydrogen atom is twice as large as the reduced mass for positronium.). Because the positron and the electron have spin $\frac{1}{2}$, then the ground state of Ps atom will have either spin 0 or 1. Historically, the spin singlet (S=0)

state of Ps atom was denoted as para-positronium (para-Ps) and spin triplet (S=1) state was denoted as ortho-positronium (ortho-Ps). In a free space, the probability of a ground state Ps in the singlet state is $\frac{1}{4}$, while in the triplet state, it is $\frac{3}{4}$. The lifetime of para-Ps in vacuum is 125 ps, while that of ortho-Ps is much longer, being 140 ns[12, 37].

According to Wallace[52], positronium can be formed in molecular materials where electron exchange occurs only within individual molecules and covalence forces between molecules, if they exist, are repulsive. The energetics of Ps formation in solids are most easily discussed in terms of the 'Ore Gap', a concept originating from the corresponding problem in gases[53]. If the ionization potential of a molecule of the medium is V_i, Ps can be formed as long as the initial energy of the positron E is greater than V_i-6.8 eV. If $E > V_i$, inelastic scattering with ionization will be more probable[52], and if $E > V_e$, the lowest excitation potential, this excitation will compete with Ps formation. Thus, Ps formation is most probable for the range of positron energies

$$V_e > E > V_i - 6.8eV \tag{1.15}$$

This is the 'Ore Gap' whose width plays a significant role in determining the yield of Ps atoms. Ps formation in some ionic crystals (for example, alkali halides) has been observed already[54], but generally it is difficult to form in perfect ionic crystals[55] due to large positron and electron affinities in the crystal. In the case of perfect ionic crystal, the 'Ore Gap' can be modified as:

$$Q_e + Q_p < Q_{pos} + B.E. \tag{1.16}$$

where Q_e, Q_p, Q_{pos} are the affinities of electron, positron, and positronium, respectively. B.E. is the binding energy of the positronium atom in matter (which may be smaller than 6.8 eV). A special and useful specimen is the crystalline quartz which is

an intermediate ionic-covalent compound in which Ps formation has been extensively studied[56, 57]. In contrast, Ps has never been observed in metals because of the continuous energy distribution of the conduction electrons., but it can be formed in the surface of metals[20, 21]. Theoretical analysis shows that it is extremely hard for the Ps to form in metals[55]. Positronium formation at the surface of metals and semiconductors has been extensively studied[58, 59, 20].

1.7 Point Defects in Semiconductors

There are very good descriptions of the physical properties of the point defects in semiconductors and of various experimental methods to detect them[60, 61], from both theoretical and experimental aspects.

The concept of a perfect crystalline solid with every atom in its proper place is introduced in introductory texts on solid-state physics. This is a convenient first step in developing the concept of electron band structure, and, from it, deducing the general electronic and optical properties of crystalline solids. However, such a concept is only an idealization of real solids. In fact, a perfect crystal does not exist. There are always defects.

It was recognized very early in the study of solids that these defects often have a profound effect on the real physical properties of solids. As a result, a major part of scientific research in solid state physics has been devoted to the study of defects, from the early studies of "color centers" in alkali halides to the present vigorous investigations of deep levels in semiconductors. In fact, most of the interesting and important properties of solids-electrical, optical and mechanical- are known to be determined not so much by the properties of the perfect crystal as by its imperfections. The very existence of the semiconductor industry is based upon the ability to control

electrical conductivity and its type by trace additions of shallow donor and acceptor chemical impurities. Research on defects in semiconductors has, therefore, been an active field since the beginning when semiconductors first emerged as technologically important materials.

It is necessary to distinguish between lattice defects and foreign atoms, or impurities. Lattice defects can be point defects, which correspond to misplaced atoms, line defects, which correspond to misplaced lines of atoms and are known as dislocations, and planar defects, which correspond to misplaced planes of atoms and are known as stacking faults.

In this thesis, only the point defects will be discussed because of the limited knowledge of positron trapping in other kind of defects. Figure 1.4 gives the atomic configurations of some simple point defects: vacancy, interstitial, and antisite (for compound materials only).

1.8 Positron Trapping in Defects

Owing to the Coulomb repulsion from the nuclei, positrons would remain in the interstitial region in a perfect single crystal; this is why positron ACAR can map out the electron momentum distribution (in fact, the electron momentum density seen by positrons). If there are defects, especially open volume related neutral or negatively charged defects, then there will be a good opportunity for the thermalized positrons to become trapped into the defects. At open-volume defects (such as monovacancies) in solids, the potential sensed by the positron is lowered due to the reduction in the repulsion by the positive ion core. As a result, a localized positron state at the defect can have a lower energy eigenvalue than a state delocalized over the lattice. The transition from the delocalized to the localized state is called positron trapping. The

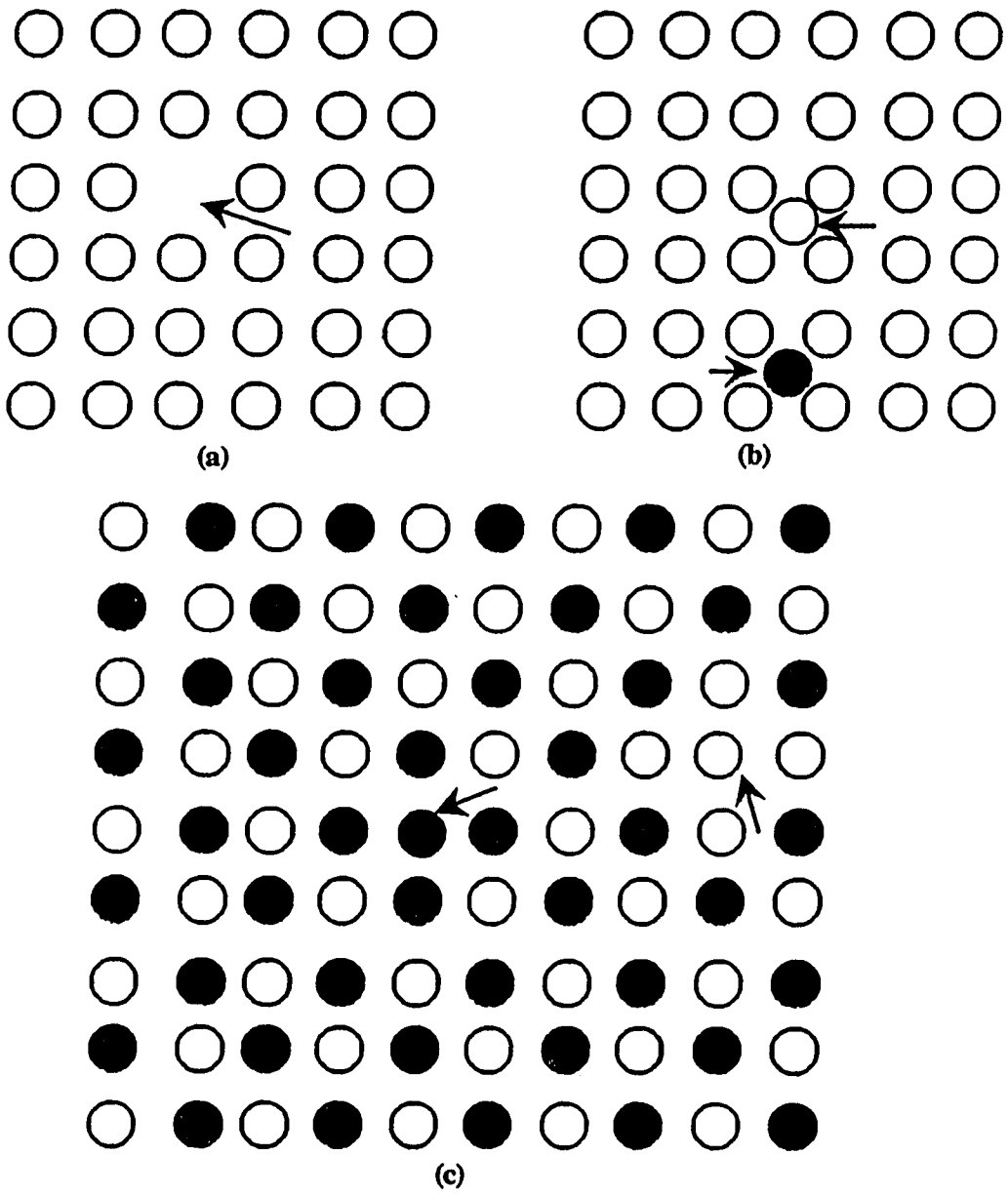

Figure 1.4: The atomic configurations of simple point defects. (a) Vacancy. (b) Interstitial. (c) Antisite.

energy difference between the initial and final positron states, the trapping energy, is transferred to the host solid. However, the trapped positrons may jump out of the defects due to some perturbation (thermal excitation, for instance) if the traps are not deep enough; this process, from the localized state to delocalized one, is called positron detrapping. A positron trapping model was developed on the basis of positron lifetime measurements, decomposing the positron lifetime spectrum. The kinetic equations which describe positron annihilation at delocalized states (free positrons) and localized states (trapped positrons) are written as

$$\frac{df_b}{dt} = -\lambda_b f_b - \kappa f_b + f_i \tag{1.17}$$

$$\frac{df_t}{dt} = -\lambda_t f_t + \kappa f_b \tag{1.18}$$

where $f_b(f_t)$ is the probability that the positron will be free (trapped) at time t. λ_b and λ_t are the annihilation rates (which are equal to the inverse of lifetime τ) for free and trapped positrons, respectively. f_i is the source term. i.e., the number of positrons implanted into the system per unit time. In the kinetic trapping model, the positron trapping rate κ is proportional to the concentration of defects, n_t, relative to the total density of the matter, n,

$$\kappa = \mu \frac{n_t}{n} \tag{1.19}$$

This equation defines the trapping coefficient μ (the trapping rate for a unit atomic concentration of defects, with $[\mu] = s^{-1}$). The total annihilation rate , λ, is

$$\lambda = \lambda_b + \kappa \tag{1.20}$$

The above formulae are valid if there is only one kind of defect. If there are more, then:

$$\lambda = \lambda_b + \kappa_1 + \kappa_2 + \ldots \tag{1.21}$$

and the relative probability for positron annihilating at free states or trapped to a specific kind of defect is

$$f_b = \frac{\lambda_b}{\lambda} \tag{1.22}$$

and

$$f_j = \frac{\kappa_j}{\lambda} \tag{1.23}$$

with $j = 1, 2, \ldots$. Generally, the positron trapping coefficient, μ, is a function of temperature. For negatively charged vacancies, $\mu \propto \frac{1}{\sqrt{T}}$, while for the neutral vacancies, μ is independent of temperature, and for positively charged vacancies, μ is at least an order of magnitude smaller than that for neutral vacancies and increases with rising temperature[62]. In semiconductors, investigations showed that the positron trapping coefficient , μ, is $10^{15} \sim 10^{16}/sec$ for negative vacancies, $\sim 10^{14}/sec$ for neutral vacancies, and $10^{11} \sim 10^{13}/sec$ for positive vacancies [27].

Chapter 2

The Momentum Density of the $e^+ - e^-$ Pair

As discussed in section 1.4, the positron 2D-ACAR technique measures the momentum distribution of the annihilating $e^+ - e^-$ pair in materials by measuring the angle between the two annihilation γ-rays. Thus, 2D-ACAR spectrum is determined by the momentum density function of the $e^+ - e^-$ pair. In this chapter, some formulae used in the calculation of the momentum density will be introduced, which will be helpful of understanding the background of the 2D-ACAR measurements, followed by some typical 2D-ACAR spectra to illustrate the principle and the powerfulness of the 2D-ACAR technique. And then a brief comparison of 2D-ACAR technique with other techniques used for studies of Fermi surface, defects, and interfaces will be given in the last section. The discussion on the density function will follow those given in ref.[6].

2.1 Momentum Density Function

The second-quantization formulation of the 2γ annihilation was given by Ferrell in 1956[55] as:

$$H'(\vec{p}) = \sum_{\vec{p}_1} \sum_{\vec{p}_2} a_{\vec{p}_1} b_{\vec{p}_2} \delta_{\vec{p}_1 + \vec{p}_2, \vec{p}} \tag{2.1}$$

where $a_{\vec{p}_1}$ and $b_{\vec{p}_2}$ are the electron and the positron annihilation operators, respectively. Using the point annihilation operators $\hat{\psi}_-(\vec{x}_1)$ and $\hat{\psi}_+(\vec{x}_2)$ given by

$$a_{\vec{p}_1} = \frac{1}{\sqrt{V}} \int d\vec{x}_1 \exp[-i\vec{p}_1 \cdot \vec{x}_1] \hat{\psi}_-(\vec{x}_1) \tag{2.2}$$

and

$$b_{\vec{p}_2} = \frac{1}{\sqrt{V}} \int d\vec{x}_2 \exp[-i\vec{p}_2 \cdot \vec{x}_2] \hat{\psi}_+(\vec{x}_2) \tag{2.3}$$

then one obtains the Hamiltonian operator

$$H'(\vec{p}) = \int d\vec{x} \exp[-i\vec{p} \cdot \vec{x}] \hat{\psi}_-(\vec{x}) \hat{\psi}_+(\vec{x}) \tag{2.4}$$

Thus, the probability for a two-photon annihilation event with a momentum $\vec{p}$, from an initial state $| i >$ to a specific final state $| f >$, is given by

$$\varrho_f^{2\gamma}(\vec{p}) = const. \cdot | < f | \int d\vec{x} \exp[-i\vec{p} \cdot \vec{x}] \hat{\psi}_-(\vec{x}) \hat{\psi}_+(\vec{x}) | i > |^2 \tag{2.5}$$

where $| i >$ stands for the initial state of the one-positron, n-electron system and $| f >$ stands for the final (n-1)-electron and two-annihilation-quanta state after annihilation.

In the standard angular-correlation experiments, the final states are not measured and thus can be summed over to obtain

$$\varrho^{2\gamma}(\vec{p}) = \sum_f \varrho_f^{2\gamma}(\vec{p}) \tag{2.6}$$

With the approximation of neglecting the constraints of the energy-conserving δ-function, the master equation can be obtained as

$$\varrho^{2\gamma}(\vec{p}) = const \cdot \int\int d\vec{x}d\vec{x'} \exp\left[i\vec{p}\cdot(\vec{x}-\vec{x'})\right] < i \mid \hat{\psi}_+^*(\vec{x})\hat{\psi}_+^*(\vec{x'})\hat{\psi}_-^*(\vec{x})\hat{\psi}_-^*(\vec{x'}) \mid i > \tag{2.7}$$

where the $const = \frac{\pi r_0^2 c}{(2\pi)^3}$ and r_0 is the electron classical radius.

In the configuration space with one positron, many electron initial wave function $\psi(\vec{r}_+, \vec{r}_1, \vec{r})$, properly antisymmetric in all electron co-ordinates, where $\vec{r}_+$ is the positron co-ordinate, $\vec{r}_1$ is an electron co-ordinate and $\vec{r}$ stands for the remaining electron co-ordinates $\{\vec{r}_2, \vec{r}_3, \ldots, \vec{r}_n\}$, the master equation becomes

$$\varrho^{2\gamma}(\vec{p}) \equiv \sum_j \varrho_j^{2\gamma}(\vec{p}) = const \cdot \int d\vec{r} \mid \int d\vec{x} \exp\left[-i\vec{p}\cdot\vec{x}\right]\psi(\vec{x},\vec{x},\vec{r}) \mid^2 \tag{2.8}$$

Finally, in the independent-particle-model (IPM), for a positron in state $\psi_+(\vec{r})$ annihilating in a system of electrons described by a Slater determinant of single-particle states $\psi_{-j}(\vec{r})$, the IPM master formula can be written as

$$\varrho_{IPM}^{2\gamma}(\vec{p}) = const \cdot \sum_j \mid \int d\vec{r} \exp\left[-i\vec{p}\cdot\vec{r}\right]\psi_+(\vec{r})\psi_{-j}(\vec{r}) \mid^2 \tag{2.9}$$

In periodic systems with a periodic potential $V(\vec{r}) = V(\vec{r}+\vec{R})$, where $\vec{R}$ is a lattice vector, e.g. perfect crystalline solid, the positron and the electron wavefunctions are Bloch waves:

$$\psi_{\vec{k}^+}(\vec{r}) = u_{\vec{k}^+}(\vec{r}) \exp\left[i\vec{k}^+\cdot\vec{r}\right] \tag{2.10}$$

and

$$\psi_{\vec{k}^-,j}(\vec{r}) = u_{\vec{k}^-,j}(\vec{r}) \exp\left[i\vec{k}^-\cdot\vec{r}\right] \tag{2.11}$$

where j now is a band index and $\vec{k}$ is a wave vector. For a single-electron Bloch wave, eq. 2.8 becomes:

$$\varrho_{\vec{k}^+,\vec{k}^-,j}^{2\gamma}(\vec{p}) = const \cdot \mid \int d\vec{r} \exp\left[-i\vec{p}\cdot\vec{r}\right]\psi_{\vec{k}^+}(\vec{r})\psi_{\vec{k}^-,j}(\vec{r}) \mid^2 \tag{2.12}$$

The Fourier transform appearing in eq. 2.12 is sometimes denoted by $A_j(\vec{p},\vec{k}^+,\vec{k}^-)$ (see ref.[55]). At zero temperature which is the simplest case, setting $\vec{k}^+ = 0$ and $\vec{k}^- = \vec{k}$, then eq. 2.12 can be written as

$$\varrho^{2\gamma}_{\vec{k},j}(\vec{p}) = const \cdot \sum_{\vec{G}} \mid A^{+,-}_j(\vec{k},\vec{G}) \mid^2 \delta(\vec{p}-\vec{k}-\vec{G}) \tag{2.13}$$

where the $A^{+,-}_j(\vec{k},\vec{G})$'s are the coefficients in the expansion of the periodic function

$$u^+(\vec{r})u_{\vec{k},j}(\vec{r}) = \sum_{\vec{G}} A^{+,-}_j(\vec{k},\vec{G}) \exp\left[i\vec{G}\cdot\vec{r}\right] \tag{2.14}$$

the $\vec{G}$'s are the reciprocal-lattice vectors of the crystal. Then

$$\varrho^{2\gamma}(\vec{p}) = \sum_{\vec{k},j} n_j(\vec{k})\varrho^{2\gamma}_{\vec{k},j}(\vec{p}) \tag{2.15}$$

where $n_j(\vec{k})$ is the step function equal to one for occupied states and zero for unoccupied states (i.e. with the step at the Fermi momentum $\vec{k}_f$ for metals).

The $A^{+,-}_j(\vec{k},\vec{G})$'s in master eq. 2.13 can be written as a convolution of the separate Fourier coefficients A^+ and A^- of the u^+ and u^- wave functions as

$$A^{+,-} = \sum_{\vec{G}'} A^+(\vec{G})A^-(\vec{k},\vec{G}-\vec{G}') \tag{2.16}$$

Eq. 2.13 shows the fundamental difference between real momentum $\vec{p}$ and crystal momentum $\vec{k}$: an electron with quantum number $\vec{k}$ will contribute not only at $\vec{p} = \vec{k}$ but at all $\vec{p} = \vec{k} + \vec{G}$, with amplitude $\mid A^{+,-}_j(\vec{k},\vec{G}) \mid^2$, as sketched in figure 2.1. The $\vec{G} \neq 0$ contributions are the "high momentum components" (HMC) of the momentum density.

For those positrons which are trapped into defects (in the localized states), their wavefunction will be the linear combination of the localized states and the delocalized states,

$$\psi^+(\vec{r}) = \psi^+_{local}(\vec{r}) + \psi^+_{delocal}(\vec{r}) \tag{2.17}$$

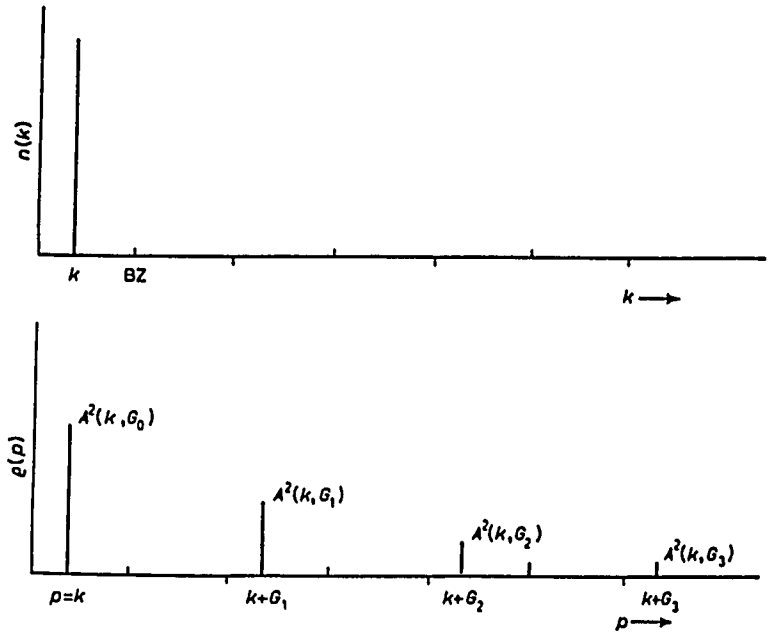

Figure 2.1: The HMC contribution to the momentum density function.

and the amplitudes of each part ($\mid \psi^{+}_{local}(\vec{r}) \mid^2$ and $\mid \psi^{+}_{delocal}(\vec{r}) \mid^2$) are determined by the depth of the traps. Thus, in 2D-ACAR spectrum, there will be two kind of signals overlapped together, one comes from positron annihilation at the localized states and the other from the delocalized states. In some cases, the positrons can be completely trapped into defects and there is no signal from the delocalized states (saturated trapping). For the positron trapped into defects, its annihilation status may be quite complicated: it may annihilate with the electrons trapped into the defects (if any), the valence and core electrons of the nearby atoms, depending on the overlap of the positron wavefunction with the wavefunctions of those electrons. Generally speaking, as a positron is trapped into vacancy-like defects, the overlap of its wavefunction with the wavefunction of core electrons of nearby atoms is very small because of the relative larger open volume available. The mechanism of using positron 2D-ACAR to study the defects structure is based on the fact that its wavefunction would be determined by the electronic structure (or even atomic configuration) around

the defects, not determined by the Bloch theorem. Figure 2.2 illustrates the positron density in Tungsten calculated by Gupta and Siegel[63] using a supercell approach and the electron density was obtained from an APW (augmented plane waves) calculation, the positron density at both the Bloch-state and the trapped state were considered.

2.2 Some Typical 2D-ACAR Spectra

From above discussion, it is clear that the positron 2D-ACAR spectrum is defined by eqs. 2.9 or 2.15. The following two examples show the result of 2D-ACAR measurements on a perfect single crystal and an amorphous solid.

Figure 2.3 is the 2D-ACAR spectrum of an α-Quartz single crystal. Silicon dioxide (SiO_2) is one of the kind of materials in which $e^+ - e^-$ pairs form their bound states–Positronium (Ps) atoms. While, as a crystalline SiO_2, the α-quartz lattice has a trigonal symmetry (or structure). The Ps atoms is delocalized in the single crystal, moving at the bottom of its conduction band(s). The small peak around the central sharp peak are due to the high momentum component of the Ps atoms governed by formula 2.13 with the integration (or projection) direction, p_z, along the z crystallographic direction.

Figure 2.4 gives a 2D-ACAR spectrum on a fused silica–amorphous SiO_2. In fused silica, the Ps atoms are localized due to the existence of large amount of voids and vacancies. Therefore, there is only one central peak, which is broader than that in the quartz single crystal, indicative of Ps trapping in open-volume related defects.

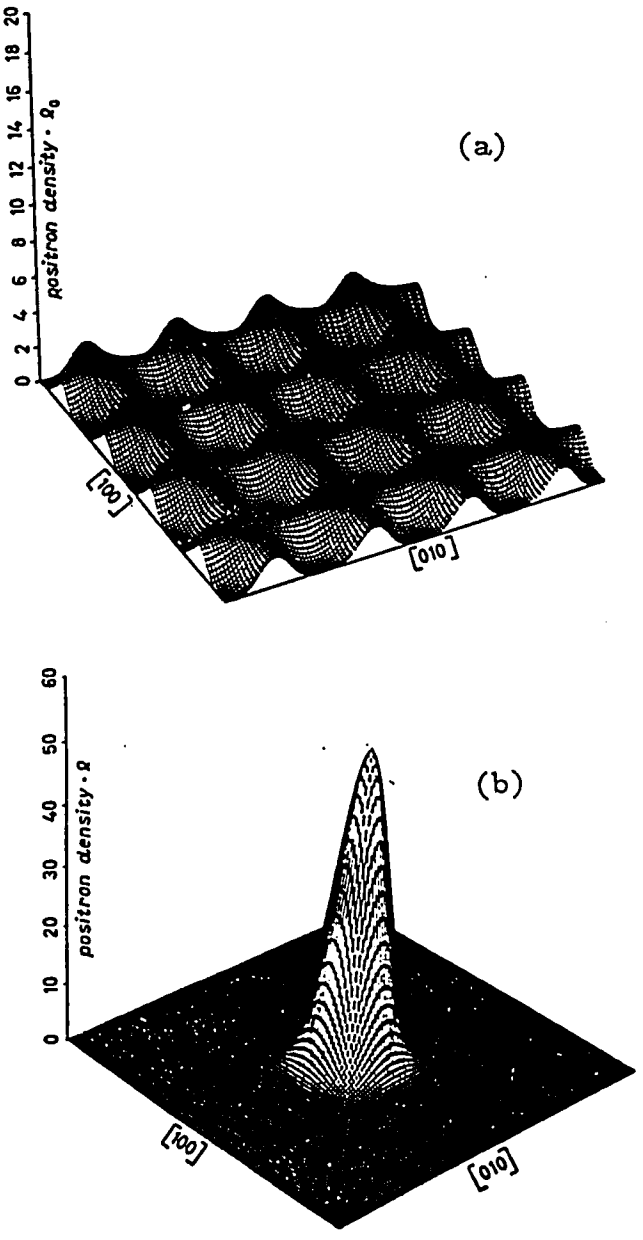

Figure 2.2: The Calculated positron density in Tungsten, shown on a network of 25 atom sites in the b.c.c. (001) plane. (a) Containing no vacancies–Bloch-state. (b) Containing a vacancy at the center–trapped positron. From ref [63].

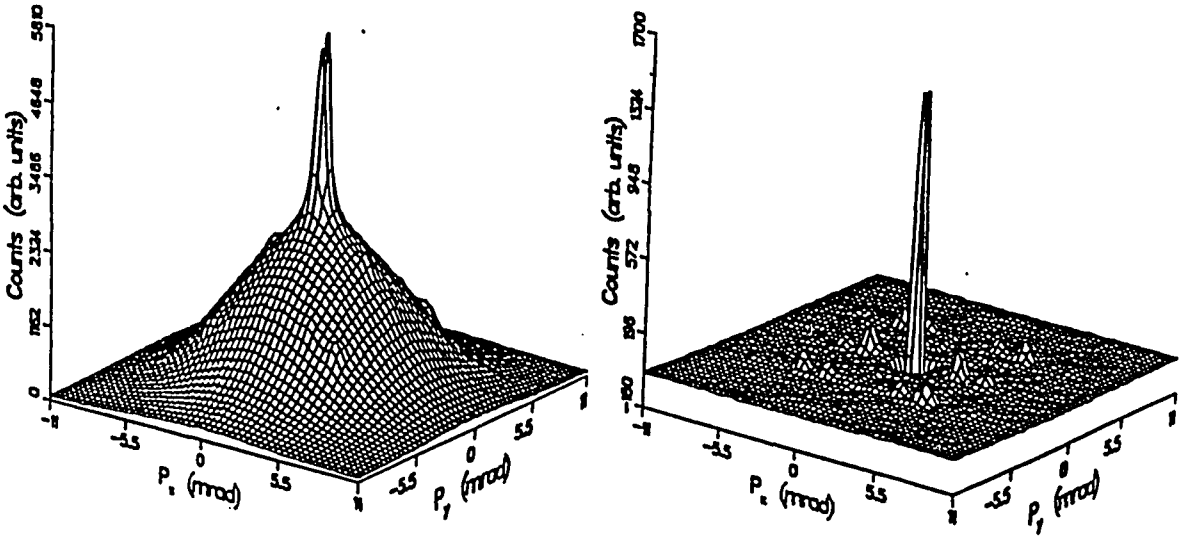

(a) (b)

Figure 2.3: Positron 2D-ACAR spectrum in a α-quartz single crystal.(a) The original spectrum. (b) The spectrum after the subtraction of a broad component (see the discussion given in sect. 4.2).

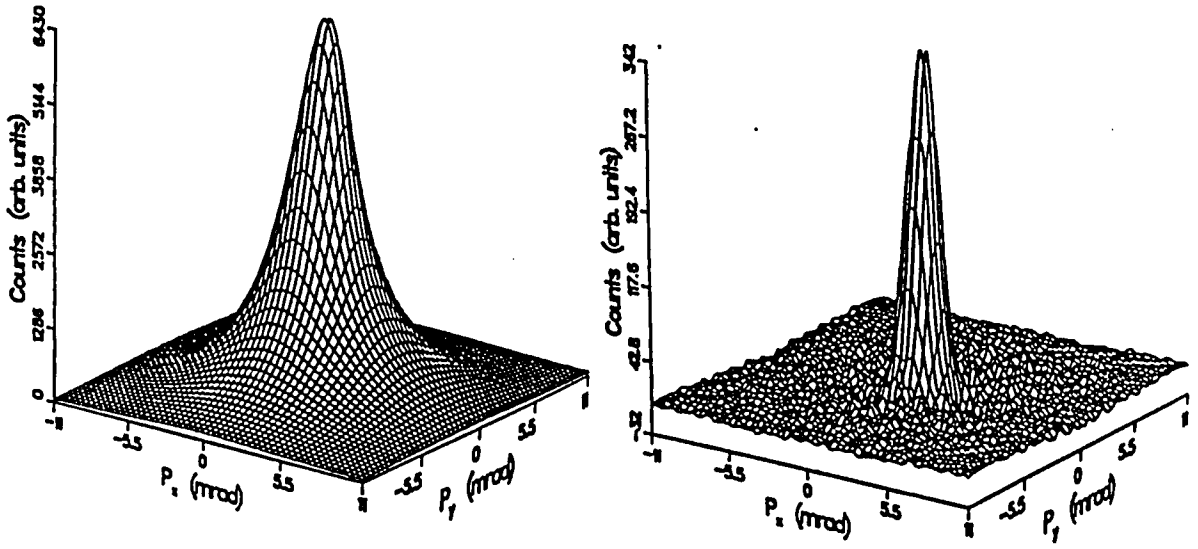

Figure 2.4: 2D-ACAR spectrum in a fused silica. (a) The original spectrum. (b) The spectrum after the subtraction of a broad component (see the discussion given in sect.4.2).

2.3 Comparison With Other Techniques

As a new promising technique, positron 2D-ACAR measurement supplies information about the band structure of crystalline solids when positrons annihilate in the delocalized states and electronic structure of defects when positrons annihilate in the localized states. Certainly, there are other techniques which can supply the same kind of information as positron 2D-ACAR does. In this section, a brief comparison of positron 2D-ACAR with other techniques will be presented. The comparison with band structure or Fermi surface techniques and with the defects detection techniques will be given separately.

2.3.1 Techniques for Band Structure and Fermi Surface Measurement

The traditional techniques for the band structure and Fermi surface measurement are de Haas-van Alphen (dHvA) technique and angle-resolved photoemission spectroscopy (ARPES). The dHvA technique based on the phenomenon that the inverse of the period of oscillations in the magnetic susceptibility as a function of the applied field is proportional to the extrema cross-sectional area of the Fermi surface in a plane normal to the applied field. The principle of this technique can be found in any standard solid state physics textbook[64]. The ARPES technique employs a beam of photons with an energy $h\nu$, greater than the work function of the measured material which is usually a few eV, to illuminate a sample. This results in the emission of photoelectrons, whose energy distributions reflect the occupied density of states below the Fermi energy, E_F. By measuring the photoelectron energy distributions as a function of position, the electronic band structure of the material can be reconstructed. This

technique is quite suit to measure the band structure for high-T_c superconductors due to the unconservation of the momentum of emitted electrons normal to the sample surface. A detailed comparison of 2D-ACAR with theses two techniques was given by Chan[42].

A relatively new technique for the Fermi surface measurement is the Compton Profile (CP) technique[65, 66], which measures the compton scattered photons to get information about the momentum density of electrons in materials. Since CP technique is very much similar to ACAR technique, it is necessary to give a more detailed comparison between the two techniques.

The compton profile is the energy distribution of inelastically scattered x-rays or γ-rays at a fixed scattering angle; the Compton-scattered photons are Doppler broadened about the Compton wavelength due to the initial momentum distribution of the electrons producing the scattering. Figure 2.5 show the geometry of the CP measurement and the principle setup, where $\mathbf{k}_i$ and $\mathbf{k}_f$ are the incident and scattered photon momenta, $\mathbf{p}_i$ and $\mathbf{p}_f$ the corresponding electron momenta, θ is the scattering angle, and $\mathbf{k} = \mathbf{k}_i - \mathbf{k}_f$ is the scattering vector defining the z-axis of the coordinate system. In the simple case of a nonrelativistic free electron system, the well-known Compton wavelength shift is

$$\lambda' - \lambda = \frac{2h}{mc} sin^2(\frac{\theta}{2}) - \frac{2\lambda}{mc} sin(\frac{\theta}{2}) p_z \tag{2.18}$$

where p_z is the component of $\mathbf{p}_i$ along the $\mathbf{k}$ direction.

In a typical experiment, one does not detect recoiling electron, all the momenta with component p_z will contribute for a given $\mathbf{k}$. Classical mechanically, for high-energy scattering with $\mid \mathbf{k}_f \mid$ much larger than the typical atomic momenta, the probability of measuring $\mathbf{k}_f$ should depend on the probability $J(p_z)dp_z$ (approximately) of having a momentum component between p_z and $p_z + dp_z$, given a momentum space

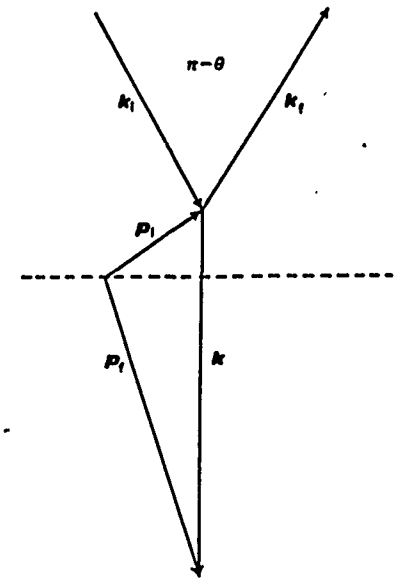

(a)

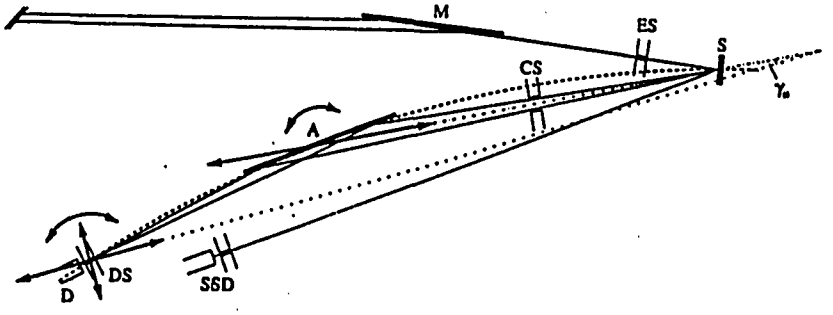

(b)

Figure 2.5: The geometry of CP measurement and its principle setup. In the setup, M–monochromator, S–sample, A–analyzer crystal, CS–aperture slit, DS-detector slit, D-detector (NaI scintillation counter and Ge-solid-state-detector (SSD)). This setup is used in the European Synchrotron Radiation Facilities (ESRF).

density of $\varrho(\mathbf{p})$:

$$J(p_z) = const \cdot \int\int \varrho(\mathbf{p}) dp_x dp_y \tag{2.19}$$

The integration is over a plane perpendicular to $\mathbf{k}$, as indicated by the dashed line in fig. 2.5.

Quantum mechanically, for the case in which the final electron energy is large compared to its binding energy prior to the scattering, the cross-section for Compton scattering from a single electron (under the impulse approximation and nonrelativistitic limit) is given by

$$\frac{d^2\sigma}{d\Omega d\omega} = f(\omega_i, \omega_f, \mathbf{k}) \int d\mathbf{p} \delta(\omega - \frac{k^2}{2m} - \frac{\mathbf{p}\cdot\mathbf{k}}{m}) \varrho(\mathbf{p}) \tag{2.20}$$

where, ω_i, ω_f are the initial and final photon energies, $\omega = \omega_i - \omega_f$, and $f(\omega_i, \omega_f, \mathbf{k})$ is a factor..

Thus, the Compton profile (CP) technique measures the 1D projection of the true momentum density $\varrho(\mathbf{p})$ onto a direction p_z parallel to the scattering vector $\mathbf{k}$. While ACAR technique measures the projections of the 'positron sampled momentum density', $\varrho^{2\gamma}(\mathbf{p})$. This is the major advantage of CP against ACAR. Two of the limiting factors that affect the application of CP technique are the poor resolution and the strong absorption of X-rays which would limit the CP measurement to low Z materials. Now the modern crystal spectrometers at the third generation synchrotron sources has overcome the resolution problem (a resolution as high as 0.01 a.u. can be reached by the setup shown in fig. 2.5. Note that 1 a.u. equals to 7.29 milliradian). Another advantage of CP study of Fermi surface is that it does not require low temperature which in the case of ACAR measurement the thermal motion of the positrons may smear out the Fermi break at room temperature. The big advantage of the ACAR technique against CP is that ACAR can have two-dimensional measurement (2D-ACAR) while it is difficult for the CP technique due to the difficulty of

coincident measurement of the recoiling electrons (although the two-dimensional CP setup is under construction to measure the Fermi surface for thin films, there is no successful report yet). As two relatively new technique, ACAR and CP measurement are attracting more and more attention.

2.3.2 Techniques for Defects Studies

There are quite a few techniques in the identification and characterization of defects in materials. Basically, the techniques can be divided into three categories by the physical quantities from which the information on the atomic structure or the electronic characteristics of the defects can be extracted: namely, electrical and optical techniques and electron paramagnetic resonance (EPR). It is not the intent of this thesis to make a thorough comparison of positron 2D-ACAR to all of these techniques.

Among these techniques, EPR is in general the most powerful one and the one most suited for providing a direct identification of a defect[67, 68, 69]. It measures the resonant absorption of electromagnetic radiation by systems composed of unpaired electrons placed in a magnetic field by lifting the degeneracy of the ground states of partially filled electron orbitals (the spin degeneracy). The absorption occurs when transitions are induced between the energy levels. The most successful application of EPR technique was in the identification of radiation related defects in Si. Figure 2.6 shows the basic setup for the EPR measurement. EPR measures the g-factor change via the orientation of the applied magnetic field, where the g is a factor appearing in the electron Zeeman Hamiltonian:

$$H_{Ze} = g\frac{e\hbar}{2mc}\vec{B}\cdot\vec{J} \tag{2.21}$$

where $\vec{B}$ is the applied field, $\vec{J}$ is the total angular momentum of the atom, and g is

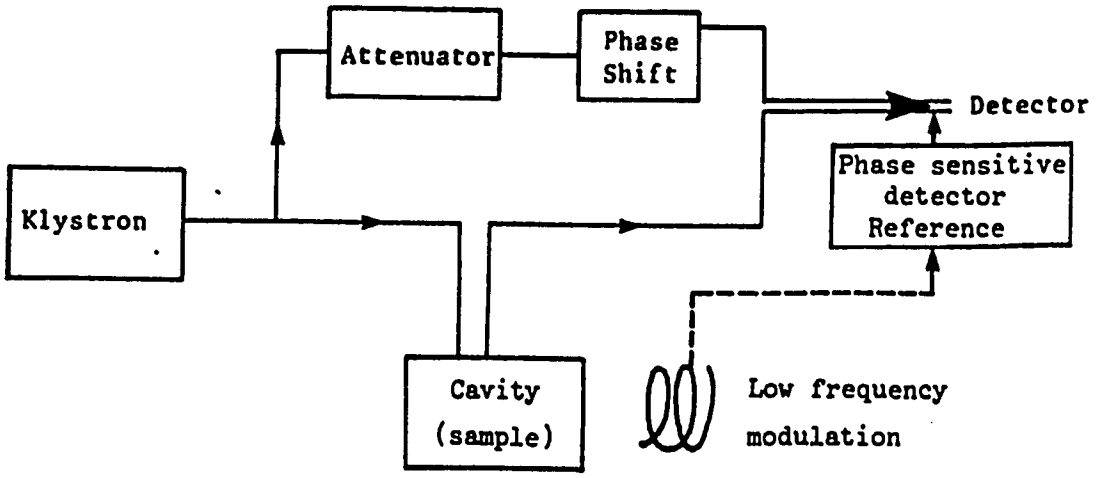

Figure 2.6: The typical setup for EPR experiment.

defined as

$$g = 1 + \frac{1}{2}\frac{J(J+1) + S(S+1) - L(L+1)}{J(J+1)} \tag{2.22}$$

where S is the total spin and L is the total orbital momentum (quantum numbers). The EPR spectrum contains detailed microscopic information on the electronic structure of the defects. Unfortunately, EPR technique only works for the paramagnetic system (odd number of unpaired electrons). For the materials in which the spin-lattice relaxation time is too short, the EPR lines are broad and difficult to detect(for the case of germanium). In other materials (like gallium arsenide-GaAs) all atoms have nuclear spins which give rise to hyperfine interactions, the EPR signal is broad and these interactions cannot be resolved[70]. All of this would limit the application of EPR. While this kind of limit does not exist for positron ACAR measurement (instead, the charge status of defects is a limiting factor to positron ACAR measurement).

Among the techniques for the interface structure measurement, transmission electron microscopy (TEM) and various forms of electron spectroscopy are the one most frequently used. TEM is the most elegant technique yet applied to the study of atomic configuration of surface and interface. In the TEM experiment, a very thin ($100\mathring{A}$) sample to be imaged is illuminated by an electron beam with energy greater that 100 eV. This beam must be as coherent as possible to obtain a good image. Upon passing through the sample, the beam is scattered by the electrostatic potential variations present, due primarily to the ion cores of the atoms. These scattered beams are then refocused by the objective lens of the microscope back into coincidence. For a perfect imaging system, there would be a one to one correspondence between the object and the image. This, however, is not possible in practice due to the defocusing type of phase contrast image obtained. In general, any real space model of the sample obtained from a TEM should be tested by a dynamical diffraction calculation to verify that artifacts in the imaging process are not misinterpreted. This is particularly important since, generally, only a few beams are allowed through the objective aperture to create the image. The resolution of the technique is determined by the properties of the electron beam itself (coherence and stability, the spherical aberration, and the wavelength or beam energy) with the currently optimized resolution in the range of $3 \sim 4\mathring{A}$ (at $\sim$ 100 keV). The big disadvantage of this technique is that a small amount of disorder render the high-resolution TEM images uninterpretable. Hence, while TEM results indicate the presence of an ordered, epitaxial SiO_2 film on Si(001) surface[71] , they have been unable to analyze the decay of order but instead see an abrupt transition from order to disorder, in other words, TEM can not observe point defects.

While the techniques of electron spectroscopy, including photoelectron spectroscopy

and Auger electron spectroscopy, have frequently been used to study the chemical nature of surface and interface. In particular, in the study of SiO_2-Si interface, the one capability of theses techniques which makes these studies critical is their ability to distinguish between different chemical states of silicon atoms. By their nature, they are sensitive only to the surface region of solids. This sensitivity is determined by the mean-free path of the emitted electrons, which can range from 5 to 50 $\AA$ depending on the spectroscopy employed. This surface sensitivity implies that interfaces can only be investigated for very thin films or for layers that have been thinned down by some other means (such as sputtering or chemical etching).

In last few years, x-ray scattering (or diffraction) start to be used in the study of the orderness of surfaces and interfaces, revealing the information about the change of crystallization near the surface or interface by grazing incident angle scattering. From the scattered spectrum, the surface roughness and the crystallization can be obtained[72], although the answer was not unique. The result on the microcrystalline near the SiO_2 -Si interface had been reported by Fuoss *et al*[73]. The advantage of x-ray scattering is that the interpretation of the experimental data is straightforward and by the development of modern synchrotron light source, the energy and spatial resolution can be improved dramatically[74]. X-ray scattering seem to be another promising tool in studying the interface, in term of the atomic configuration.

EPR is still the major technique in studying the defects structure in atomic scale in interface. As a probe for electronic (seen by positron) structure study of defects, the most important contribution from EPR was the identification of the P_b centers in SiO_2-Si interface (which will be discussed in Chapter 6). Certainly, it can not overcome the difficulties mentioned before for the bulk study. SiO_2-Si system is a special example which is appropriate for EPR applications.

Positron 2D-ACAR can accomplish both of the studies: periodicity in the atomic configuration and the electronic structure of defects. In particular, benefited from the development of slow positron beam, positron 2D-ACAR can perform the depth-resolved study and to access buried interfaces while the other techniques can only perform the study at the region near surface ($\leq 100\mathring{A}$ away from surface). This is the major advantage of positron 2D-ACAR. The disadvantage of positron 2D-ACAR technique is that the interpretation of its data is not as straightforward as for the other techniques.

Chapter 3

Experimental Setup

There are two sets of experimental systems employed for the 2D-ACAR experiment due to different purpose of the measurements. One is for the bulk property measurements called bulk chamber, a conventional 2D-ACAR setup. Another is for the measurements of layered system on the high intensity slow positron beamline called interface (beamline) chamber. The detectors used to detect the annihilation photons (γ-ray, $\sim$ 511 keV) are two two-dimensional position sensitive γ-ray detectors, called Anger cameras. Figure 3.1 shows the relative position between the two setups and the two detectors (top view). The detector frames can move freely on the rail to change the distance from the sample, which means changing the angular resolution of the measurements. The detectors which sit on the frames can be slided to align with one of the chamber depending on which one is used currently. In this chapter, the two setups and the detectors will be described but the emphasis will be on the high-intensity positron beamline.

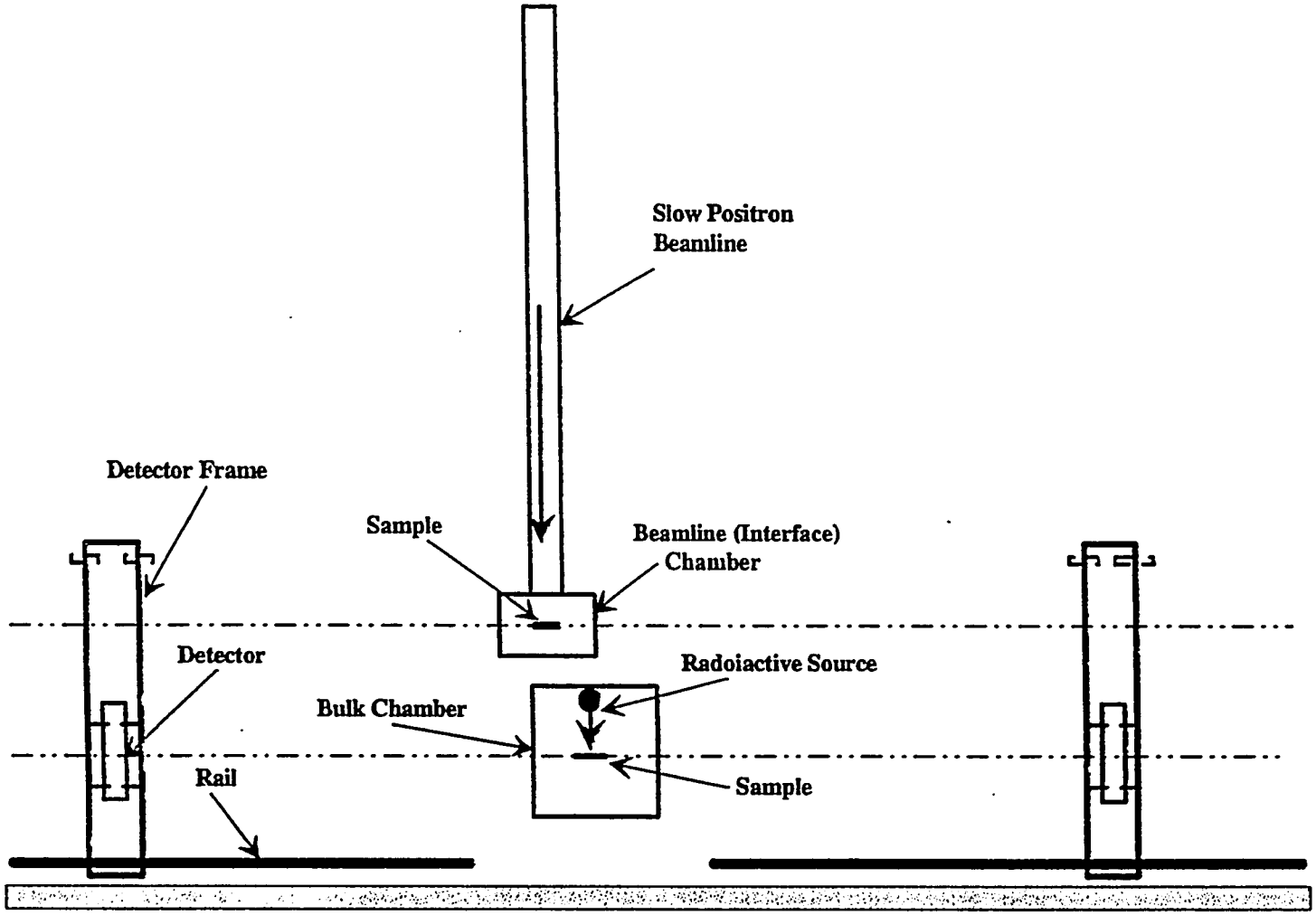

Figure 3.1: The block scheme of the two sample chambers and the detectors

3.1 Conventional 2D-ACAR Setup–Bulk Chamber

Figures 3.2 and 3.3 are the top and side views of the bulk chamber, showing the main components of the setup. The radioactive source which is used to produce positrons is put inside the vacuum chamber and is positioned in the front of the sample which is about 1 cm away from the source. The positrons are produced from an encapsulated ^{22}Na source with an activity of $\sim$ 30 mCi. The source was made at Brookhaven National Lab. by evaporating the NaCl solution into a stainless steel capsule. Then the dry NaCl coated on the inner wall of the capsule was sealed by a titanium foil of $\sim$ 4 microns with a surface area of $\sim$ 1 cm^2 and with a β^+ yield of $\sim$ 20% (20% of the total positrons can come out of the window). The decay scheme of ^{22}Na and the energy spectrum of the emitted β^+ particles are shown in figure 2.4. The positrons emitted from the radioactive source (and passing through the titanium window) are guided to the sample by a strong magnetic field produced by the two magnetic coils between which the sample chamber is sandwiched. With a 1.8 Tesla field, there are about 200 millions positron are guided to the sample surface and the spot size of the positrons at sample surface is 4$\pm$1 mm in diameter determined experimentally and the maximum diameter of the synchrotron motion of individual positron under this field is 2.25 mm. The heavy-metal (inside the vacuum chamber) and the lead-bricks (outside the chamber) are used to shield the 1.28 MeV γ-ray which follows each β^+ emission and the 0.511 MeV γ-ray from positron annihilation with the materials other than the sample to reduce the background in the detectors. The chamber was equipped with cooling stage (cold finger) so that the sample can be cooled down to $\sim 20^oK$. The vacuum level was kept at $10^{-7} \sim 10^{-8}$ Torr during the measurements.

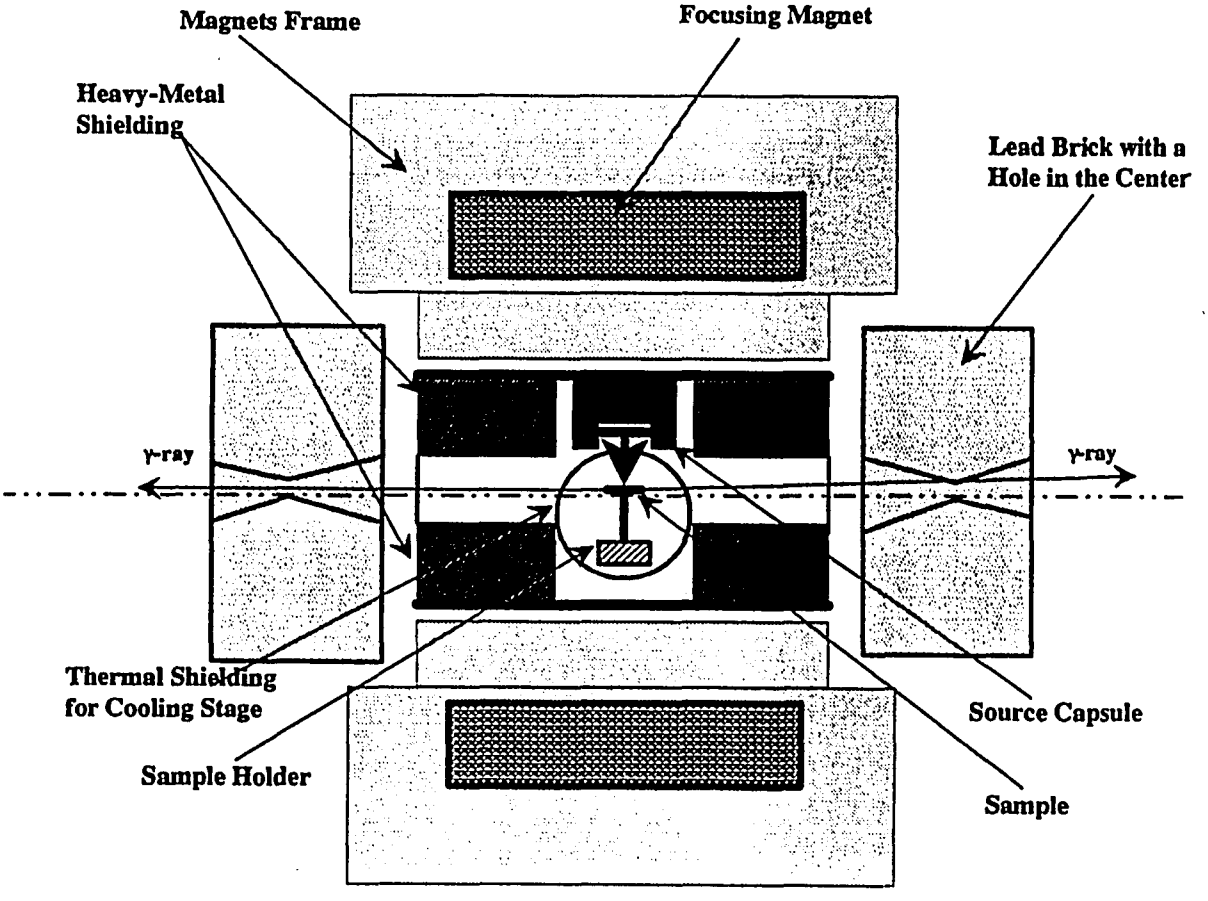

Figure 3.2: The top view of the bulk chamber setup.

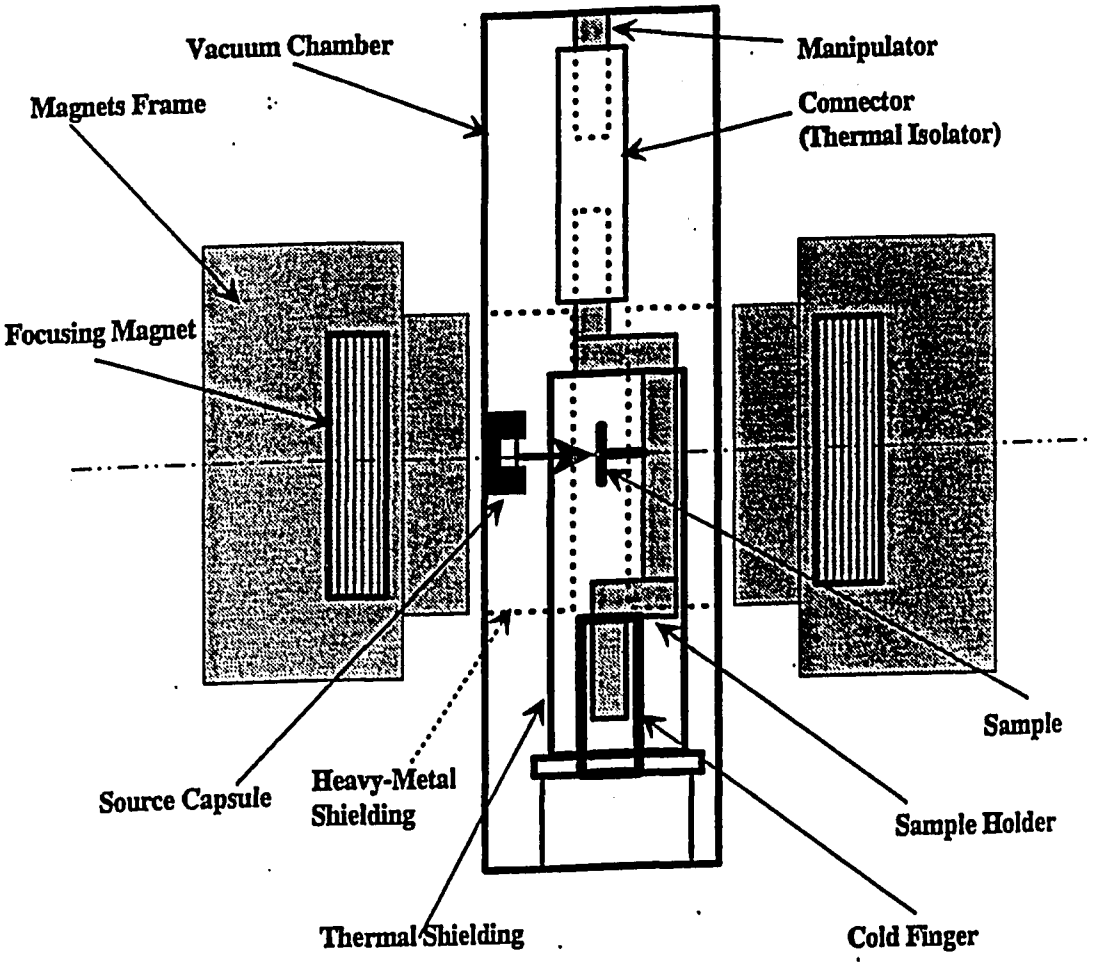

Figure 3.3: The side-view of the bulk chamber setup.

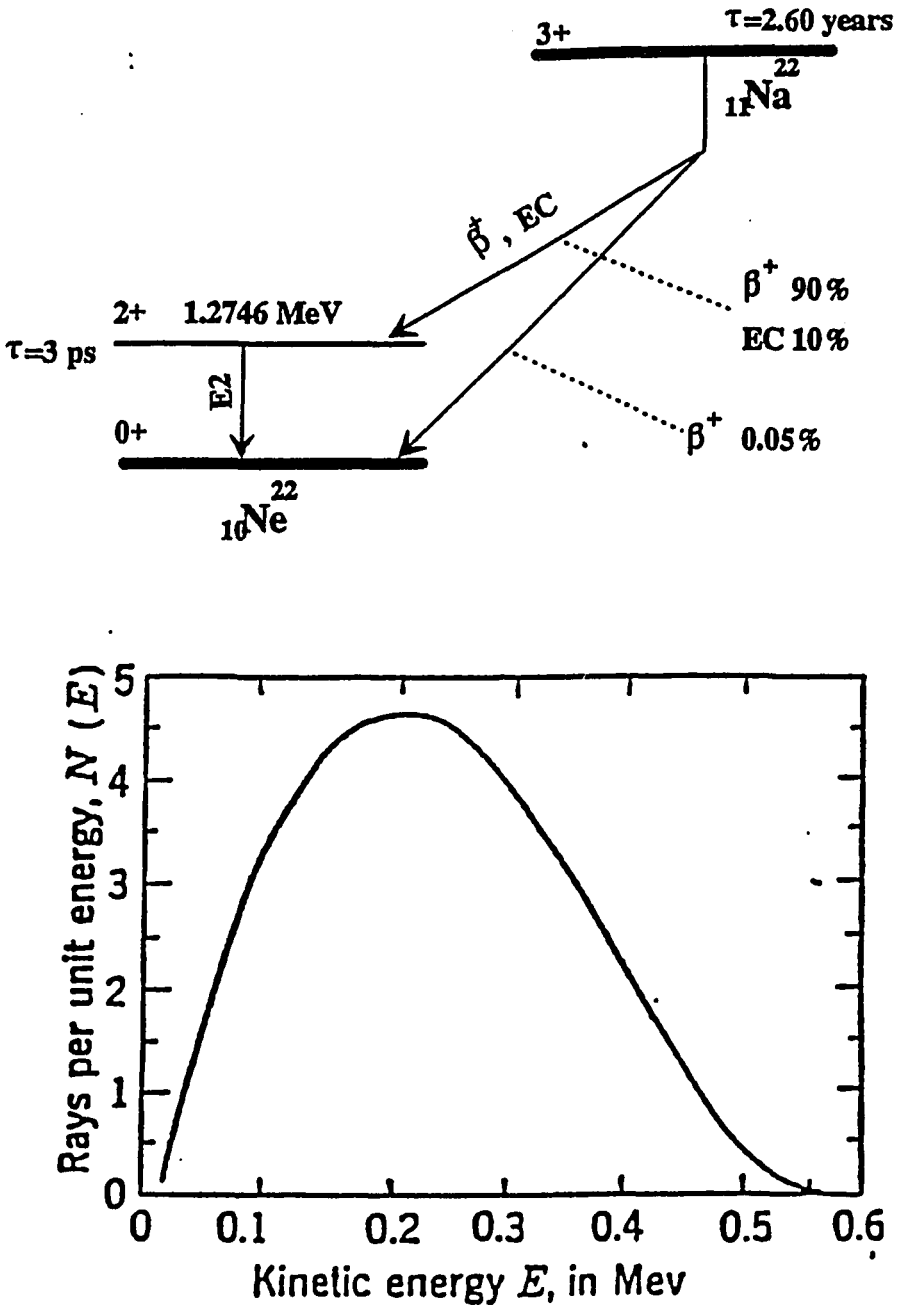

Figure 3.4: The decay scheme of ^{22}Na and the β^+ spectrum.

Because the energy of the positrons emitted from the ^{22}Na source ranges from 0 eV up to 0.58 MeV, the positrons will be implanted into the sample from surface down to deep inside the bulk (a few hundred microns), with the implantation profile given in eqs. 1.1 and 1.2. Thus, the conventional 2D-ACAR spectrum is an average of the bulk properties at different depth of the sample and the setup can only be used to study the bulk properties of materials, with the sample thickness of 0.5~1 mm.

3.2 High-Intensity Monoenergetic Slow Positron Beamline

As a major part of the high flux slow positron facility, the purpose of the High-Intensity Slow Positron Beamline (HISPB) was to guide the slow positrons to the sample chamber located in the 2D-ACAR experiment site. Figure 3.5 shows the outline of the few beamlines related to the whole slow positron facility. The HISPB is a magnetic-field-based beamline, transporting the monoenergetic slow positrons produced in the source region (source chamber) downstream to the 2D-ACAR sample chamber. Before the detailed description of the beamline, it is necessary to describe briefly the mechanism and the procedure of producing the slow positrons.

3.2.1 The Positron Source and Moderator

The radioactive source used to produce positrons is the ^{64}Cu isotope which was made at Brookhaven National Laboratory. First, the small sphere of natural ^{63}Cu (called copper Bee-Bee) with a mass of 150 $\sim$ 300 milligrams was irradiated by the thermal neutron in the HFBR at Brookhaven Lab. and the stable ^{63}Cu atom become a radioactive ^{64}Cu atom (with a lifetime of 12.7 hours) after the absorption of a

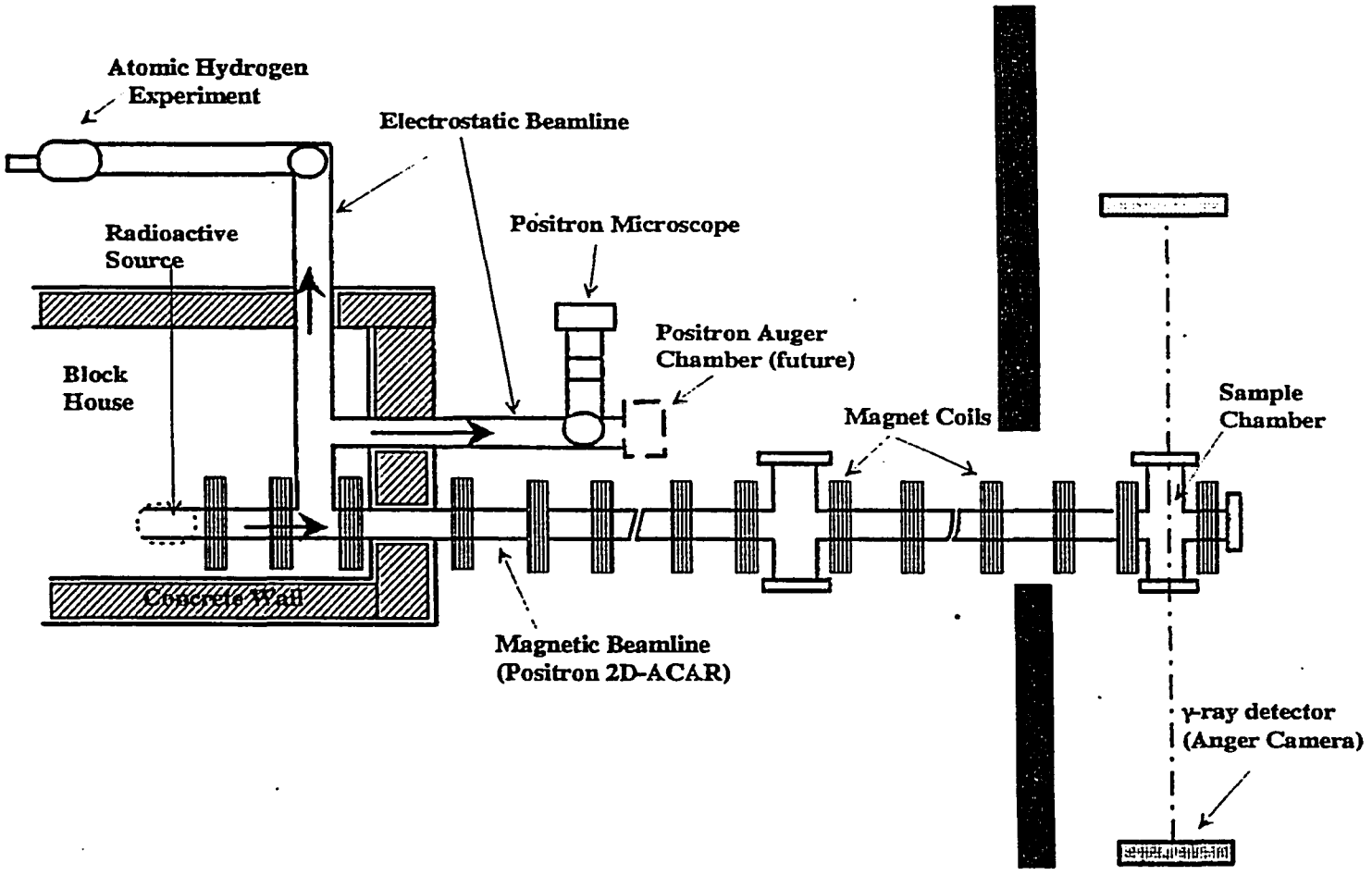

Figure 3.5: The outline of beamlines in the slow positron facility

thermal neutron. The thermal neutron irradiated copper Bee-Bee (^{64}Cu with a total activity of 60 $\sim$ 90 Ci) is then transported to the experiment site and dropped into a crucible which sits inside the source chamber which is under ultrahigh vacuum. After heating the crucible to $\sim$ 1200°C the copper Bee-Bee is evaporated and deposited on the surface of the source holder which is located right above the crucible. The β^+ decay of the radioactive ^{64}Cu will produce fast positrons. Figure 3.6 gives the decay scheme of the ^{64}Cu and the energy spectrum of the emitted positrons.

The number of positrons emitted from the layer of ^{64}Cu coated on the source holder can be estimated from the activity of the ^{64}Cu. It was calculated that the maximum number of positrons getting out of the surface of the Cu layer is $\sim 10^{10} e^+/cm^2$[75]. These positrons was defined as fast positrons due to the large energy spread (see figure 3.6).

To do the depth resolved measurement for the layered systems, the positrons emitted from the ^{64}Cu have to be slowed down to get a relatively monoenergetic positron beam with a reasonable intensity. This slowing down process is called moderation of fast positrons and the materials used to moderate the fast positrons are called moderators which are the heart of slow positron beam. The idea of moderation of fast positron from a radioactive source was initiated by Madanski[13] about forty years ago. A large amount of work had been done to develop various moderators[76]. It was considered that the idea of 'negative' work function of positrons in some metals (or alloys) created by Groce *et al*[77, 78] was a great breakthrough in the development of slow positron beam. Up to present, the commonly used moderators are W(100) thin film and Cu single crystal (self-moderation), using the idea of negative work function of positrons. The general moderation efficiency (defined as the ratio of the number of the slow positrons coming out of the moderator to the number of

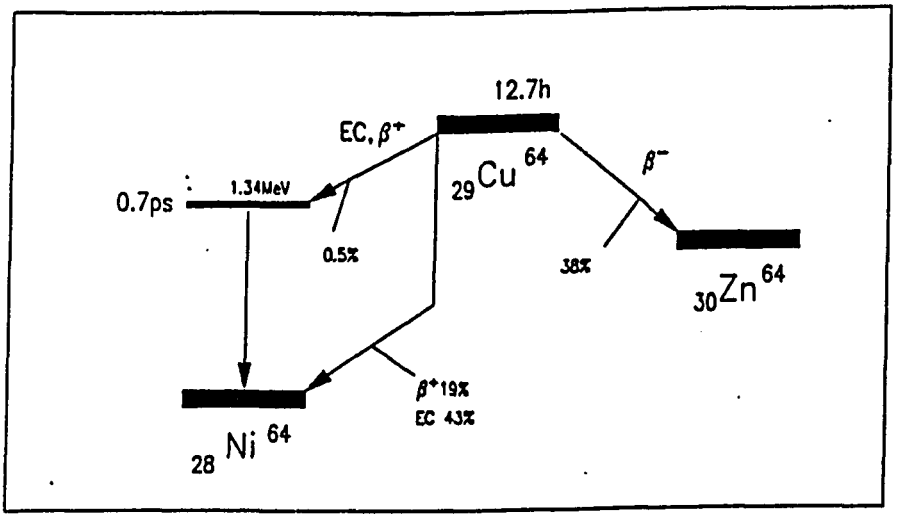

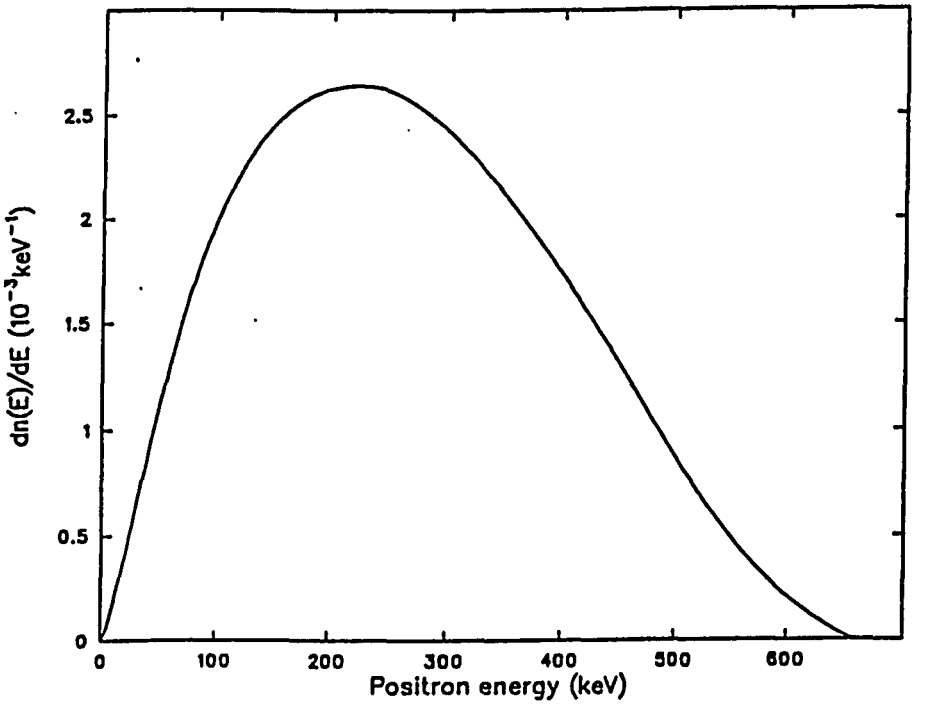

Figure 3.6: The decay scheme of ^{64}Cu isotope and the β^+ spectrum.

the incident fast positrons) is on the order of $10^{-4} \sim 10^{-3}$ with high quality of single crystal and clean surface (to reduce the trapping of the thermalized positrons into defects). The detailed discussion of various moderators can be found in ref.[76]. In last few years, another idea was created by Mills et al[79] that the rare gas solid (Ne, Ar, Kr, Xe) can be used as positron moderators with a much higher efficiency (at least an order of magnitude higher than metal moderators), due to the incomplete thermalization of the incident positrons because of the large band-gap and lack of the optical phonons in the crystals with a single atom basis. Although the mechanism of rare gas moderators is not fully understood yet and there are still some difficulties in controlling the quality of the rare gas solids (not quite crystallized), the efficiency of over 1% had been reported by Khatri *et al*[80] with a Ne moderator. Although the metal moderators have a relatively lower positron yield (or moderation efficiency), the energy spread of the re-emitted positrons from metal moderators is better than that from the rare gas moderators.

In our experiment, the moderator used to produce slow positrons is the solid krypton, which means that the source holder has to be cooled down to $\sim 30K$ after the Cu evaporation. When it is at that temperature Kr gas injected from outside the vacuum chamber can form a layer of a few tens of microns solid on the surface of the positron source. It has been measured that the energy spread of the Kr moderated slow positrons is $10 \sim 15$ eV, while for the self-moderated positrons (measured before injecting the Kr into source chamber is $1 \sim 2$ eV, both numbers seem larger than those reported by other workers. The reason for the larger energy spread for the self-moderated positrons is probably due to the low quality of Cu single crystal because no annealing (should be up to 700°C) is applicable in the source chamber, same may be true for the higher energy spread for the Kr moderated positrons because of the

lack of the experimental data and the capability of controlling the quality of the moderator. By two years of testing and working, the beam intensity has reached $10^8 e^+/sec$ from the $2 \times 10^7 e^+/sec$ at the beginning, although the intensity is still a factor of $3 \sim 5$ lower than that expected from calculation (assuming the moderator efficiency of 0.75% and the effective source area of 4 cm^2). The work on improving the procedure of Cu evaporation and the growing of the rare gas moderator is still going on.

3.2.2 Beamline-Transportation of the Slow Positrons

Once the fast positrons from ^{64}Cu source are moderated, the slow positrons from the surface of the moderator, with an energy in the order of eV, are then extracted out by floating the moderator (and the source holder) to a positive potential (usually floated to 100 volts) relative to the grid (90% transmission) in the front of the moderator. The beamline is grounded (The energy spread of the slow positrons were measured by putting retarding voltages on the grid.). So the energy of the slow positrons in the beamline is about 100 eV. An axial magnetic field was produced by a series of coils along the beamline. The source chamber and the beginning section of the beamline was shielded inside a blockhouse which was constructed with a 3 foot thick concrete blocks and lead bricks wall to prevent the γ-rays coming out the source region. Thus the whole beamline can be divided into three segments: inside the blockhouse, outside the blockhouse and the sample chamber. Figure 3.7 illustrates the part inside the blockhouse. The geometry of the source holder is just a flat surface (although some other geometries were tested, but the flat face geometry gives better yield) with an effective area of $\sim$ 4 cm^2, located inside the thermal shielding of the three stage refrigerator which can cool the source down to 6 Kelvin. With an axial magnetic field

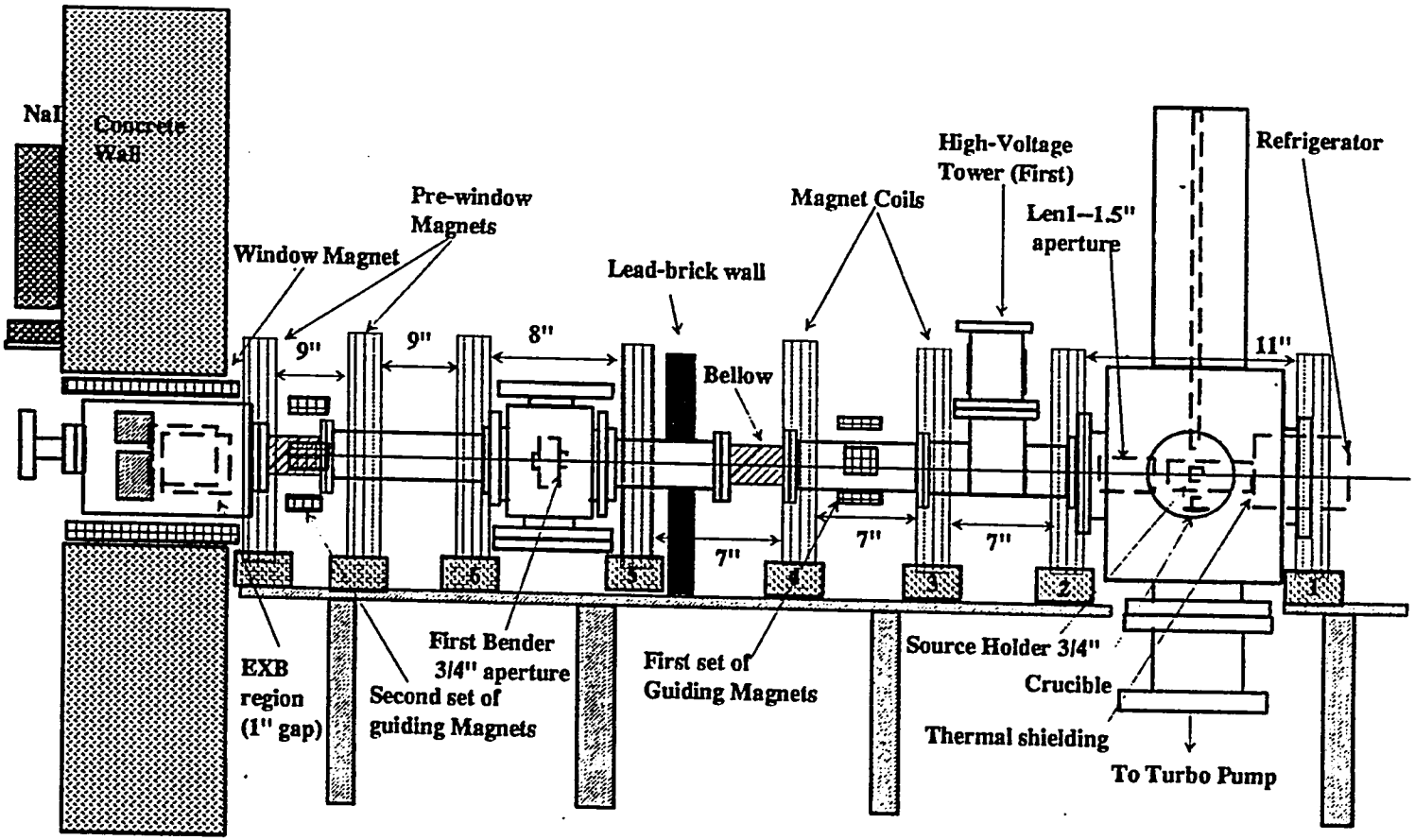

Figure 3.7: The part of the beamline inside the blockhouse

of $\sim$ 200 gauss, the beam size is $\sim$ 1 inch. Owing to the incomplete thermalization of the incident fast positrons in the rare gas moderators, there are still a large fraction of fast positrons (with energies above 100 eV). Next to the thermal shielding is the series of electrostatic lenses for the electrostatic beamline with diameter of the lenses of 1.5 inches. The segment from the source to the bender chamber (see figure 3.7) is shared by magnetic beamline and the electrostatic beamline (all the lens elements would be grounded when the magnetic beamline is running). The aperture of the bender elements for the electrostatic beamline is $\sim \frac{3}{4}$ inches which was used to bend the beam 90 degree to the positron re-emission microscope (PRM) or atomic physics chamber (see figure 3.5) when running the electrostatic beamline. The existence of the small aperture increases the difficulties of tuning-up the magnetic beam and may represent a source of losing positrons. The first set of guiding magnets produces a vertical and a horizontal field to move the positron beam up-and-down and left-and-right in that small region to make the beam through the bender aperture. After the positron beam passes through the bender region, it will enter the first E $\times$B region which consists of a pair of parallel stainless steel plates of 14 inches long sitting in the center of the beamline tubing and with a $\sim$ 1 inch gap between the two plates, and a block of heavy-metal with a hole of $\sim$ 1 inch in diameter and off centered by 1 inch parallel to the plates. The purpose of the E$\times$B region is to filter out the high energy part of the positrons (sometimes the E$\times$B region was called EXB energy analyzer), due to the incomplete moderation by the moderator, to reduce the background on the γ-ray detectors. The EXB method is almost a common practice in operating the slow charged particle beam. The principle of the EXB filtering is: by applying a voltage across the plates, there will be a electric field pointing from one plate to another. Thus, there will be a magnetic field along the beamline direction and an electric field

perpendicular to the beam direction. When the positrons come into the plates region and experience the Lorentz force

$$\vec{F} = \frac{e}{c}(\vec{E} + \vec{V} \times \vec{B}) \tag{3.1}$$

where $\vec{V}$ is the initial speed of the positrons, they will acquire an extra motion with a velocity $\vec{v} \propto \frac{(\vec{E}\times\vec{B})}{B^2}$, which is independent of the initial speed of the positrons and move the positron beam off centered. The distance of the beam off the center of the beamline, d, is

$$d \propto \mid v \mid \frac{l}{\sqrt{\epsilon}} \tag{3.2}$$

where l is the length of the EXB plates (=14 inches) and ϵ is the initial energy of the positrons getting into the EXB region (e.g. for the 100 eV positron beam with $\sim$ 150 gauss axial magnetic field in the center, 50 $\sim$ 60 V across the plates is necessary to move the beam 1 inch off-centered). Thus, by adjusting the voltage across the plates, the high energy fraction of the positrons can be filtered out. The slow positrons coming out of the blockhouse window will enter the beamline outside the blockhouse off centered 1 inch still because the whole beamline (inside and outside blockhouse) was well aligned to each other. Then the beam will be moved back to the center of the beamline by the second set of EXB which is parallel to the first one but with opposite polarity of the electric field between the plates and was positioned $\sim$ 1 meter downstream of the beamline from the blockhouse window. It is worthwhile to mention that the axial magnetic field is strong (160 $\pm$ 20 gauss) and the effect of the earth magnetic field was compensated by a set of steering magnets located in the middle of the beamline outside the blockhouse.

3.2.3 Sample Chamber

Figure 3.8 shows the setup for the sample chamber at the end of the beamline. As the slow positrons with an energy of $\sim 100eV$ were transported to the sample chamber, they will be accelerated to the required energies before hitting the sample. The small two stage accelerator consists of two lenses made of three copper tubings each with a diameter of 2 inches. The first tubing was always grounded, and the middle one was kept at medium potential while the last tubing was floated to the required potential (negative). The sample itself was floated to the same potential as the last tubing of the accelerator. Although the lenses themselves has the focusing capability, two permanent ring magnets were used to further focus the beam: one was positioned at the end of the last tubing with a field of $\sim$ 500 gauss in the center and the other was positioned in the back of the sample with a field of 4000 $\sim$ 5000 gauss in the center (The effect of magnetic reflection is small for the positron energy of above 1 keV). Generally speaking, the beam size is inversely proportional to the square root of the magnetic field, which can be understood quantum mechanically that the degeneracy of each Landau level for particle moving along a magnetic field is $\frac{2e}{hc}BA$[81], where B is the field strength and A is the cross section of the beam, thus, for a fixed beam intensity the BA is a constant. Therefore, the beam was focused to the sample surface from a $\sim$ 1 inch down to 5 $\sim$ 7 mm in diameter. This was observed by using an Micro-Channel-Plate. The sample was mounted in a manipulator with X-Y-Z three stage linear motion and a rotation about the Z axis so that it can be well aligned to the center line of the two γ-ray detectors–Anger Cameras. The chamber was not equipped with cooling function yet. So the 2D-ACAR measurements were done at room temperature.

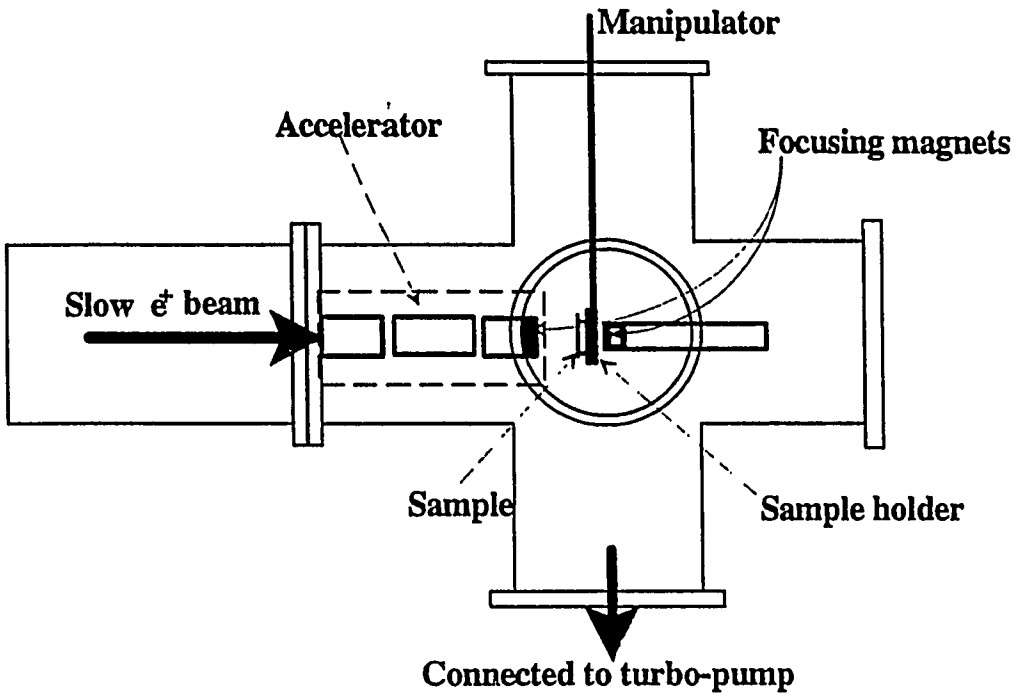

Figure 3.8: The side view of the sample chamber for the beamline.

3.3 Anger Camera

The two γ-rays from each annihilation of the $e^+ - e^-$ pair are detected by two position sensitive γ-ray detectors called Anger Cameras. Each detector consists of a NaI single crystal in the front and an array of 91 photomultiplier tubes in the back. The dimension of the NaI crystal is ~50 cm in diameter and ~1.3 cm thick. The solid angle covered by the detector is approximately

$$\omega = \frac{\pi}{16d^2} \tag{3.3}$$

where d is the distance from sample to the center of the detector, in meters. In our measurements, d ranges usually from 8 to 15 meters, which results that ω is about a few tens of milliradians. A high-energy (~511 keV) photon impinging on the NaI single crystal produces light photons which then activate the surrounding photomultiplier tubes which are couple to the crystal optically such that the nearest tube yield the largest signal whereas tubes further away give smaller pulses. The sum of the voltage output from the activated PM tubes yield the energy of the detected photon, E. To obtain the position of the incident photon, the output from the PM tubes are fed into a resistor network, where each PM tube is associated with four resistors whose values produce voltage outputs proportional to the position of the tube from four calibration points on the detector, respectively. These voltages are coupled to yield a set of four analogue coordinates (X^+, X^-, Y^+, Y^-) that represents the position of the incident photon with respect to the calibration points.

Each detector is linked to a General Electric Starport system[82] and an online computer. When each set of analogue signals arrives at the Analog Control Board within the Starport system, it is accepted only if the energy pulse is above some

threshold limit so as to remove unwanted low amplitude events produced by multiple reflections in the crystal and the pulse does not have an asymmetric shape due to the pile-up. The accepted signals are then passed to the analog-digit converter where each coordinate set is first normalized by dividing each value within the set by a value proportional to E. This procedure yields constant amplitudes regardless of the statistical fluctuations in the NaI crystal and the PM tubes that would otherwise produce different values for photons hitting the crystal at the same position. The normalized (X^+, X^-, Y^+, Y^-) are converted to (X,Y) by differential amplifiers, respectively. The (X,Y,E) signals are subsequently digitized before they are passed to the correction board which provides linearity and energy correction matrices to compensate for inherent imperfections in the detectors. These correction matrices are actually "look-up" tables acquired empirically from the calibration procedures described elsewhere[11, 42], and they provide appropriate values that are added to the digitized (X,Y,E) signals. The corrected signals are subject to spatial and energy discriminations, whereby only signals with spatial and energy within the respective user-defined windows are retained. In our measurements, the energy window is set at $\pm 20\%$ of the 511 keV photopeak, and the spatial window corresponds to an effective circular area of diameter of 45 cm on the detector face. Those accepted signals are then displayed on the respective monitors of the Starport systems, and at the same time passed to a coincidence circuit in an on-line computer. A pair of signals from the detectors are considered to be in coincidence when they arrive at the circuit within the time window (time resolution of the coincidence circuit) which is $1 \sim 2\mu$s. For a pair of coincident signals, (X_i, Y_i, E_i), i=1,2, the coincidence signal (x_c, y_c), in unit of channels (or pixels), is given by

$$x_c = \frac{(X_1 + X_2)}{2} \tag{3.4}$$

and

$$y_c = \frac{(Y_1 + Y_2)}{2} \tag{3.5}$$

which are stored in the on-line computer. The output from the on-line computer are two-dimensional matrices which are usually downloaded every few hours so that any change on the system (for example, sample and the aquisition system) can be monitored. The data files are usually analysed on a VAX mainframe computer. The procedure of the data analysis will be discussed in the next chapter.

3.4 Angular Resolution of the system

The angular resolution of the system is determined by the following factors:

1) The intrinsic spatial resolution of the detector.

2) The spot size of the positron beam hitting the sample.

3) The distance between the sample and the detector.

For our detector system, the spatial resolution is about 3 mm (factory specified), which is limited by the contemporary technology. The spot size of positron beam for the bulk chamber is $\sim$ 4 mm and for the interface chamber it is 5 $\sim$ 7 mm. So these two factors are fixed and the only factor variable is the distance from sample to the detector. To get good angular resolution, we have to move the detector far away from sample and result in a lower count rate. In the experiment, there always is a compromise on the resolution and the count rate. The requirement of the resolution depends on what structure we want to measure. Although there is standard procedure to obtain the angular resolution of the system (by putting the phantom plate with thin slots in the front of detector and calculating the Fourier transform of the image of the slot) discussed by Chan[42], the easier way to obtain the angular resolution

is to measure the width (in fact, the Full Width at Half Maximum or FWHM) of the para-Positronium signal from the 2D-ACAR spectrum of quartz single crystal (or ice single crystal[83]) in which the Ps atoms stay at the bottom of the conduction band with a crystal momentum of $\vec{k} \approx 0$. Figure 2.3 gives the 2D-ACAR spectrum of a α-quartz from the bulk chamber at a sample-detector distance of $\sim$ 15 meters at a temperature of 20 $\sim$ 30 K, giving rise to the angular resolution of the bulk measurement at that setup and temperature. While Figure 3.9 gives the 2D-ACAR spectrum of the α-quartz measured from the interface chamber at room temperature and with a sample-detector distance of $\sim$ 8 meters.

The angular resolution of the two systems can be calculated from these two spectra. The angular resolution of the system, σ_r, is,

$$\sigma_r^2 = \sigma_q^2 - \sigma_T^2 \tag{3.6}$$

where, σ_q is the FWHM of the para-Ps peak in the 2D-ACAR spectrum, and σ_T is the term originated from the thermal motion of the Ps atoms, given by

$$\sigma_T = \sqrt{1.665 m^* kT} \tag{3.7}$$

where k is the Boltzmann constant and m^* is the effective mass of Ps atom ($\approx 3m_e$[84], where m_e is the electron rest mass). For the bulk chamber setup, the overall angular resolution is $\sim$ 0.5 $\times$ 0.5 milliradian^2(mrad^2). While for the interface chamber, the overall angular resolution is $\sim$ 1.3 $\times$ 1.3 mrad^2.

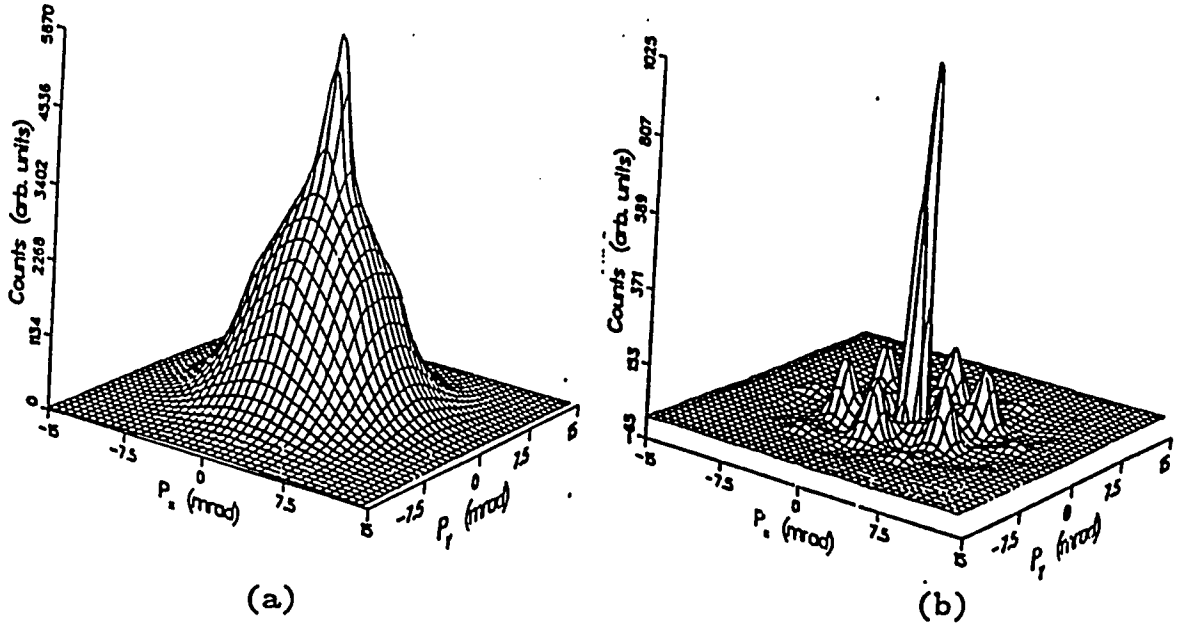

Figure 3.9: The 2D-ACAR spectrum of α-quartz single crystal from the high-intensity beamline chamber to obtain the angular resolution of the system, measured at room temperature with a sample-detector distance of $\sim$ 8 meters which is the situation for the real experiment. (a) The original spectrum. (b) After the subtraction of the broad component (see the discussion given in sect. 4.2).

Chapter 4

Procedure of Data Analysis

Once the positron 2D-ACAR spectrum is acquisited, the raw data are analysed by certain schemes to extract the physical information behind the data. There are some differences between the schemes of data analysis for bulk measurement and interface measurement. The following scheme is basic in the data analysis for both of the bulk and interface studies:

1) Apply the camera correction function to the raw spectrum;

2) Determine the position of $\vec{p} = 0$ and center the spectrum;

3) Determine the rotation angle and rotate the spectrum;

4) Smooth the spectrum to convolute the spectrum with the resolution;

5) Symmetrize the spectrum (when allowed).

For the bulk measurement, it is necessary to get the anisotropy of the spectrum to judge the quality of the single crystal, which comes from the delocalized positron annihilation with valence or conduction electrons.

For the interface measurements, we have to go three more steps to get information from the data:

1)Find out the positron annihilation fractions at different beam energies;

2)Get the net spectra for position annihilating at different layers;

3)Remove the broad component from each spectrum to see the fine structure (when necessary).

A more detailed explanation to each step is given below.

4.1 The Basic Procedure of the Data Analysis

4.1.1 The Camera Correction Function

The two γ-ray detectors, Anger Cameras, are not point detectors. Instead, each detector represents a detection area of $\sim 0.25\pi$ m^2. For the coincidence measurements with two cameras, the detection efficiency for the two γ-rays with small angle between them is significantly higher than the efficiency for the two γ-rays with larger angle between them. West *et al*[11] had given a detailed discussion on this subject. It is shown that in a particular case in which the camera adjustments are assumed to be exceedingly successful and the linearity is hence perfect, the recorded 2D-ACAR spectrum of a delta momentum density $\delta(\vec{p''} - \vec{p'})$ takes the simple form

$$N_\delta(\vec{p}, \vec{p'}) = M(\vec{p})R(\mid \vec{p} - \vec{p'} \mid) \tag{4.1}$$

where

$$M(\vec{p}) = \int \epsilon_1(\vec{p} + \frac{\vec{p'}}{2})\epsilon_2(\vec{p} - \frac{\vec{p'}}{2})d\vec{p'} \tag{4.2}$$

is the camera correction function or called momentum sampling function, ϵ_i is the efficiency function of camera i (i=1,2) and the integral is taken over all space, and $R(\vec{p} - \vec{p'})$ is the two dimensional detector's resolution function which is homogeneous, i.e. $R(\vec{p} - \vec{p'}) = R(\mid \vec{p} - \vec{p'} \mid)$.

Positron 2D-ACAR measures the momentum density function $\varrho(\vec{p})$ projected along a given direction p_z:

$$N(p_x, p_y) = \int R(\vec{p})\varrho(\vec{p})dp_z \tag{4.3}$$

The recorded spectrum of a general momentum density is, therefore, the convolution of $\varrho(\vec{p})$ with $N_\delta(\vec{p}, \vec{p'})$. Thus, eq. 4.3 implies implicitly that the measured spectrum is the real momentum density function multiplied by the detector's correction function. To show the real momentum distribution, the measured spectrum has to be divided by the correction function.

A true single camera efficiency $\epsilon(\vec{p})$ can be measured by the setup similar to the real data acquisition setup: ^{22}Na radioactive source with a sample in the front. To measure the efficiency of camera 1, it is positioned to the distance at which a real measurement will take place and the signals being collected are gated by the coincidence events detected by camera 2 to discriminate the background. Generally, camera 2 is set closer to the source to ensure larger subtending solid angle. Similar measurement is also performed for camera 2 to obtain its efficiency. The correction function is then obtained from the overlapping integral of the two measured efficiency functions.

Figure 4.1(a) shows the three-dimensional plot of the correction function and (b) shows the correction effect of the camera's correction function on the shape of data.

The corner on the top center of the correction function is due to the equal distance of the two detector from the sample, which makes the alignment of the system very difficult and may arguably cause some small artifacts in the data when applying the correction matrix. To avoid this, some workers set the detectors at non-equal distance from the sample, i.e. make a $10 \sim 15\%$ offset of the distances. Although all of the data in this thesis were taken at equal distance setup, no any obvious artifacts were

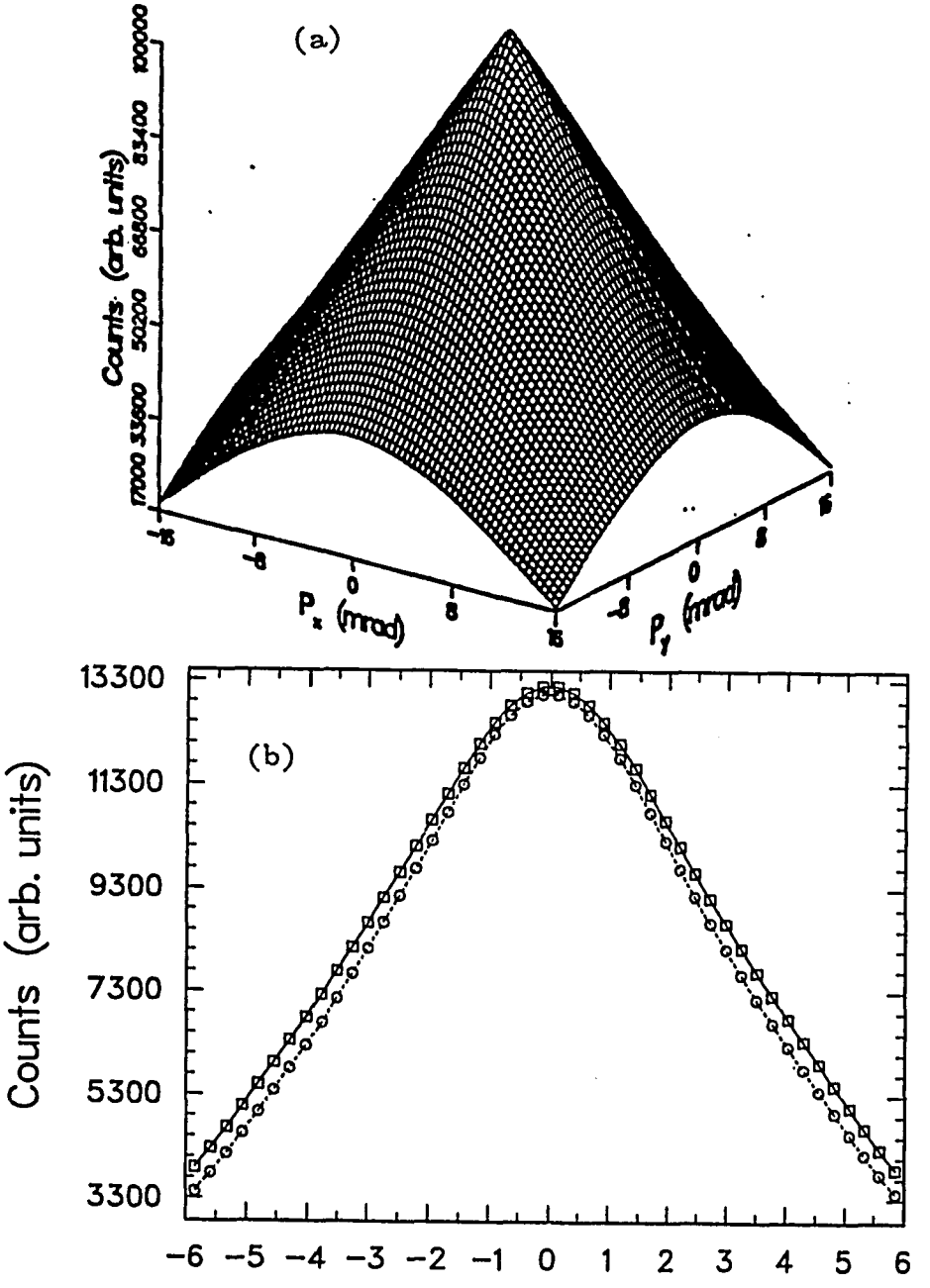

Figure 4.1: (a) Camera's correction function. (b) The comparison of data before and after the implementation of the correction function: solid line–after the correction; dashed line–without correction.

seen yet (see the spectrum shown in figures 5.12 and 6.9). This may be due to our careful alignment of the sample relative to the detector for each measurement.

4.1.2 Centering the Spectrum

In position 2D-ACAR measurement, the annihilation source (sample) which is positioned at the mid point of the axis joining the center of the cameras should be aligned very well with the center line of the two cameras. In an ideal case of perfect alignment, the point $\vec{p} = 0$ in the spectrum will coincide with the origin of the detectors coincidence field coordinate system. Any small shift of the source from the center line of the cameras will result twice the shift of the position of $\vec{p} = 0$ from the origin of the coincidence field. The coincidence of the point $\vec{p} = 0$ with the origin of the coincidence field is crucial for the symmetrization of the spectrum. A physical alignment to a very high accuracy is usually not trivial and almost impossible. Thus it usually happens that the point of $\vec{p} = 0$ of the spectrum deviates one or two channels from the origin of the detectors coincidence field and in the data analysis we have to shift the spectrum to make the point of $\vec{p} = 0$ coincide with the origin of the coincidence field. The relative position of $\vec{p} = 0$ point of the spectrum in the coincidence field coordinate system (a matrix) is defined by the first moments, $(\bar{p}_x, \bar{p}_y)$, given by

$$\bar{p}_x \sum_{allpts} N(p_x, p_y) = \sum_{allpts} p_x N(p_x, p_y) \tag{4.4}$$

and

$$\bar{p}_y \sum_{allpts} N(p_x, p_y) = \sum_{allpts} p_y N(p_x, p_y) \tag{4.5}$$

Since the first moments do not necessarily occur at whole or half channel, a linear interpolation scheme is used, yielding an accuracy of ± 0.03 channel for each of the x and y centering.

4.1.3 Rotation of the Spectrum

The purpose of this operation is to correct for any misalignment of the crystal in the $p_x p_y$ plane, *i.e.*, the rotation angle of the crystal about the axis joining the centers of the two detectors. For a well aligned system, the p_x direction of the spectrum will be in the x direction of the coincidence field coordinate system and similarly p_y will be in the y direction. But in the real experiment, there is sometimes an angle between the p_x and x. This angle can be determined by a χ^2 analysis of the raw spectrum. Since we study the bulk or interface properties of the samples the 2D-ACAR spectra have at least two-fold symmetry (will be discussed in the next subsection). We first consider the reflection about p_x=0. After a θ^o rotation of the spectrum about the origin($p_x = 0, p_y = 0$), we compute the χ_2 defined as:

$$\chi^2(\theta) = \frac{1}{M-1} \sum_{k=1}^{M} \frac{(N_k' - N_k)^2}{N_k} \tag{4.6}$$

where N_k and N_k' denote counts at the points symmetric about the reflection axis, p_x=0. In the data analysis, we usually restrict the summation of the momentum positions, represented by k, to the range $0 \leq k \leq$ 8mrad to exclude the positions with zero counts. Figure 4.2 shows the plot of χ^2 versus angle θ. We can get an identical curve for the reflection about p_y=0. The minimum point occurs at 4.8°, which is the required angle of rotation of the spectrum.

4.1.4 Gaussian Smoothing

After correcting for the misalignment in the (p_x, p_y) plane, the rotated spectrum is smoothed with a gaussian with a full width at half maximum (FWHM) equal to the experimental resolution which has been discussed in section 3.4. The gaussian smoothing operation does not introduce any artifacts to the spectrum[42]. Figure 4.3

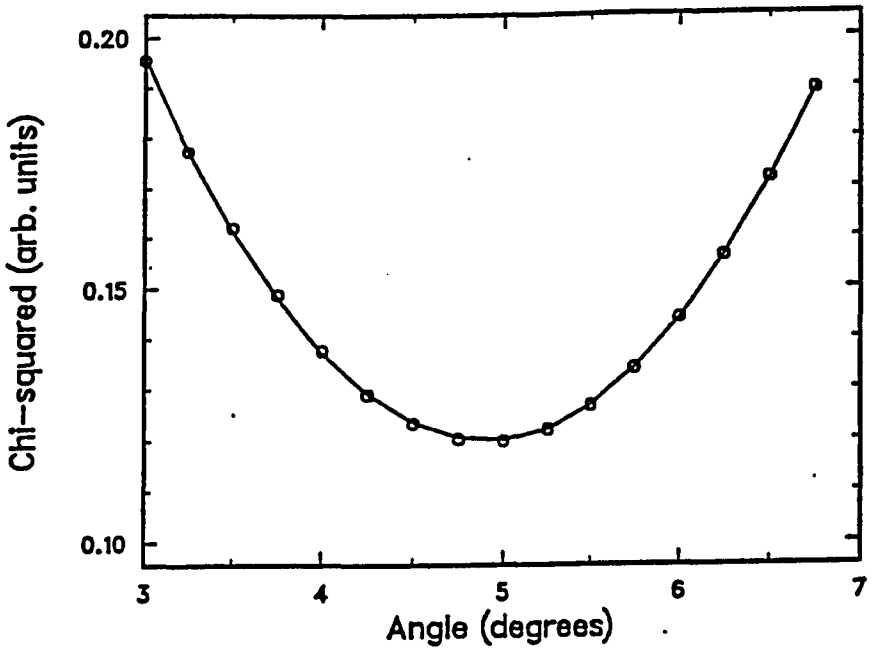

Figure 4.2: The plot of χ^2 versus angle of rotation.

show the 1D plot of the 2D-ACAR spectrum with and without gaussian smoothing.

4.1.5 Symmetrization

Positron 2D-ACAR measures the $e^+ - e^-$ pair momentum distribution inside materials. The symmetry of the 2D-ACAR spectrum is determined by the momentum density of electrons (or $e^+ - e^-$ pairs). Under static condition, i.e. there is no constant current (in microscopic scale) pass through the sample during the measurement, all the electrons are moving in the closed orbits or trajectories in momentum space. In quantum mechanics[85], the Schrödinger equation has time-reversal-symmetry, i.e. the solution, $\psi(\vec{p})$ and $\psi(-\vec{p})$ only differ by a phase factor ($e^{\pm i\frac{Et}{\hbar}}$, where E is the eigenvalue of the equation). Therefore the momentum density of electrons $\varrho(\vec{p}) = \varrho(-\vec{p})$, which indicates that the 2D-ACAR spectrum has at least 2-fold symmetry. But in

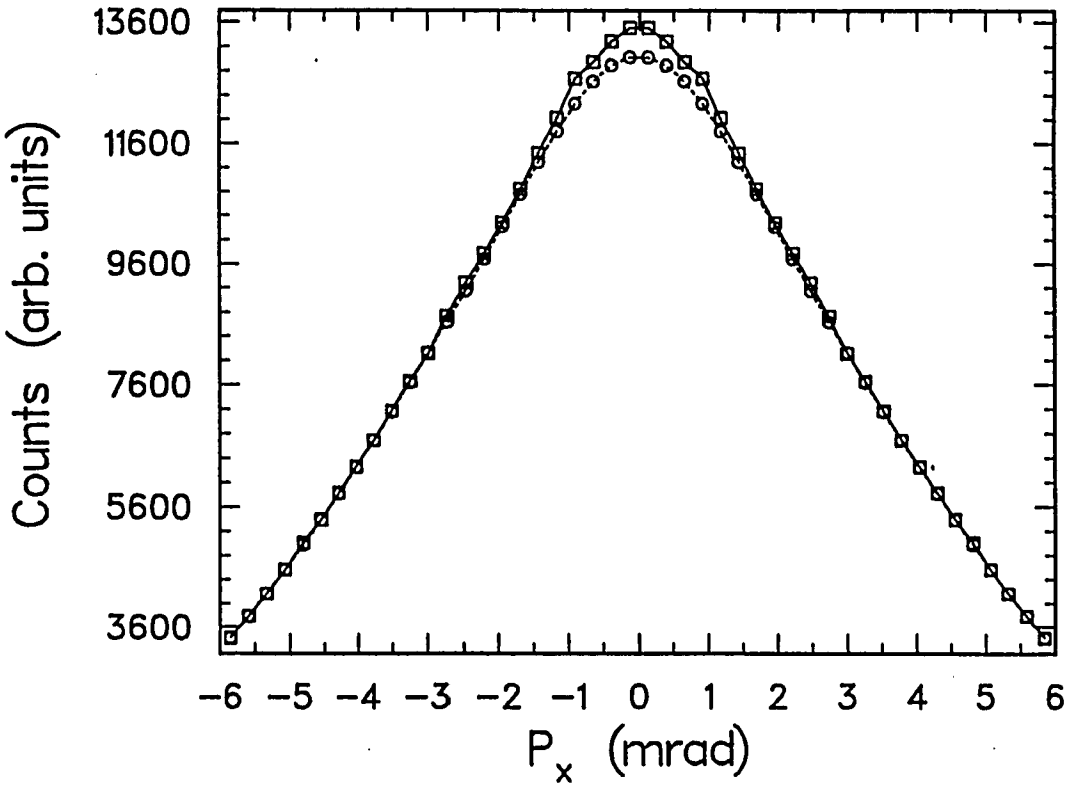

Figure 4.3: The effect of gaussian smoothing: solid line–no gaussian smoothing; dashed line–with gaussian smoothing.

the case of Ps emission from surface of materials, the 2D-ACAR spectrum is not symmetric in the emission direction (in this case, the Ps atoms are not moving in a closed trajectories in momentum space.). A detailed discussion of positron study of surface of metal and semiconductors has been given by Chen[20].

In a semiconductor single crystal, the thermalized positrons will annihilate with valence electrons and core electrons. In 2D-ACAR spectrum, the contribution from positron annihilation with core electrons will be averaged and be isotropic because the periodic potential of the lattice has no effect on the motion of core electrons. But the momentum of the valence electrons will be decided by the periodic potential of the lattice, i.e., reflects the symmetry of the reciprocal lattice of the single crystal. The contribution from positron annihilation with valence electrons to the 2D-ACAR spectrum is anisotropic and the shape of the contribution reflects the geometry of the first Brillioun zone projected along the integration direction which is usually coincident with a major crystallographic direction.

4.2 Data Analysis for the Bulk Measurement

For the bulk measurements, generally speaking, it is necessary to find out the quality of the crystal by the anisotropy analysis and then find out the fraction of positron annihilation with the single crystal and remove it to see the spectrum for positron annihilation at defects. The anisotropy analysis some times is used to highlight the fine structures in the spectrum by subtracting the broad symmetric component. The broad isotropic component, $N_i(p_x, p_y)$, is defined as the Gaussian smoothed "radial angular average", $N_r(p_r)$. For every $p_r = \sqrt{p_x^2 + p_y^2}$, $N_r(p_r)$ is given by:

$$N_r(p_r) = \frac{\sum_{k=1}^{n} N(p_{xk}, p_{yk})}{n} \tag{4.7}$$

where each (p_{xk}, p_{yk}) (n of them) lie on the circle of radius p_r. Here the gaussian smoothing is performed with a FWHM of $2 \sim 3$ times larger than the angular resolution of the system to ensure that it is really "broad". The anisotropy is then defined as

$$N_a(p_x, p_y) = N(p_x, p_y) - N_i(p_x, p_y) \tag{4.8}$$

Note that the gaussian smoothing of the $N_r(p_r)$ is not necessary for the anisotropy analysis. It is just a preliminary way of defining the broad isotropic component in highlighting the fine structure in original spectrum.

In the data analysis for the interface measurement, we usually use this method to define the fine structure. But in that case the fine structure is different from the true anisotropy and it may give some artifacts in the quantitative interpretation (mainly causing some change in the width of Ps atoms signal). Thus we just use this method to show the existence of the structure and use another method to give quantitative interpretation of the data (a few Gaussian fit to the data).

4.3 Data Analysis for the Interface Measurement

With utilizing the slow positron beam, the positrons can be implanted to appropriate depth to probe different layers of the sample. The implantation profile for monoenergetic slow positron beam has been given in section 1.2. The behavior of the thermalized positron can be well described by the diffusion equation[25, 86]:

$$\frac{\partial n(z,t)}{\partial t} = D\frac{\partial^2 n(z,t)}{\partial z^2} - \epsilon e\frac{d}{kT}\frac{\partial n(z,t)}{\partial z} - \frac{n(z,t)}{\tau_{eff}} + \dot{n}(z) \tag{4.9}$$

where n(z,t) is the positron density at depth z and time t, D is the positron diffusion coefficient, T the temperature, ϵ the electric field,e the positron charge, k the Boltzmann's constant, $\dot{n}(z)$ the rate at which thermalized positrons are being implanted

at depth z, and τ_{eff} is the effective lifetime of the positrons in the sample, given in section 1.8. A theoretical study of the validity of the diffusion model was given by McMullen[87]. The breakdown and the limitation of the diffusion model were discussed by Brandt et al[88] and Lynn et al[89], and are reviewed in several statistics textbooks[90, 91].

In steady state, $\frac{\partial n(z,t)}{\partial t} = 0$, the time dependent diffusion equation can be reduced to an ordinary linear second-order differential equation,

$$\frac{d^2n(z)}{dz^2} - \frac{1}{\Lambda}\frac{dn(z)}{dz} - \frac{n(z)}{L^2} + \frac{\dot{n}_0(z)}{D} = 0 \qquad (4.10)$$

where $L \equiv (D\tau_{eff})^{1/2}$ is the positron diffusion length and $\Lambda \equiv \frac{kT}{ee}$ is a parameter with the dimension of length characterizing the effect of electric field (In the case of metal, Λ becomes infinity and the second term of the equation becomes zero). The solution and discussion to eq. 4.10 can be found elsewhere[49].

Usually, before we perform the positron 2D-ACAR measurement using high-intensity slow positron beam to get detailed information for a specific layered system, we make the positron Doppler broadening (S-parameter) measurement for the system using a relatively low intensity positron beam in which a ^{22}Na radioactive source and a W(100) thin film moderator was employed as slow positron source. The intensity of the beam is about $5 \times 10^5 e^+$/sec. The detailed description of the beamline can be found elsewhere[92]. The principle of positron Doppler broadening measurement has been given in section 1.5. Figure 1.3 shows the principle setup for Doppler Broadening measurement. The recorded energy spectrum of the annihilation photons by the High-purity Ge detector which was positioned right behind the sample was shown in figure 4.4., due to the motion of the $e^+ - e^-$ pair and the finite energy resolution of the detector (in the ideal case of infinite resolution of the detector and the annihilating $e^+ - e^-$ pair at rest, the spectrum would have been a δ function with

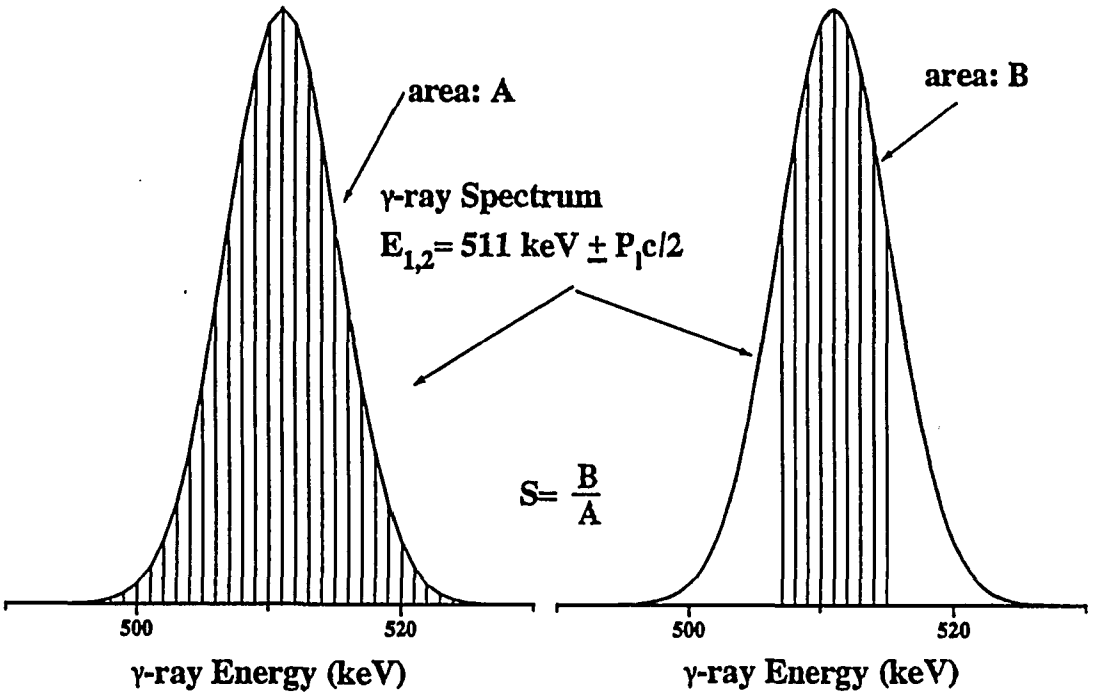

Figure 4.4: The definition of the S-parameter.

a value at 511 keV.). The S-parameter (or line-shape parameter) is the practice of quantifying the Doppler broadening, first introduced by MacKenzie *et al*[93] and its detailed discussion were given by Campbell [94] and Schultz *et al*[95]. The definition of the S-parameter is shown in figure 4.4. It is defined as the ratio between the sum of the counts in a central region (area B) and the total counts (area A) of the energy spectrum recorded by a multi-channel analyzer (MCA), i.e.,

$$S = \frac{B}{A} \tag{4.11}$$

Generally speaking, the higher the momentum of the annihilating $e^+ - e^-$ pair is, the

greater is the broadening of the spectrum and the lower is the S-parameter, and vise versa. The central region is defined by the energy window of the MCA and was set that in bulk silicon single crystal S $\approx$ 0.5 for the optimum sensitivity.

As a preliminary approach in the study of the multilayer structures, each layer is assumed to be homogeneous but distinctive from other layers. The resultant S is the average of the S values of the various layers weighted by the respective annihilation fraction, f, i.e.

$$S = \sum_{i=0}^{N} S_i f_i \tag{4.12}$$

for an N-layer system, where S_i and f_i are the S-parameter of the i^{th} layer and the fraction of positrons annihilating at the i^{th} layer, respectively. The 0^{th} layer (i.e. i=0) represents the surface annihilation. The annihilation fraction, $f_i s$, is an crucial parameter which can not be obtained directly from 2D-ACAR measurement. This is another reason to do the S-parameter measurement before doing 2D-ACAR measurement. A numerical method with an efficient computer code VEPFIT[49] has been developed to determine the fraction, f, by fitting the experimental S vs Energy (S-E) curve. The program VEPFIT solves the eqs. 4.10 and 4.12 by an iteration procedure and is equipped with an adjustable implantation profile and the fitting of S-parameter, diffusion length, electric field and the layer boundaries. A detailed discussion of the S-parameter measurement and the data analysis using VEPFIT to the SiO_2-Si system can be found elsewhere[50, 96].

4.4 Error Analysis

4.4.1 Statistical Error

The statistical error associated with each momentum position, $N(p_x, p_y)$, in the recorded raw spectrum is defined as[97]:

$$\Delta N_{raw}(p_x, p_y) = \sqrt{N_{raw}(p_x, p_y)} \tag{4.13}$$

In the data analysis, the error propagation is carried out by using the quadrature rule, which states that for a derived quantity $z = f(x_1, x_2, \ldots x_n)$ with the x_is are independent variables, the error Δz is given by:

$$(\Delta z)^2 = \sum_{i=1}^{n} (\frac{\partial z}{\partial x_i})^2 (\Delta x_i)^2 \tag{4.14}$$

Thus, for the operation of applying the correction matrix, the error bar for the resultant spectrum, $N_{true}(p_x, p_y)$, is

$$\Delta N_{true}(p_x, p_y) = \sqrt{(\frac{\Delta N_{raw}(p_x, p_y)}{N_{raw}(p_x, p_y)})^2 + (\frac{\Delta M(p_x, p_y)}{M(p_x, py)})^2} N_{true}(p_x, p_y) \tag{4.15}$$

where $M(p_x, p_y)$ is the element of the correction matrix. Due to the very high statistics for the correction matrix ($\approx 10^8$ counts for each camera spectrum), the contribution from this term was generally neglected by other authors[20, 42]. In our data analysis, this small contribution was taken into account.

It is clear that the error propagation rule given above is only valid when the variables, x_is, are independent of each other. This condition is satisfied by almost all of the operations stated in previous sections except the operation of symmetrization. Strictly speaking, the variables are not completely independent (or uncorrelated) after this operation. Although this has been the concerns for long time, there is still no solution yet. The major dilemma is that the symmetrization operation is sometimes

necessary to correct the errors from other sources. To minimize the artifacts on the calculation of the error bar caused by the symmetrization operation, we leave this operation as the last step of the data analysis and only if necessary.

Obviously, the way of reducing the statistical error is to increase the statistics of each spectrum, i.e. increase data acquisition time. Sometimes this is not practical because: first, long time exposure of sample may cause radiation damage to the sample; second, the error from the electronics and other change in environment condition may play a more important role. At least under present experimental condition, the infinitely increasing statistics is not practical.

4.4.2 Other Sources of Error

Besides the statistical error which can be reduced by increasing the statistics to a reasonable level, there are some other errors cause by other factors:

1) Misalignment of the center of the 511 keV γ-ray source to the centerline of the two detectors. This error can be minimized by a careful and time consuming procedure so that the misalignment can be kept in the level of a fraction of 1 mm.

2) Misalignment between the integration direction, p_z, and the direction of the major axis along which the momentum density is supposed to be integrated. By carefully mounting the sample, this misalignment can be kept in the level of $2 \sim 3$ degrees.

3)The intrinsic asymmetry of the detector itself. It was found that there is always a limit of asymmetry in the data, even with extremely careful alignment of the sample and relative position of sample and the detector. We attribute this to the intrinsic asymmetry originated from detector and the setup (for the bulk chamber, it is about 0.3%). Thus, this would force us to symmetrize the data.

4)Temperature fluctuation around the detectors will cause an error because the detection efficiency of the detectors are temperature dependent (In the experiment, we always keep the temperature as constant as possible so that the error caused by temperature fluctuation is negligible.).

4.4.3 Extra Error in the Interface Study

Besides the source of errors discussed above, for the interface measurement using the variable energy positron beam there is new kind of error that may affect our data analysis and the interpretation of the data. This is the error originated from the calculation of the annihilation fraction discussed in the last section. The positron annihilation fractions are calculated from the result of positron S-parameter measurement, using the standard numerical procedure VEPFIT. The error bar of the original data can be defined according to eq. 4.13, but there is no error bars propagation in the procedure VEPFIT. Thus, the result from VEPFIT does not contain error bar. This will increase the difficulties in our analysis. To compensate this, the annihilation fractions are changed by a small amount around the ones calculated from the VEPFIT to see if the structures or features in the spectrum is stable. By this, we have a reasonable estimation of the possible errors in the fractions.

Chapter 5

The SiO_2-Si System

Silicon oxidation is perhaps the most common process in the fabrication of electronic devices. The silicon dioxide-silicon interface (SiO_2-Si) has excellent electrical properties which are employed in field-effect devices and surface passivation. The importance of Si technology in the semiconductor industry is best illustrated by its dominant role in the microelectronics industry. Because of that, a tremendous amount of effort has been devoted to the study of the Si technology since late 1950s. This makes Si technology a most understood and controlled one. Deal *et al*[98] gave a comprehensive review about the evolution in the Si technology. It is generally recognized that the taking off of the silicon semiconductor industry was marked by the discovery of the oxide passivation of the silicon and the introduction of the planar process. Various techniques have been used to study the SiO_2-Si system, especially the interface which has been the subject of intense study because of its dominant role in Si technology. The experimental techniques used to determine the structure of the interface, its extent and its roughness include: transmission electron microscopy (TEM)[71, 99, 100, 101], scanning tunneling microscopy (STM)[101, 102],

low energy electron diffraction (LEED)[103, 104], ellipsometry[105], x-ray scattering [106, 73], x-ray photoelectron spectroscopy (XPS)[107, 108, 109, 110, 111, 112, 113], and positron annihilation[114, 115]. The results range from atomically sharp to extended interfaces of $\sim 10\mathring{A}$ width. These variations in results could be due to the different probing technique or to the differences in sample preparation. For the interface states studies, there are, in fact, very few chemically diagnostic analytical techniques that can reveal the nature of atomic-scale or point defects which are responsible for interface states; the one most suitable for Si and SiO_2 is the Electron Paramagnetic Resonance (EPR)[116, 117, 118] technique. Positron 2D-ACAR is a promising tool in the study of electronic structure of defects. While coupled with a high-intensity monoenergetic slow positron beam, 2D-ACAR can be applied to study the well-studied and poor-understood SiO_2-Si interface, to supply some unique information which is not obtainable by other techniques. In this chapter, we will present our experimental result on positron 2D-ACAR study of the physically and technologically important SiO_2-Si interface. First of all, a brief introduction to Si technology and its surface oxidation will be given.

5.1 Si Single Crystal

The lattice of Si single crystal has a structure of FCC with a two-point basis (0,0,0) and $(\frac{1}{4},\frac{1}{4},\frac{1}{4})$, similar to that of diamond or GaAs. Each Si atom has four nearest neighbors and share a pair of valence electrons with each nearest neighbor to form the covalence bond with a bond angle of 109.47°. The lattice constant is $5.43\mathring{A}$. Figure 5.1 shows the conventional cubic cell of silicon lattice.

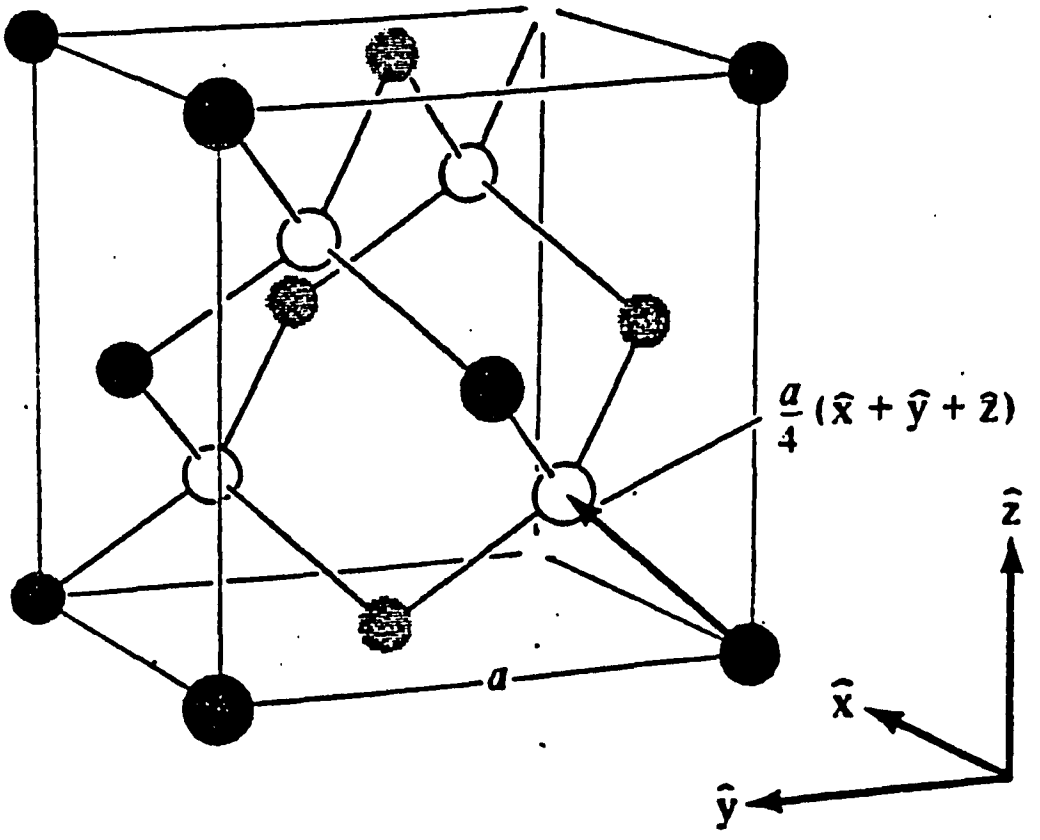

Figure 5.1: The conventional cubic cell of Si lattice–two interpenetrating FCC lattices

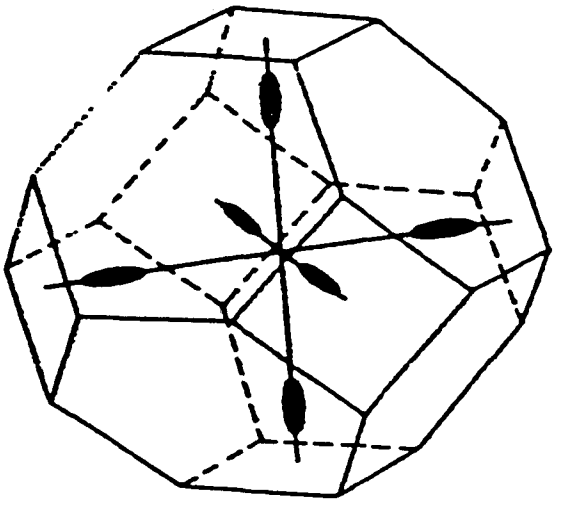

Figure 5.2: Constant-energy surfaces near the conduction band minima in silicon.

5.1.1 The Energy Bands of Si Single Crystal

The reciprocal lattice is a BCC Bravais lattice. The first Brillioun zone is the truncated octahedron. The conduction band has six symmetry-related minima at points in $< 100 >$ directions, about 80% of the way to the zone boundary (see figure 5.1). As a most studied and understood semiconductor, silicon energy band has been calculated by quite a few workers with various methods, especially Herman[119], Chelikowsky and Cohen's work[120]. Figure 5.2 shows the energy bands of silicon. The conduction band minimum along [100] gives rise to the ellipsoids of figure 5.2. The valence band maximum occurs at $\vec{k}$=0, where two degenerate band with different curvature meet, giving rise to 'light holes' and 'heavy holes'. The most significant difference from the energy bands of GaAs is that the Si has an indirect bandgap. The bandgap of Si single crystal is 1.12 eV at room temperature.

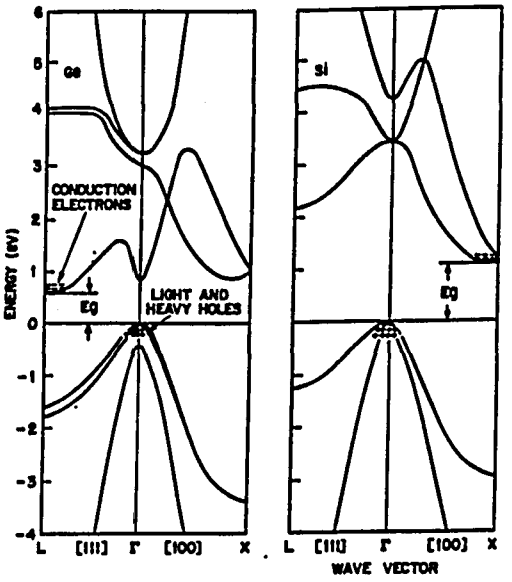

Figure 5.3: The energy band in Silicon, From ref.[120].

5.1.2 The Surface of Si Single Crystal

Unlike the bulk, which can be regarded as an infinite uniform periodic structure amenable to theoretical treatment, semiconductor surface is an abrupt termination of the periodic lattice. This termination results in deformation of the crystal surface and a loss in periodicity. The atoms at the semiconductor surface are not completely surrounded by other atoms of the crystal like those in the bulk. As a result, all the valence electrons of the surface atoms are not satisfied and the unsaturated bonds of the surface atoms make the surface highly reactive chemically. For Si, there is usually one unpaired valence electron, forming a dangling bond. Thus, the surface of a semiconductor usually is covered with one or more layer of foreign atoms. Unfortunately, surface properties can be the dominant influence on device performance and stability. The surface properties are affected significantly by small amount of contamination picked up from the environment during handling, processing, and use.

Historically, the first attempt to solve the problem of the surface sensitivity of semiconductor devices was to encapsulate the bipolar transistors and junction diodes in a hermetically sealed metal can, which was not quite practical. The most practical solution was to passivate the surface. Passivation is accomplished by forming a thin insulating layer on the surface. Passivation minimizes the electrical activity of the device surface and the passivating layer also protects the surface from environmental contamination. Thus, passivation results in a marked improvement of device performance, stability, and uniformity of characteristics from device to device. By far, the most successfully passivated semiconductor is Si, although a lot of effort has been devoted to the surface passivation of other important semiconductors, for example, germanium (Ge)[121] and gallium-arsenide (GaAs)[122, 123]. As the ability to produce a stable insulating layer by oxygen passivation on the surface of a Si crystal was considered as a milestone in the development of Si-based semiconductor technology, it is necessary to give a brief description of the oxide layer.

5.2 SiO_2 Layer on the Si Surface

As stated in previous section, the purpose of growing a layer of silicon-dioxide on the Si surface is to passivate the electrically sensitive surface, *i.e.* to prevent the surface from contamination by impurities. In this section, we will briefly describe methods of growing the oxide layer, the mechanism of protecting the surface by introducing this layer (The general discussion will follow those given by Nicollian and Brews[124]).

5.2.1 Oxidation Technology

Once the silicon crystal for electron device application is pulled into the form of a cylindrical single crystal ingot, the following three steps are required to prepare wafers from the ingot for oxidation:

(1) Saw. Cut the ingot into slices (circular disc) with required thickness and the orientation of the slices is established by having a birotational X-ray goniometer serve as a crystal holder on the sawing apparatus, while a single X-ray diffraction spectrometer and a Laue back reflectance camera are required for determining orientation prior to sawing. A diamond saw is used because silicon is a relatively hard material.

(2) Chemical etching. The sawing operation mechanically damage the surface on each side of the wafer and the damaged surface layers have electrically active properties significantly different from the bulk properties of Si single crystal. Chemical etching of 25 μm of silicon from each side of the wafer removes the electrically active damage completely and neither leaves the wafer nonflat nor causes feather edges prone to chipping. The usual etchant consists of 4 parts by volume of nitric acid, 1 part hydrofluoric acid, and 3 parts acetic acid. The nitric acid oxidizes the silicon surface, and the hydrofluoric acid dissolves the oxide formed.

(3) Polishing. This is the last and most critical step: leaves one surface flat and undamaged. The polishing is done by rubbing the wafer against a cloth saturated with an abrasive material such as Syton–powdered SiO_2 which is not foreign to the SiO_2-Si system.

After the polishing residues have been cleaned off, the wafers are ready for the preoxidation cleaning step which is considered as part of the oxidation process as the wafers should be placed in the oxidation furnace immediately after the preoxidation cleaning. The procedure for preoxidation cleaning was described in detail by the Bell

Telephone Laboratories Manual entitled Silicon Oxidation Guide. The purpose of the preoxidation cleaning is to remove the metallic impurities (in particular, the metal ions from group I and II of the periodic table) from the silicon surface and prevent their displacement plating back onto the silicon.

After the preoxidation cleaning (during which the wafer should not be permitted to dry even partially because even highest purity water or reagent has some submicron-size particles that become deposited on the surface during drying), the oxidation process can be accomplished. The gate oxide (the oxide grown prior to the deposition of the gate electrode in a MOSFET) is grown in dry oxygen at $900 \sim 1200^{o}C$ to a thickness typically 100 nm or less. The field oxide (the oxide used to isolate metallization patterns, carry current to various portions of the iterated circuit from the silicon substrate and to act as a diffusion mask) is grown in steam to a thickness typically 500 nm or more.

5.2.2 'Dry' and 'Wet' oxide

After finishing above preoxidation and cleaning, the silicon surface will be exposed to an oxidizing ambient to grow SiO_2 and the terms 'dry' and 'wet' are used to describe the growth condition of the thermal oxidation process[125] (temperature ranges from 900 to 1200°C). 'Dry' oxide refers to oxidation in pure oxygen and the stoichiometric chemical reaction is

$$Si(solid) + O_2 \rightleftharpoons SiO_2(solid) \tag{5.1}$$

while the stoichiometric chemical reaction for the 'wet' oxide is

$$Si(solid) + 2H_2O \rightleftharpoons SiO_2(solid) + 2H_2 \tag{5.2}$$

The relative degree of hydration distinguishes the 'dry' process from the 'wet' process. Above equations describe only the overall reactions. The different intermediate reactions during the oxidation process and the subsequent dissimilar impurity incorporation coefficients make the detectable differences between 'dry' and 'wet' oxide.

It is a widespread practice in growing 'dry' oxide that chlorine is intentionally added to the oxidation ambient to minimize sodium ion concentration, to reduce the interface trap density (will be discussed later), and to increase the dielectric breakdown strength. Chlorine is added to the oxidation ambient in either chlorine gas, HCl, or chlorine incorporated organic compounds. However, the chlorination only works in 'dry' oxide but not in 'wet' oxide[124] and too much chlorine would form bubbles[126] at the SiO_2-Si interface.

There are various methods of measuring the thickness of the oxide layer, for example, ellipsometry[127], multiple-beam interferometry[128], capacitance method and optical interference method, just name the few. A relatively detailed description of the measuring techniques can be found in ref [124].

5.2.3 Planar Process

It is inevitable to mention the discovery of planar process in reviewing the history of silicon technology. It is almost as same important as the discovery of the oxide passivation. In 1957, Frosh and Derrick[129] found that the thin layer of silicon dioxide can effectively mask against many commonly used dopant impurities, thus preventing them from reaching the underlying silicon. The importance of the discovery is that this made possible precise control of both the depth of a diffused (later on, ion-implanted) junction and its location on the silicon wafer. The location of devices on the silicon wafer could be delineated by covering the silicon with SiO_2 and

then exposing the silicon to the diffusing impurities only in selected area, defined by photolithography, where the SiO_2 layer had been removed. The idea of selectively removing SiO_2 and introducing dopant impurities to the areas of bare silicon was first produced by Hoeni[130] and was called planar process (or technology). The planar process was so successful in fabricating the integrated circuit that all monolithic circuit are made by the planar process today.

5.3 SiO_2-Si Interface

We have described the Si single crystal and the masking SiO_2 in previous sections. Now we have to move our attention to the transition region (if any) between the two solids, the so-called interface region, which joins the two solids with different structures. There had been a long argument about the existence of the interface region. Now it is commonly accepted that there is a interface region with a thickness of $10 \sim 40\mathring{A}$, connecting the Si single crystal and the amorphous SiO_2.

5.3.1 Interfacial Model

Modeling of the entire SiO_2-Si interfacial region is essential for a better understanding of this interface. Such understanding would be of technological importance if it led to better control of the properties of the interface, based on science rather than on empirical art. An appealing picture of the SiO_2-Si interface proposed by Grunthaner and Maserjian et *al*[132, 133, 134, 135] is one of an interfacial region comprised of single crystal silicon followed by

(1) a monolayer in which there are some SiO_2, Si_2O_2, and Si_2O (i.e., incompletely oxidized silicon and the relative amounts of these suboxides depend on processing),

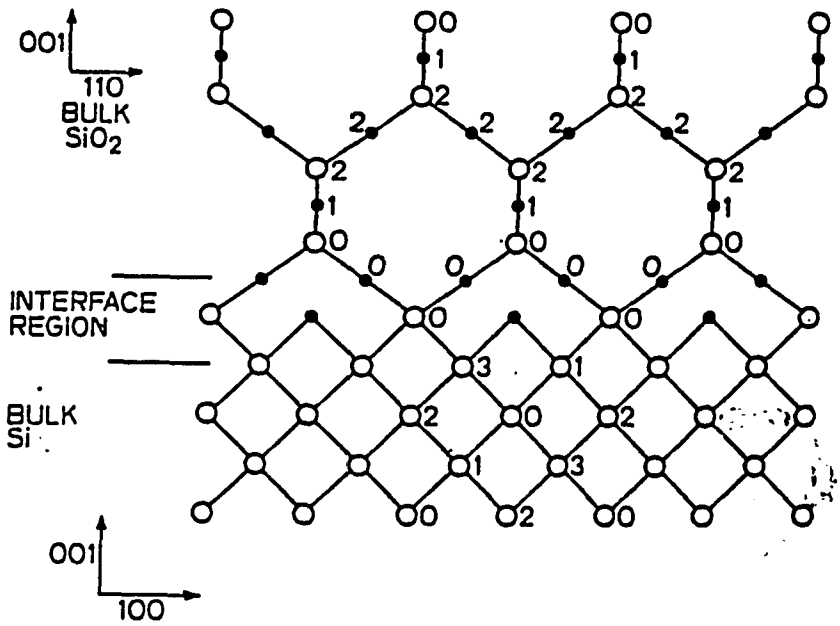

Figure 5.4: The crystalline model of the Si-SiO_2 interface showing the match between Si(001) and cristobalite (011) (After Herman *et al*[136]).

(2) a strained region of SiO_2 roughly 10-40 $\AA$ deep.

(3) the remaining stoichiometric, strain free, amorphous SiO_2.

While Herman *et al*[136] constructed an ideal SiO_2-Si structure with a nearly perfect geometrical match between SiO_2 and Si(100). Figure 5.4 shows the atomic configuration of this model. This model gave the narrowest interface ($2 \sim 3\AA$) contains an intermediate SiO configuration to connect Si and SiO_2. Even in this ideal model, the intrinsic imperfections still exist at the interface region because there is interface strain due to about 6% mismatch between the Si atom positions in Si single crystal and SiO_2 due to a lower Si atom concentration in SiO_2 ($\sim 2.5 \times 10^{22}/cm^3$) compared to that in Si ($\sim 5 \times 10^{22}/cm^3$). This 6% of mismatch results in broken

bonds and leads to some interface strain. Consequently, these intrinsic imperfections make interface act as a sink for impurities. In fact, this ideal interface structure has never been observed and may well be thermodynamically unstable. However, it does form a good basis for understanding what the actual interface might look like.

5.3.2 Interfacial Traps

The problem of charge trapping at or near a semiconductor surface is very old. The oxide passivation on the surface of silicon was a breakthrough on the process of solving this problem. But the introduction of the layer of oxide moves the charge trapping problem to the interface region. Although a very large research effort on the SiO_2-Si interface system had been motivated since 1960, this problem is still not fully understood or completely under control. Through the work of last three decades, we have learned to minimize most of the charge trapping problems, at least emperically. There exist in principle two classes of trapping states in the SiO_2-Si system. One is the so-called interface traps, which capture and release electrons and holes with a time constant at room temperature in the range of picoseconds to hours, affecting directly the leakage currents, metal-oxide-silicon (MOS) capacitor storage time and noise voltage. The second class of trapping states are the bulk oxide traps with long time constants (years), affecting the device stability. Several kinds of interface traps and charges had been identified and characterized by Capacitor versus Voltage (C-V) measurement on the MOS structures. Figure 5.5 illustrates the three oxide "charges" in interface defined by Deal [137, 138]. They are: fixed oxide charge (of concentration per unit area N_f), interface trapped charge (of concentration N_{it}), and oxide trapped charge (of concentration N_{ot}). Although the three "charges" had been extensively investigated, their physical origin are still unclear [139].

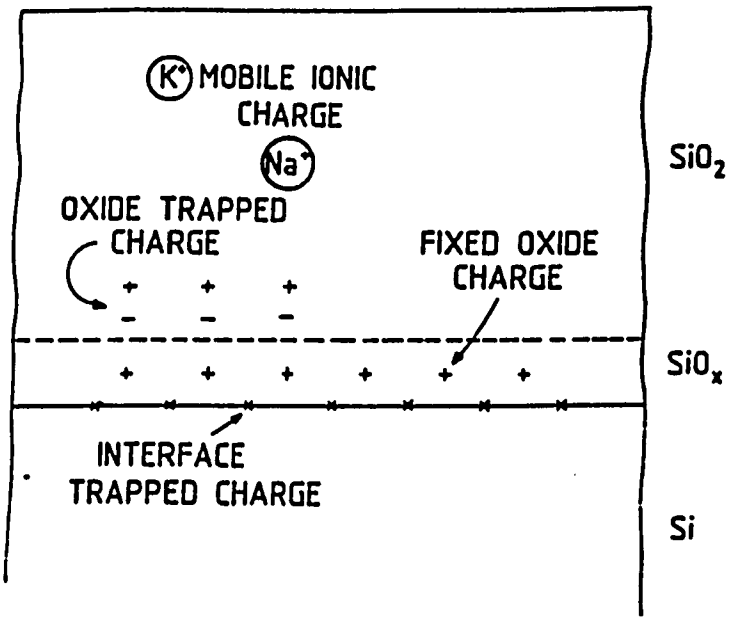

Figure 5.5: The charges in the SiO_2-Si interface. (After Deal[137, 138]).

It is worthwhile to point out that, these "charges", especially the fixed oxide charge will produce an electric field pointing to the bulk Si and these field will affect the diffusion of the thermalized positrons in bulk Si. In the calculation of positron annihilation fraction, this field must be taken into account.

5.3.3 Interfacial Defects

The defects in the interface region still play significant role in determining the quality and performances of Si-related devices[124, 140]. Thus the identification and characterization of interfacial defects has been an active field of research and still remain active as a fully understanding of the defects is still not accomplished yet. EPR is the most powerful tool in the study of the interfacial defects, especially unpaired spin related defects. The silicon dangling bond in the interface was first observed by Poindexter *et al*[116] using EPR in thermally oxidized silicon. They designated the EPR signal as the P_b center which is also observed in damaged silicon and is undoubtedly due to the unpaired spin of a silicon dangling bond but with atom otherwise bonded to other silicon atoms. Figure 5.6 gives two models of the broken bond related defects.

Of all the postulated interface defects, only the P_b centers had been experimentally verified. And it was found that the P_b centers associated to interface states (responding to about half of the interface states). P_b center is identified with a Si atom bonded to three other silicon atoms, with the unbonded electron orbital (the dangling bond) pointing to the oxide, normal to the Si (111) surface. While in Si (100) direction, P_b have two possible configurations: one is the Si atom bonded to three other silicon atoms (Si$\equiv Si_3$, denoted as P_{b0}) with the dangling bond pointing to oxide at 60 degree angle relative to the (100) surface and the other is a Si atom

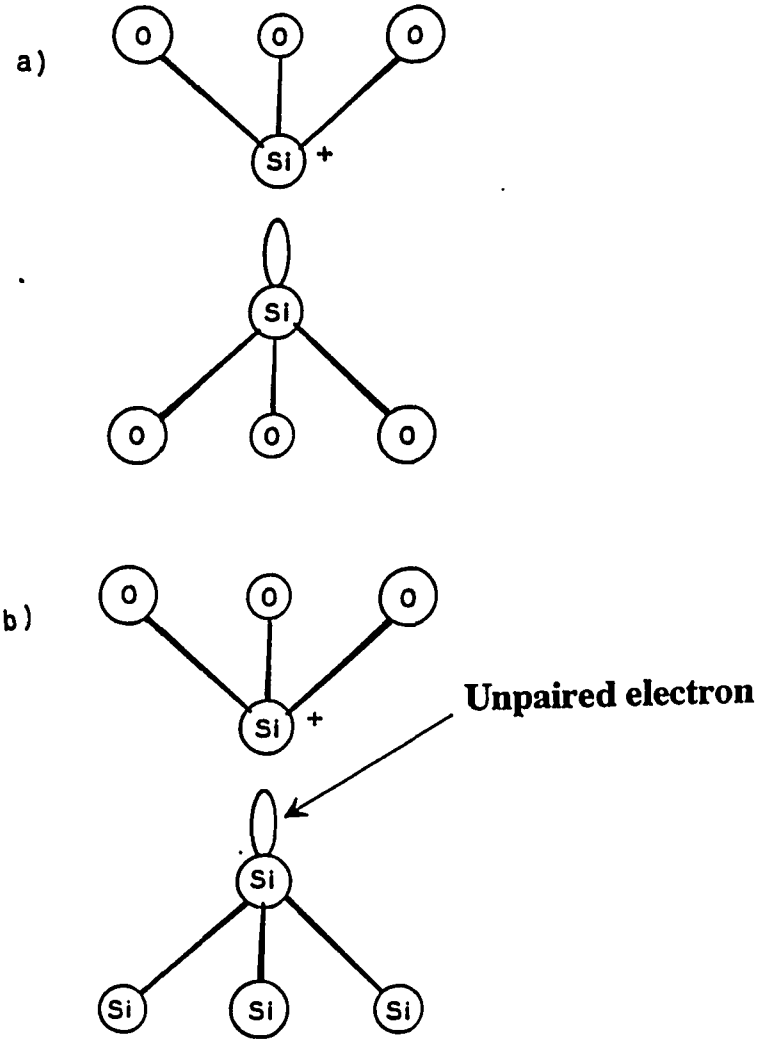

Figure 5.6: The model of the broken bond defect (a) Model of the broken bond defect believed associated with the E' center in bulk SiO_2. (b) Related defect at the SiO_2-Si interface which appear as a P_b center in EPR spectra.

bonded to two other silicon atoms and an oxygen atom (Si≡ Si_2O, denoted as P_{b1}) with the dangling bond pointing to oxide with 60 degree angle. Up to present, only the P_{b0} center was experimentally observed, due to the difficulty in separating the EPR signals from the two centers. It is possible to use positron 2D-ACAR to separate the two centers by employing (111) and (100) samples and comparing the two spectrum.

5.4 Positron 2D-ACAR Study of the SiO_2-Si System

In this section, we present the result on the study of SiO_2-Si system by positron 2D-ACAR coupled with a high-intensity monoenergetic slow positron beam, described in section 3.2. This is the theme of the thesis.

5.4.1 The SiO_2-Si Sample

The samples investigated were Czokralski grown Si(100) single crystal with a layer of oxide on its surface, thermally grown in dry oxygen ambient at the temperature range of 900~1000°C, no HCl, no forming gas (FG) annealing. The thickness of the oxide was $\sim$ 1170$\AA$, measured by the ellipsometry method. The samples were supplied by IBM Inc.. The density of the interfacial state is $\sim 10^9/(cm^2 \cdot eV)$, measured by C-V method[124]. Figure 5.7 shows the configuration of the sample. In the measurement, the sample was aligned such that the integration direction, p_z, along the $< 01\bar{1} >$ crystallographic direction, and in the 2D-ACAR spectrum, $p_x \rightarrow < 100 >$ and $p_y \rightarrow < 011 >$ crystallographic directions, respectively.

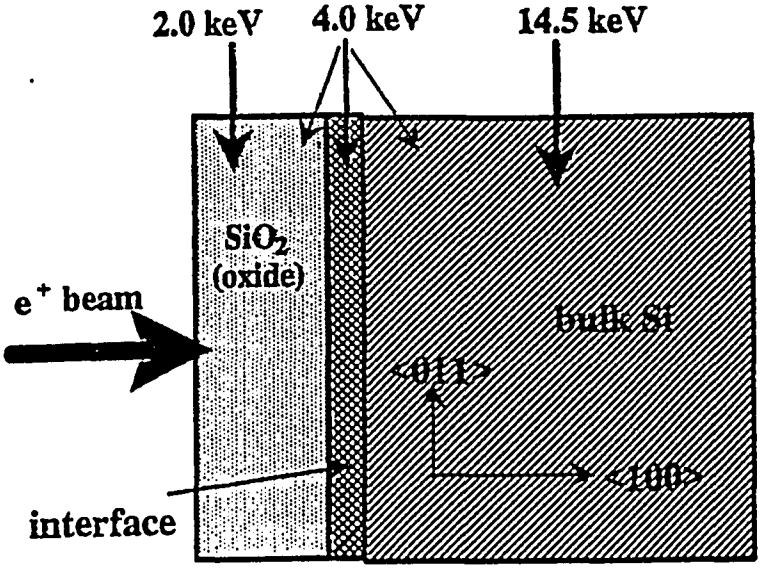

(a)

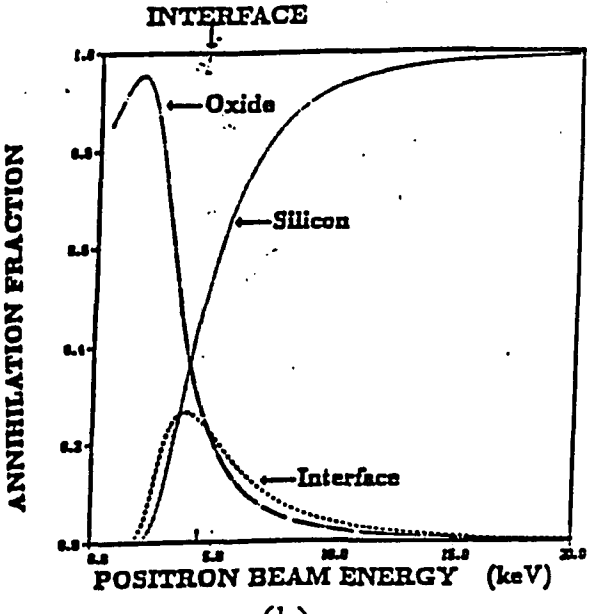

(b)

Figure 5.7: (a) The configuration of the sample. (b) The illustration of positron annihilation fraction at different beam energies (for a different sample).

5.4.2 Overture–Doppler Broadening Measurement

By changing the positron beam energy, the positrons can be implanted into different layers of the SiO_2-Si system. The implantation profile (which is a Makhovian) and the diffusion of the thermalized positrons (in Si single crystal the diffusion length is $1000 \sim 2000\mathring{A}$, while in amorphous SiO_2, the diffusion length is under $100\mathring{A}$.) cause a relatively large spatial spread (relative to the thickness of the layers) of the annihilating positrons. Thus, even with a single energy of the incident positrons and an known mean implantation depth, the annihilation may still extend to a few neighboring layers. For each incident energy of the positron beam, we have to figure out the annihilation fraction of the incident positrons at different regions (or layers). For a specified beam energy of the incident positrons, the resultant 2D-ACAR spectrum $N(p_x, p_y)$ is a linear combination of the spectra of positron annihilation at different layers:

$$N(p_x,p_y) = f_{surf}N_{surf}(p_x,p_y)+f_{oxide}N_{oxide}(p_x,p_y)+f_{intf}N_{intf}(p_x,p_y)+f_{bulk}N_{bulk}(p_x,p_y) \tag{5.3}$$

where N_{surf}, N_{oxide}, N_{intf}, and N_{bulk} are the positron 2D-ACAR spectrum at surface, oxide region, interface region, and bulk Si single crystal, respectively. The f's are the annihilation fractions corresponding to each region mentioned above with the normalization condition of $f_{surf} + f_{oxide} + f_{intf} + f_{bulk} = 1.0$. The f's can be obtained by different measurement based on positron annihilation:

(1) Positron lifetime measurement by fitting the lifetime curve with known average lifetime in each region.

(2) Positron Doppler Broadening (or S-parameter) measurement by fitting the S-E curve employing the standard numeric procedure VEPFIT described in section 4.3.

(3) Use formula 5.3 to do the least χ^2 fit to the resultant 2D-ACAR spectrum if

each individual spectrum on the righthand of the formula is known.

Unfortunately, the positron beam lifetime measurement is far more difficult than the conventional lifetime measurement and our beamline is incapable of doing the lifetime measurement because of the relatively large spread in the positron energy. Positron 2D-ACAR spectrum is unavailable for positron annihilating at each individual layer (or region). Therefore, the only solution is to do the positron S-parameter (Doppler broadening) measurement. In fact, positron S-parameter measurement had been extensively used to study the important SiO_2-Si system[114, 147, 96, 51]. There was a clear interface signal in the measured S-E curve. Although a lot of experiments had been done and a lot of data showing the overall feature of the system had been accumulated, the detailed structure or feature regarding to positron annihilation in this system was still unclear due to the limitation of the resolution and sensitivity of the measuring parameter. The development of the high-intensity monoenergetic slow positron beam made it possible for the first time in the world to obtain the information in the atomic scale from this system by 2D-ACAR method.

Before the detailed positron 2D-ACAR experiment was carried out, the positron S-parameter measurement had been performed on the samples which were going to be studied by 2D-ACAR measurement to obtain the information regarding positron annihilation fraction. The experiment was done in a separate laboratory positron beam which has lower intensity ($\sim 5 \times 10^5 e^+/sec.$) and with which a routine S-parameter measurement can be carried out much easier and only need 6 to 8 hours of data acquisition time for each sample. The detailed description about this beamline can be found elsewhere[92]. Figure 5.8 shows the result (S-E curve) from S-parameter measurement (in which the data for the p-type sample was quoted from ref[147]).

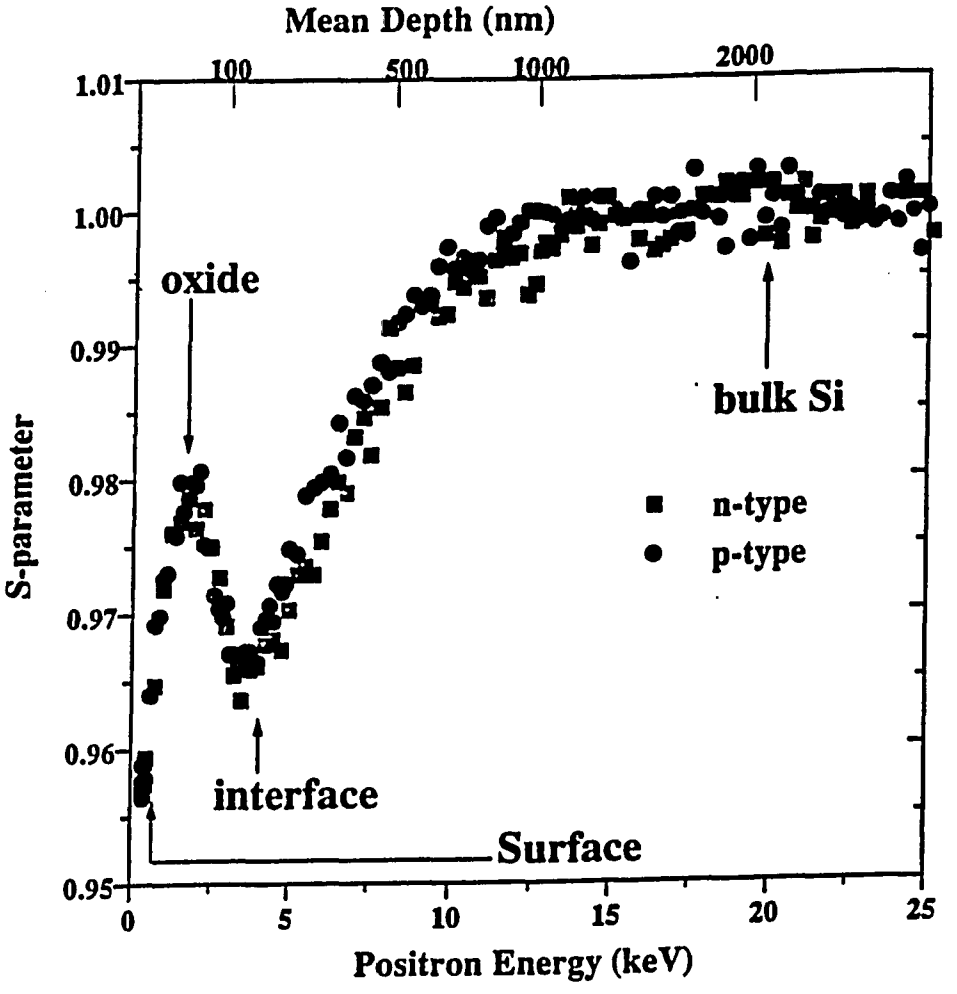

Figure 5.8: The S-parameter *vs* positron beam energy curve from positron Doppler broadening measurement. A clear interface signal appears at beam energy of 4-5 keV. The data for the p-type sample was quoted from ref[147]

5.4.3 Positron 2D-ACAR Spectrum at Positron Beam Energy of 2.0 keV

The sample chamber on the high-intensity positron beamline is not designed for surface measurement to get a 2D-ACAR spectrum for a clean surface. Thus, we have to choose appropriate beam energy to avoid the surface. Because the thickness of oxide layer is large enough to get a relatively pure oxide spectrum by carefully choosing the positron beam energy by which both surface and interface contribution can be minimized. From S-parameter measurement, it was calculated that at beam energy of 2 keV, the surface fraction, f_{surf}, is less than 4% (and would become smaller with increasing the beam energy as expected) and the interface fraction, f_{intf}, is about 6%. Thus 90% of the annihilation occurred in oxide layer. So the spectrum taken at 2 keV gave a fairly good oxide spectrum which could be used as a basis in the following data analysis. Figure 5.9 gives the 2D-ACAR spectrum for the n-type sample at beam energy of 2 keV. From this spectrum, we may not be able to get much information about the status of positron annihilation in oxide because the mixture of contributions from different annihilation channels. After the subtraction of the broad symmetric component (see the discussion given in sect.4.2) originating from positron annihilation with valence and core electrons of both Si atoms and O atoms, the detailed structures appear clearly. The residual spectrum is usually called fine structure spectrum. Figure 5.10 shows the fine structure. From fig. 5.10 we can see that there is a sharp peak in the center of the spectrum, indicative of Positronium atom (Ps) formation in the oxide region (similar to the case of Ps formation in quartz single crystal in which the Ps are delocalized and the 2D-ACAR spectrum shows the periodicity of the crystal, see fig 3.9). Comparing with the Ps peaks in the 2D-ACAR spectrum for quartz single crystal shown in fig. 3.9, there is only one sharp peak in

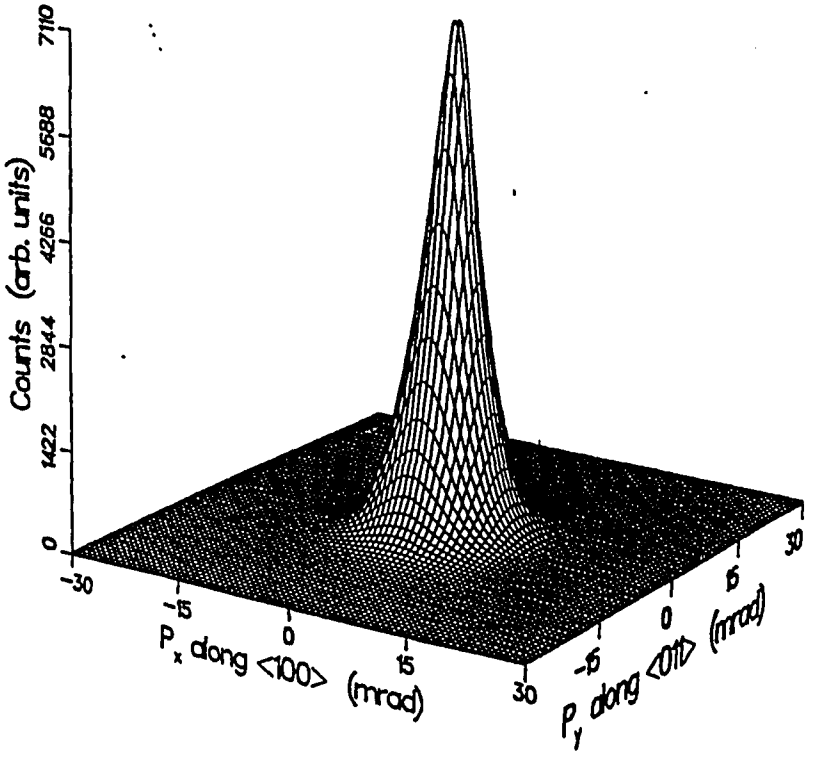

Figure 5.9: Positron 2D-ACAR spectrum at beam energy of 2 keV for the n-type sample.

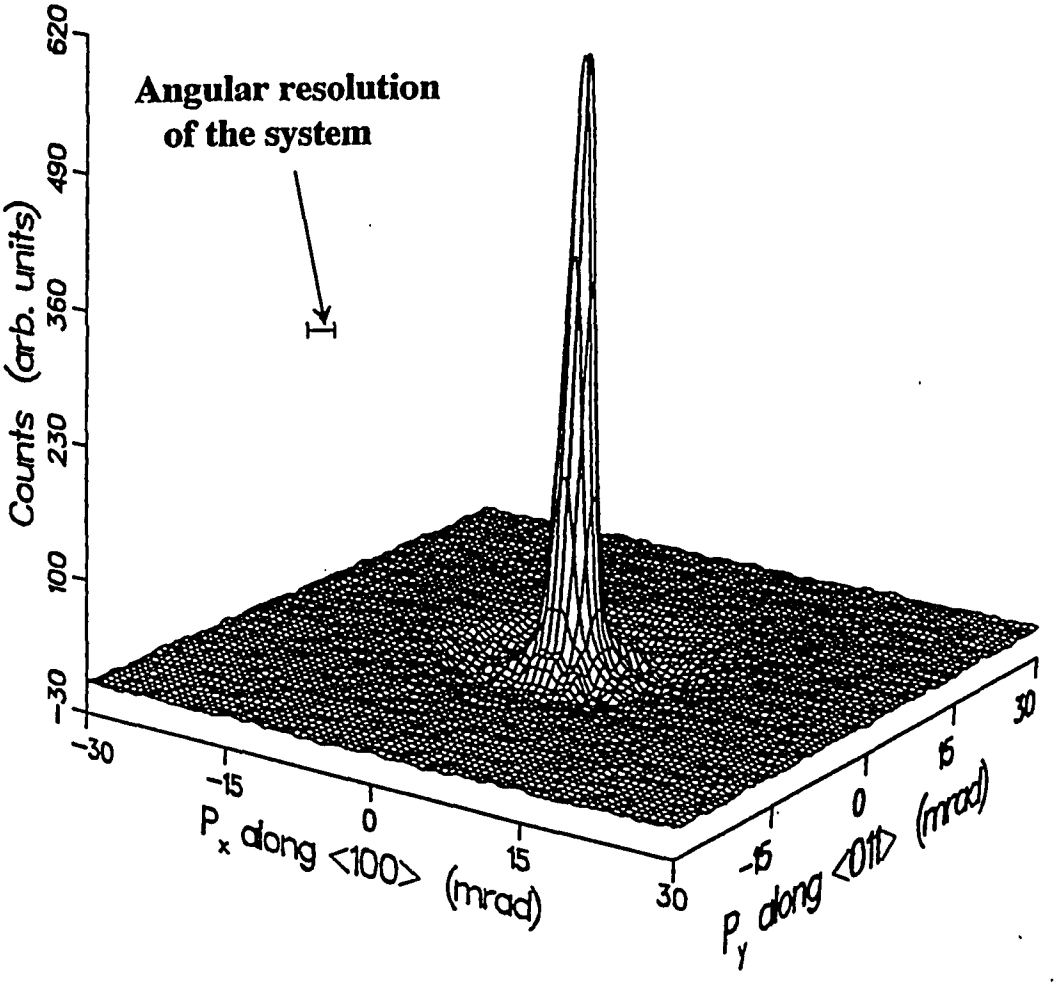

Figure 5.10: The fine structure of positron annihilation at beam energy of 2.0 keV.

the fine structure spectrum of oxide, indicating that the Ps formed in oxide must be localized, in other words, the Ps atoms are trapped into microvoids (here we don't have solid argument whether the positron get trapped into the microvoid first and then form the Ps or vise versa). It is not a surprising result because Ps formation and trapping in amorphous SiO_2 had been observed before[172, 173].

Beside the central sharp Ps peak, there are some small bumps surrounding the Ps peak, with a four-fold symmetry. From the position of the small bump, it may come from positron annihilation in vacancy-like defects. Lack of any anisotropy may indicate that either the defects have a four-fold symmetry or the defects are not aligned along the growth direction. More information is necessary to identify and characterize the defects (may have to get help from other techniques).

5.4.4 2D-ACAR Spectrum for Bulk Si

As the positron beam energy was tuned as high as 14.5 keV, the mean implantation depth, $\bar{z} \approx 12000\mathring{A}$, the positrons will basically penetrate into deep inside bulk silicon single crystal with a small possibility that the thermalized positrons diffuse back to the interface. It was calculated from the S-parameter measurement and using the VEPFIT that over 97% of the incident positrons annihilating in bulk silicon and less than 3% of them diffuse back to interface. Therefore, the spectrum taken at 14.5 keV is a good 2D-ACAR spectrum of silicon single crystal. Figure 5.11 shows the 2D-ACAR spectrum at beam energy of 14.5 keV. The spectrum and its contour plot is similar to other worker's result [174, 175] from the conventional 2D-ACAR (similar to our experiment in semi-insulating GaAs described in chapter 6) measurements. Also, a spectrum of bulk Si (After the oxide layer was etched out by using HF solvent) with the sample cut from the same wafer was taken using the bulk chamber (the

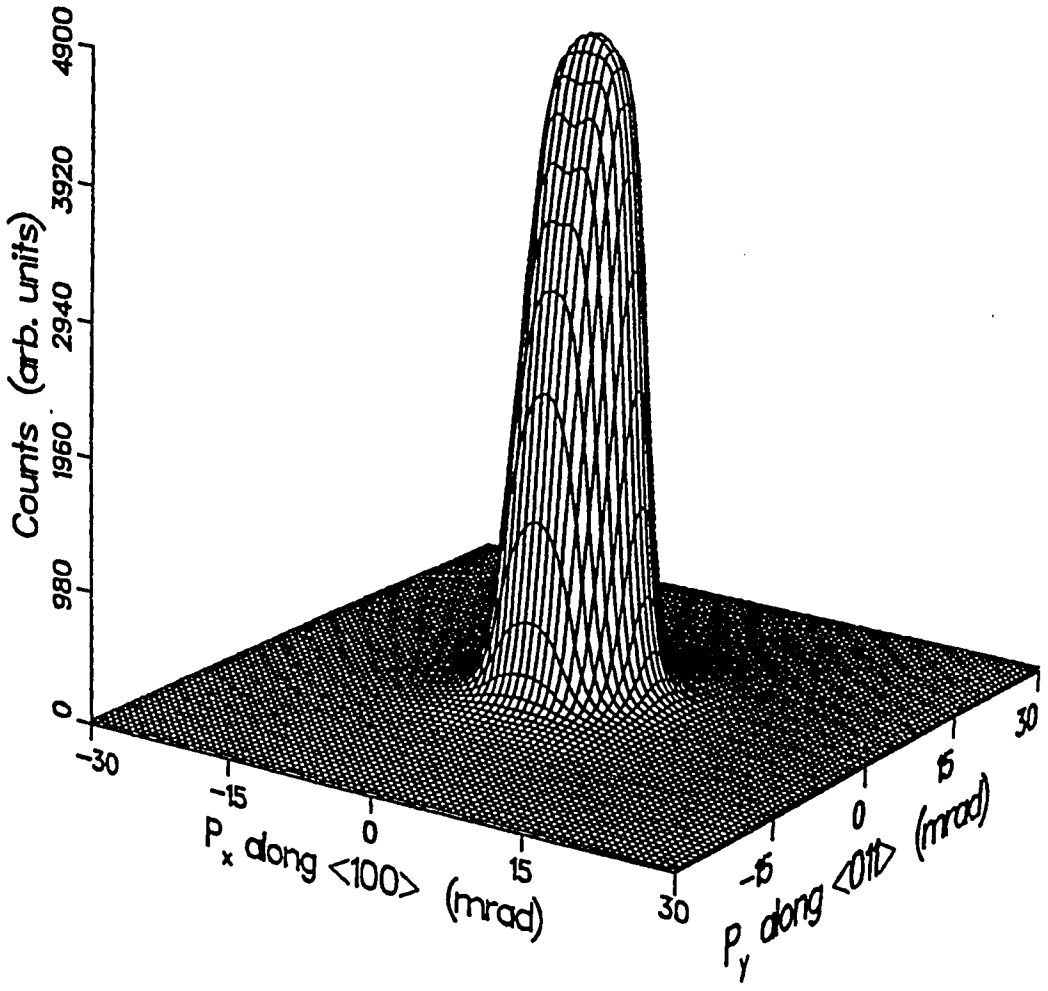

Figure 5.11: 2D-ACAR spectrum at beam energy of 14.5 keV– sampling bulk silicon.

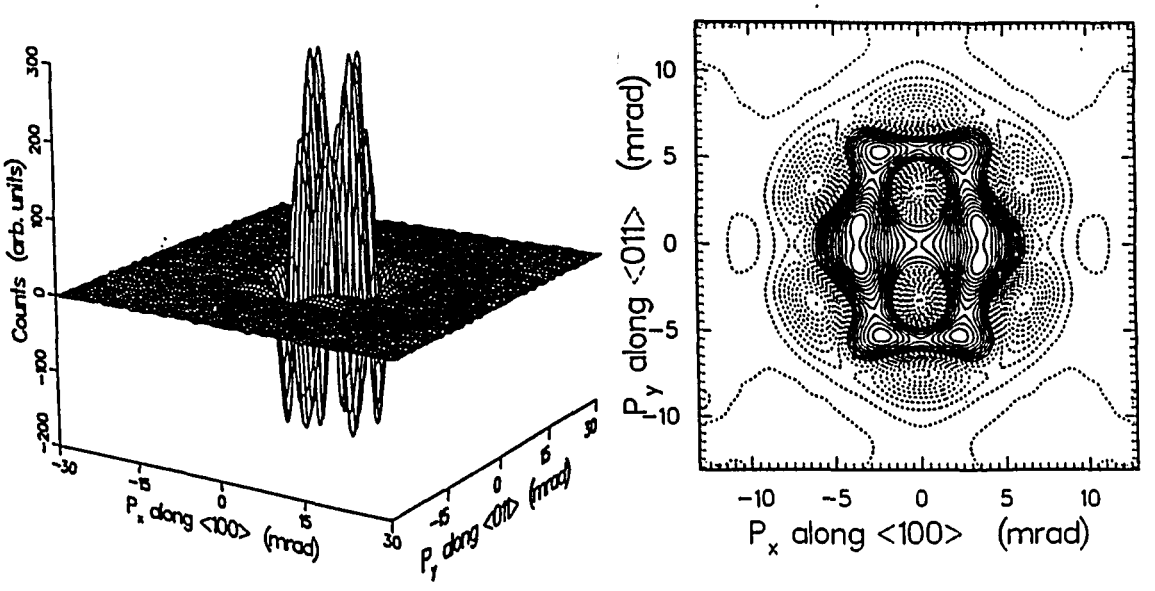

Figure 5.12: Anisotropy (or fine structure) of bulk Si single crystal and its contour plot (measured from bulk chamber).

Anger cameras were moved to 8 meters distance from the bulk chamber to match the setup for the interface measurement). There is $4 \sim 5\%$ difference between the two original spectrum (by volume normalization), which may be due to the difference in the beam size. After the subtraction of the broad symmetric component originating from positron annihilation with valence and core electrons, more features regarding positron annihilation status in bulk Si single crystal are revealed. Figure 5.12 shows the anisotropy of bulk Si single crystal (after the subtraction of the broad component described in section 4.2) and its contour plot from the bulk chamber measurement (the anisotropy spectrum measured from the interface chamber is very similar to this spectrum). Figure 5.13 gives the comparison of the anisotropy of Si measured in our

experiment with that from other work's result. Here we use one-dimensional plot along two major axis (< 100 > and < 011 >). The error bar is representative in all of our data shown in this thesis (the error bar is difficult to show in 3D-plots). Comparing with the anisotropy for GaAs (see figure 6.9), the two semiconductors show very similar anisotropy, originating from the same FCC lattice and similar band structures.

5.4.5 Spectrum at Beam Energy of 4 keV– Sampling the Interface Region

It is very important to choose a right positron beam energy to probe the SiO_2-Si interface, because we want maximum interface fraction in the spectrum at that beam energy. As stated above that the width (linear dimension) of the interface region is only 10-40 $\AA$, only a very small fraction of incident positrons really stop at interface, while those positrons which were implanted to bulk Si originally may have a good chance of diffusing back to the interface after thermalization if the mean implantation depth is not too far away from the interface (within the positron diffusion length in Si single crystal: 1000–2000$\AA$). Thus, the fraction of positron annihilation at interface is largely dependent on the positron diffusion instead of direct implantation. From the result of positron S-parameter measurement, it was found that the interface annihilation reach its maximum at beam energy of 4 keV. Thus, 4 keV acceleration energy was chosen to probe the interface. Figure 5.14 shows the 2D-ACAR spectrum at positron beam energy of 4 keV at which the mean implantation depth is $\sim$ 1500$\AA$ (about 400 $\AA$ away from the interface). As mention above, this spectrum is a mixture of positron annihilation at oxide, interface, and bulk Si single crystal. To get the feature of positron annihilation in the interface, the fractions of positron annihilation

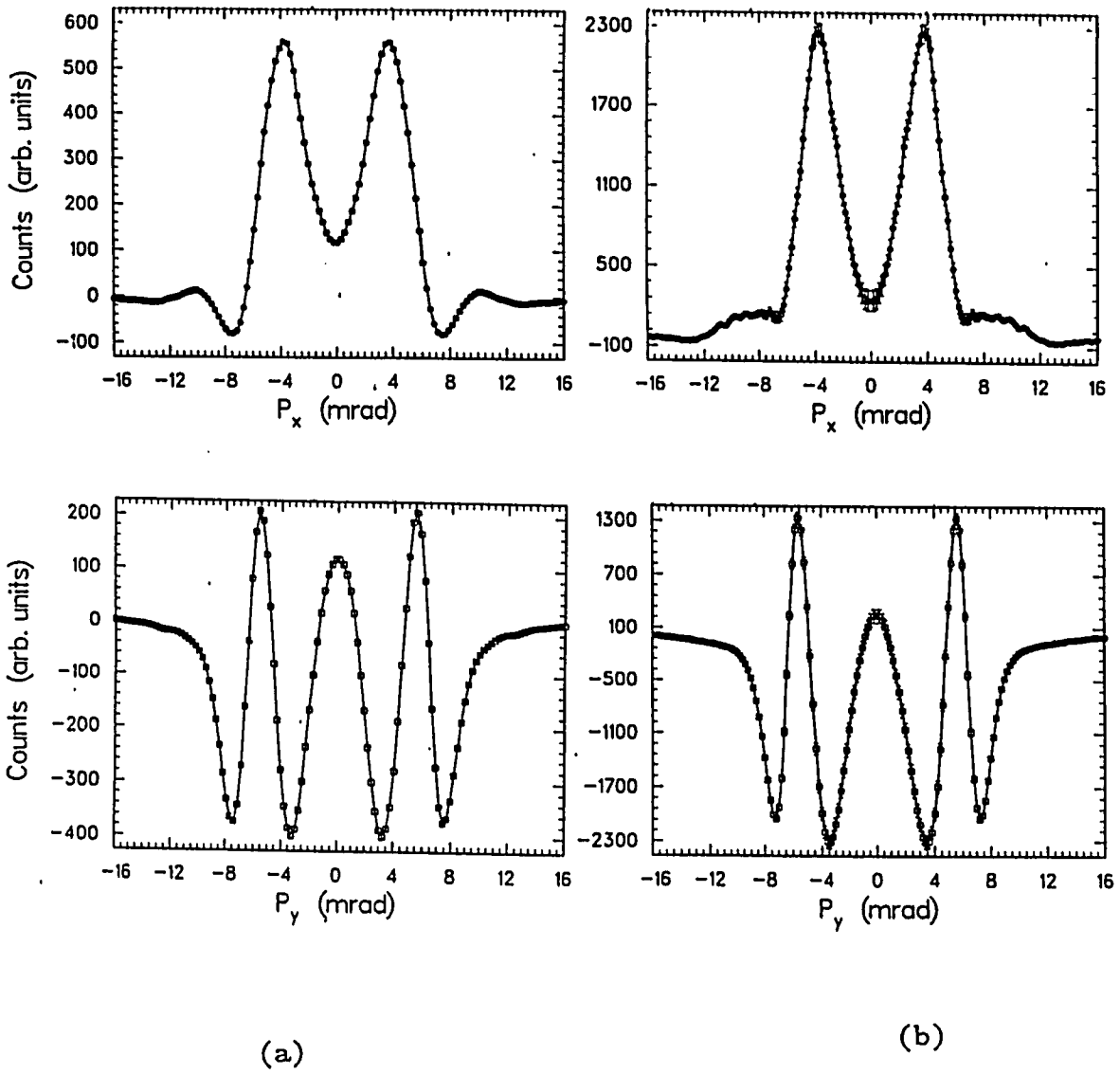

Figure 5.13: (a) The 1D-plot of the anisotropy of Si for our data. (b)Similar plot for the data from ref.[175]. (by conventional 2D-ACAR setup)

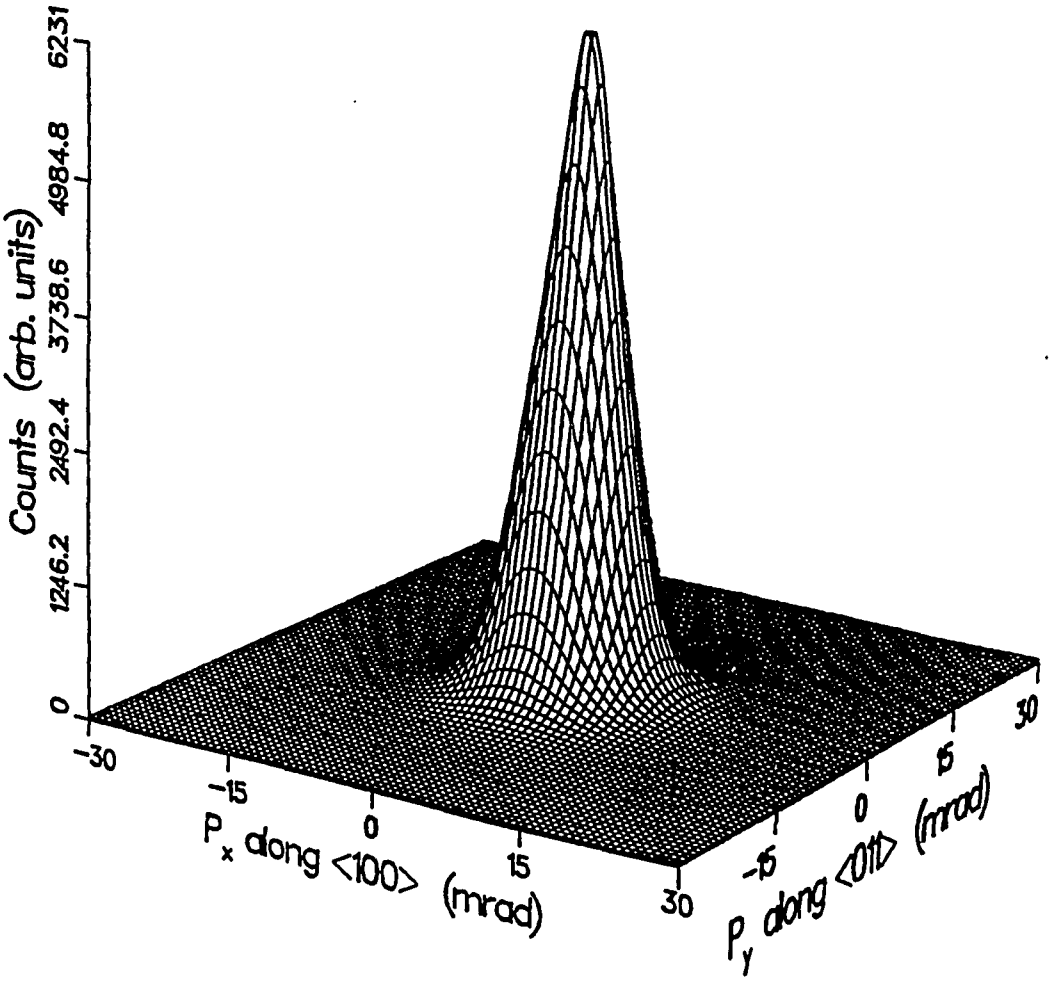

Figure 5.14: 2D-ACAR spectrum at 4 keV for the n-type sample– 43% of positrons would sample the interface.

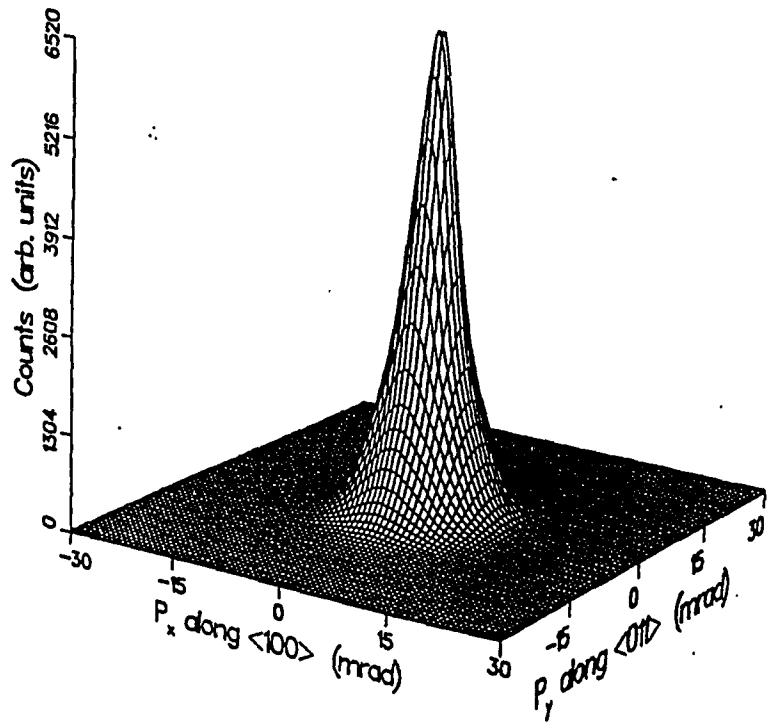

Figure 5.15: Pure interface spectrum– the residual spectrum after the subtraction of the fractions of oxide and bulk Si from the spectrum at beam energy of 4 keV.

in oxide and bulk Si should be subtracted from this spectrum. It was calculated from the S-parameter data that at positron energy of 4.0 keV, f_{oxide}=28%, f_{intf}=43%, and f_{bulk}=29%, while $f_{surf} \approx 0$. Figure 5.15 shows the residual spectrum after the subtraction of the fractions of oxide and bulk Si spectra (see figure 5.9 and fig. 5.12) from the spectrum at 4 keV (fig. 5.14). This spectrum was defined as pure interface spectrum. Here, we use both of the bulk spectra taken in the interface chamber and in the bulk chamber. The pure interface spectra from both subtractions are similar. In the following discussion, we always use the bulk spectrum taken in the bulk chamber. While figure 5.16 shows the fine structure of the pure interface spectrum--after the subtraction of the broad symmetric component. Once again, a sharp peak appears in

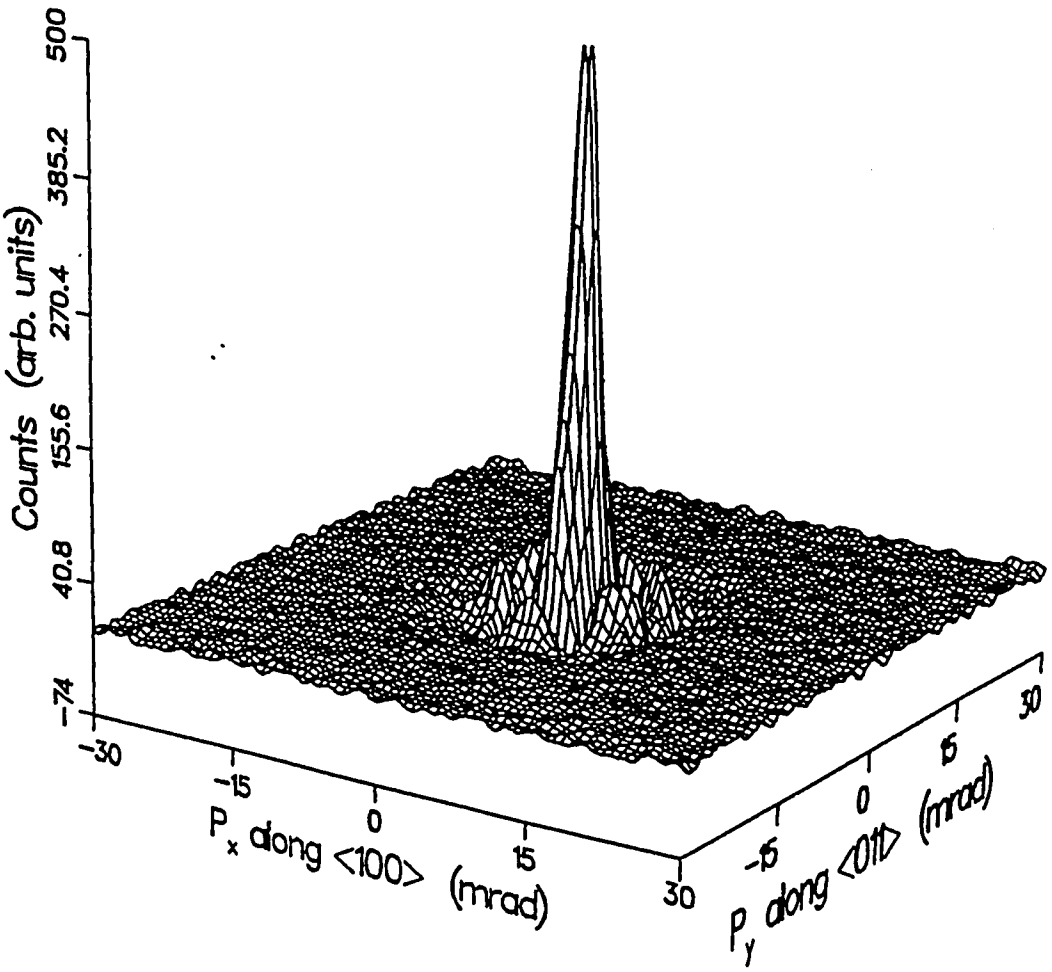

Figure 5.16: The fine structure of the pure interface spectrum

the center of the spectrum, indicating the Ps atoms formation in the interface region. There may be some controversy about this conclusion. First argument is that the Ps peak seen in the interface may just be those Ps atoms which formed in the oxide and diffuse (or drift) to the interface. Second argument is that the Ps signal may be caused by an uncompleted subtraction of the oxide spectrum from the spectrum at 4.0 keV beam energy (the fraction of 28% is doubtful). Following are the verification for confirming our conclusion that the Ps atom signal seen in the pure interface spectrum really represents the Ps atom formation in the interface region.

1) The Ps atoms formed in oxide region can not diffuse or drift to interface. As seen from the fine structure spectrum (fig 5.10) for oxide region, there is only one sharp Ps peak and no any other visible peak around it. It means that the Ps atoms formed in the oxide are trapped into microvoids and the potential barrier of the voids is high enough to confine the Ps atoms trapped. In other words, the Ps atoms in oxide region are localized. In contradiction, the Ps atoms formed in quartz single crystal–crystallized SiO_2, can move freely–they are delocalized and the resultant 2D-ACAR spectrum shows a great central peak and a few small peak around it, reflecting the periodicity of the lattice.

2) The positron annihilation fractions were calculated from the S-parameter measurement using the standard procedure VEPFIT. Unfortunately, the program VEPFIT does not give the error bar. For the sake of safety, it has been tested that the overall shape of the fine structure of pure interface spectrum was stable by a 5% variation of the fractions, e.g. oxide fraction, f_{oxide}, ranged from 25% to 33 %, and bulk Si fraction, f_{bulk}, ranged from 24% to 34%. Further, an χ^2 fitting of the spectrum at 4.0 keV energy by a linear combination of oxide spectrum and bulk Si spectrum (assume there is no interface signal at all) had been performed. Even at the best fit

(with the smallest χ^2), there is still a significant difference between the spectrum at 4.0 keV and the linear combination of the oxide and bulk Si spectra, primarily due to the different widths of the Ps peak in the interface region and in the oxide region. Therefore, there must be an interface signal in the spectrum at beam energy of 4.0 keV.

Thus, the Ps atom signal seen in the pure interface spectrum (the fine structure) is due to the Ps atoms formed in the interface region locally, and can not be accountable for the Ps atoms formed in the oxide region.

Similarly, there is only one sharp peak in the fine structure for the interface, and the width of the peak is much larger than the Ps peak in the spectrum for quartz single crystal, indicating that the Ps atoms formed in the interface region are trapped into the microvoids in that region, i.e. they are not free Ps atoms. Besides the central Ps peak in the fine structure spectrum, there are some small but significant bumps around the central peak, with a 2-fold symmetry. From the position of these small bumps, it can be attributed to positron annihilation in vacancy-like defects. As we mentioned in section 5.2, an important interface defect is the P_b centers which corresponds to about half of the interface states. The unpaired electron of the Si atom, the so called silicon dangling bond or the P_b center and its environment atoms work like a neutral or negatively charged vacancy into which the positrons may get trapped. In the $< 100 >$ crystallographic direction, these dangling bonds point to the oxide direction with a 60 degree angle relative to the (100) silicon surface. Thus, the wavefunction of the dangling bonds will have only 2-fold symmetry. Therefore, we attribute the signal from positron annihilation with vacancy-like defects to positron annihilation with the dangling bonds of the Si atoms in the interface region–P_b centers. In fact, positron trapping and annihilation with or near the P_b centers had been observed in

the positron Doppler broadening (S-parameter) measurement[147, 51] coupled with annealing and hydrogen passivation of the interface states. But the authors attribute the observed features to positron annihilation with valence electrons of the oxygen atoms surrounding the P_b centers, although the conclusion was not quite solid due to the poor energy resolution of the technique and lack of sufficient information regarding the status of positron annihilation in the interface. If their statement was valid, then we should be able to observe the similar small structure in the oxide spectrum (for 2D-ACAR) because the wavefunction of the valence electrons of oxygen atoms should be the same in the interface and oxide regions, which is not the case in the 2D-ACAR measurement.

5.5 Quantative Discussion-The Size and Concentration of the Defects

In last section, the 2D-ACAR result on the SiO_2-Si system has been described in detail but in qualitative manner. In this section, some quantitative results about the defects will be given. These include: apply appropriate analytical method to derive the concentration of the defects in both oxide and interface regions and further derive the dimension of the defects by applying proper model.

5.5.1 The Width of the Ps Signal–Three-Gaussian Fit

In the ideal case (very good system resolution), the Ps signal observed in the oxide and pure interface spectra should be seen clearly without taking out the broad component, like the spectrum for quartz single crystal (here delocalization of the Ps atoms is another important factor of the clearness despite of the system resolution was not

good). But in this experiment, the angular resolution of the measuring system is not too good due to the compromise between the resolution and the count rate (data acquisition time), which can be improved by increasing the distance between the detector and the sample and a resultant lower count rate, and the Ps atoms are localized. Following is the elaboration of the reason why the localization of the Ps atoms will widen the Ps signal in the spectrum.

As described in section 2.1, positron 2D-ACAR measures the momentum distribution of the annihilating $e^+ - e^-$ pair. Ps atom is just a special case of the $e^+ - e^-$ pair-its bound state. When Ps atom is in the delocalized state, it will stay at the bottom of the conduction band (similar to the positron) with a momentum, $\vec{p} \approx \vec{0}, \vec{G}, 2\vec{G} \ldots$, where $\vec{G}$ is the reciprocal lattice vector. That is why we can see an array of Ps atom signals in the spectrum of quartz single crystal and the geometry of the array reflects the periodicity of the crystal. If the Ps atoms are trapped into microvoids (in their localized states), they do not experience the periodic potential and their wavefunctions will not obey the Bloch's theorem[64]. The wavefunction of the localized Ps atom will be determined by the simple Schrödinger equation with an appropriate barrier potential, similar to the motion of a particle confined in a well potential. The width of the Ps signal will be determined by the momentum uncertainty of the Ps atom, $\sqrt{< \vec{p}^2 >}$ which is determined by the size or dimension of the well in which the Ps atom is trapped. Thus, in our data analysis, a spherical well potential was employed to simulate Ps atom trapping in microvoids. Before applying a model to calculate the dimension of the microvoids, it is essential to know the width of the Ps peak (signal) in the 2D-ACAR spectrum. Here, a three-Gaussian curve was used to fit the oxide spectrum and the pure interface spectrum (not the fine structure

spectra).

$$N = \sum_{i=1}^{3} A_i \exp\left[-\frac{(B_i - 116.5)^2}{\sigma_i^2}\right] \tag{5.4}$$

The three gaussians represent Ps peak (with the smallest σ), contribution of positron annihilation in vacancy-like defects (medium σ) , and the contribution from positron annihilation with valence and core electrons (with the largest σ), respectively. 116.5 is the center of the data matrix (The dimension of the data matrix was reduced from 256X256 to 232X232 to minimize the edge effect of the camera.). The relation between the smallest σ (corresponding to the Ps peak) and the full width at half maximum (FWHM) of the Ps peak in the 2D-ACAR spectrum is:

$$FWHM = 2\sigma\sqrt{\ln 2} \tag{5.5}$$

To take the angular resolution of the system (which is $\sim 1.3 \times 1.3$ mrad^2) into account, the real FWHM, σ_{real}, of the Ps peak should be the quadratic difference between the FWHM from the three Gaussian fit, $\sigma_{gaussian}$ and the angular resolution,

$$\sigma_{real}^2 = \sigma_{gaussian}^2 - 1.3^2 \tag{5.6}$$

After the real FWHM of the Ps peak is obtained, which is equal to the momentum uncertainty of the Ps atoms in the microvoids, the infinite-spherical-well potential is introduced to simulate the Ps atoms trapping at microvoids. The concept of the using spherical-well potential to simulate Ps atoms trapping was first introduced by Roellig *et al*[141, 142] in the study of positron annihilation in helium and then was further developed by Briscoe *et al*[143] in a similar experiment. From this model, a formula relating the real FWHM, σ_{real}, of the Ps peak and the diameter, D, of the microvoids in which the Ps atoms were trapped can be obtained,

$$D = \frac{33.2}{\sigma_{real}} \mathring{A} \tag{5.7}$$

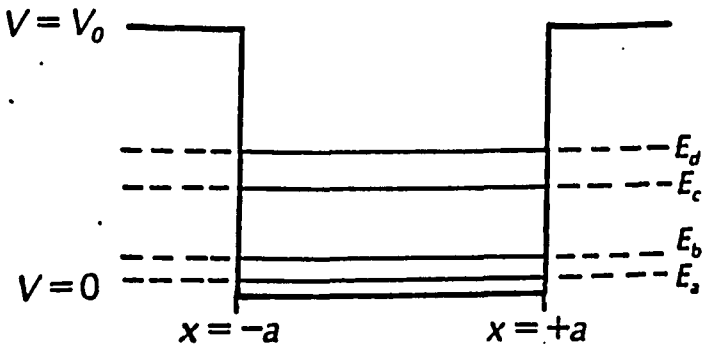

Figure 5.17: Energy levels of a particle confined in a finite-spherical well potential.

where σ_{real} is expressed in mrad.

From the three-gaussian fit for the oxide spectrum, it was calculated that $\sigma_{real} = 3.2 \pm 0.2$ mrad for the Ps peak, corresponding to a microvoids diameter, D_{oxide}, of 10.4 $\pm 0.6 \mathring{A}$. Similarly, in the interface spectrum, $\sigma_{real} = 2.8 \pm 0.2$ mrad, corresponding to a microvoids diameter, D_{intf}, of $11.9 \pm 0.9 \mathring{A}$. There is no difference in the width of the Ps signal between x and y direction, which means that the either the microvoids are not aligned along one direction or with a round shape.

A more realistic model would be a finite-spherical-well potential with a depth of the well V_0 and radius a. Unfortunately, there is no simple relation between the momentum uncertainty, $\sqrt{< \vec{p}^2 >}$, of the particle confined in the well and the radius of the well, a. The energy levels can be obtained by solving the time-independent Schrödinger equation:

$$-\frac{1}{r}\frac{\partial^2}{\partial r^2}(ru) - \frac{1}{r^2 sin\theta}\frac{\partial}{\partial\theta}(sin\theta\frac{\partial u}{\partial\theta}) - \frac{1}{r^2 sin^2\theta}\frac{\partial^2 u}{\partial^2\phi} = \frac{2m}{\hbar^2}[E - V(\vec{r})]u \qquad (5.8)$$

For the centrifugal potential, *i.e.* $V(\vec{r}) = V(r)$, after the separation of the angular

motion from the radical motion, *i.e.*, $u(\vec{r}) = R(r)Y(\theta,\phi)$, the energy levels can be obtained by solving the equation:

$$\frac{d^2}{dr^2}(rR) = -\frac{2m}{\hbar^2}[E - V(r) - \frac{l(l+1)\hbar^2}{2mr^2}](rR) \tag{5.9}$$

By a simple and standard mathematical derivation with an appropriate boundary condition, the energy levels for $l = 0$ states which should be the case of Ps in the microvoids are given by the solution of the equation:

$$sin(ka) = \pm\frac{ka}{\beta a} \tag{5.10}$$

where $k = \sqrt{\frac{2mE}{\hbar^2}}, \beta = \sqrt{\frac{2mV_0}{\hbar^2}}$, and E is the energy of the particle (Ps atom) in the well. The momentum $\vec{p}$ is not an conservative quantity in this situation and its average (expectation) value $< \vec{p} >= 0$, while the momentum uncertainty, defined as $\sqrt{< \vec{p}^2 > - < \vec{p} >^2}$ is just equal to $\sqrt{< \vec{p}^2 >}$. From the relation of the quantum operator, $p = \hbar k$, we have $< \vec{p}^2 >=< 2mE >$. With a reasonable assumption that the half of the real FWHM of the Ps peak in 2D-ACAR spectrum equals the momentum uncertainty of the Ps atoms in the microvoids, we can replace the k and E in equation 5.12 by σ_{real},

$$sin(\frac{\sqrt{3}\sigma_{real}a}{2\hbar}) = \pm\sqrt{\frac{3\sigma_{real}^2}{8mV_0}} \tag{5.11}$$

where number 3 represents three-dimensional and $m = 2m_e$ is the mass of Ps atom. By solving this equation numerically, with a definitive σ_{real}, we can find out how the diameter of the microvoids changes with the depth of the microvoids (in terms of bounding energy). Table 5.1 gives some numbers of a and V_0 for the ground state solution of equation 5.11 (Note that the σ_{real} is the ratio of the momentum of the Ps atom to the momentum of the 0.511 MeV γ-ray. In the calculation of $\sigma_{real}a$ and σ_{real}^2, the momentum of the γ-ray which equals to $\frac{E_\gamma}{c}$, where E_γ=0.511 MeV and c is the speed of light, should be taken into account.).

Oxide region	Depth V_0 (eV)	1.04	1.25	1.51	2.00	2.14	2.51	3.25	3.65	3.81	4.11	5.10	5.89	.	.
σ=3.2 mrad	Diameter of the well (Å)	5.04	5.74	6.17	6.60	6.71	6.89	7.15	7.26	7.30	7.35	7.44	7.61	.	.
Interface region	Depth V_0 (eV)	0.76	0.77	0.80	1.36	2.16	2.96	4.25	4.51	4.61	4.97	5.27	5.45	.	.
σ=2.8 mrad	Diameter of the well (Å)	4.62	5.55	5.79	7.37	8.02	8.35	8.65	8.69	8.72	8.77	8.81	8.83	.	.

Table 5.1: The relation between the depth and the diameter of the finite-spherical-well potential calculated from eq. 5.11 for the positronium atoms peak in the oxide and the interface spectra.

5.5.2 The Estimation of the Concentration of the Defects

The concentration of the defects (microvoids and vacancy-like) can be calculated from the relative intensity under each signal in the 2D-ACAR spectra. The most important defects observed in this experiment is the microvoids in both of oxide and interface regions. In performing the three-gaussian fit to the oxide and interface spectra, the narrowest component (with smallest σ) represents the signal from Ps atoms which are trapped into the microvoids. The relative intensity is defined as the ratio between the total counts under that narrow gaussian (component) and the total volume of the original spectrum. After the relative intensity is obtained, the positron trapping rate, c, can be calculated from eqs. 1.19 and 1.23 with known positron average lifetime, τ, in the corresponding region (oxide or the interface). Although positron lifetime measurement was not performed for this sample, the lifetime measurement was done on a MOS (metal-oxide-silicon) sample grown from the same wafer as the n-type

SiO_2-Si sample used in this experiment and with the same thickness of the oxide layer ($\sim$ 1170Å)[144]. Note that the Ps signal seen in the 2D-ACAR spectrum is only due to the para-Ps atoms, spin-singlet state of the Ps atom, because the energy window of the NaI detectors were set at 511 keV energy at which only the γ-rays from the para-Ps annihilation can be detected (the γ-ray energy from the ortho-Ps annihilation can have a continuous distribution and will fall outside the energy window of the detectors.). As described in section 1.6, the ratio between the spin singlet and triplet is 1:3 (although the ratio may change at very high magnetic field due to the magnetic quenching effect[145], the field of 0.4 $\sim$ 0.5 Tesla is not high enough to change the ratio). Thus, if the relative intensity of the Ps signal in the spectrum is

$$x_{para-Ps} = \frac{N_{para-Ps}}{N_{total}} \tag{5.12}$$

where $N_{para-Ps}$ is the total counts under the Ps signal and N_{total} is the total counts under the whole spectrum. Then the total fraction of those positrons which formed Ps and trapped into microvoids is

$$x_{Ps} = \frac{4x_{para-Ps}}{3x_{para-Ps} + 1} \tag{5.13}$$

While the fraction of positron annihilation in other kind of defects (vacancy-like) should be re-scaled accordingly from the relative intensity of the corresponding signal in the 2D-ACAR spectrum,

$$x_{vacancy} = \frac{N_{vacancy}}{N_{total} + 3N_{para-Ps}} \tag{5.14}$$

Knowing the Ps trapping rate, c, in the defects is not sufficient to calculate the concentration of the defects. Another important parameter is the positron trapping coefficient, κ, at the defects. The trapping coefficient, κ, can be obtained either from theoretical calculation or from the positron lifetime measurement with known

Defects / Item / Layer	Microvoids		Vacancy-like defects
	Diameter (angstrom)	Concentration	Concentration
Oxide region	10.4(6)	10^{16}/cm^3	N/A
Interface region	11.9(9)	10^{8}-10^{9}/cm^2	10^{10}/cm^2

Table 5.2: The size and the concentration of the defects in the oxide and the interface regions for the n-type sample. The diameter of the microvoids are estimated by using the infinite-spherical-well potential. Note that the concentrations are only accurate to the order of the magnitude.

concentration of the defects. Generally speaking, the trapping coefficient, κ, varies from 10^{16}/sec (negatively charged vacancy at low temperature) to 10^{14}/sec (neutral vacancy, temperature-independent, and negatively charge vacancy at room temperature). While for positively charged vacancies, the κ is as low as 10^{13}/sec [62, 27]. For the sake of safety, we take $\kappa \approx 10^{14}/sec.$, which should be reasonable for the defects at room temperature at which our experiments were done. After all of above preparation, we finally come to the stage of estimating the concentration of the defects observed in the 2D-ACAR measurement. Table 5.2 gives the result of the estimation (include the size of the defects if applicable) and the result on the concentration should be considered to be accurate to the order of magnitude due to the assumption made for the trapping coefficient.

5.6 Result on a p-Type SiO_2-Si Sample

To confirm the information obtained from the 2D-ACAR measurement for the n-type SiO_2-Si sample, a p-type sample was employed with the same thickness of thermal oxide grown under the same condition. Figure 5.18 shows the 2D-ACAR spectrum for the p-type sample and its fine structure at positron beam energy of 2 keV. Compared to the spectra for the n-type sample at the same beam energy (figs. 5.9 and 5.10), both of the original spectrum and its fine structure spectrum shows the same feature, *i.e.* the oxide (SiO_2) regions are the same for the n-type and the p-type sample.

To see the interface signal, the positron beam energy was tuned to 5.0 keV (with the mean depth of $\sim$ 2100 $\AA$) at which $\sim$ 14% of incident positron annihilate in oxide, 49% annihilate in bulk Si, and the remaining 37% sample the interface, calculated from the S-parameter measurement using the same procedure VEPFIT. Figure 5.19 shows the pure interface spectrum (after the subtraction of the fraction of oxide and bulk Si spectra) and its fine structure spectrum. Similarly, the sharp Ps peak appears in the center of the fine structure spectrum. The small bumps around the Ps peak is slightly different from those seen for the n-type sample. The explanation for this small but statistically significant difference is waiting for further investigation.

5.7 Investigation on an n-Type MOS Sample

The MOS (metal-oxide-silicon) is the basic building block of modern silicon-based electronics. The discovery of the MOS field-effect-transistor (MOSFET) made it possible to manufacture the modern very large integrate circuit (VLIC). The only difference between a bare SiO_2-Si and MOS is that an aluminum gate (generally $\sim$ a few hundred $\AA$) is produced on the surface of the oxide (gate oxide) and another layer

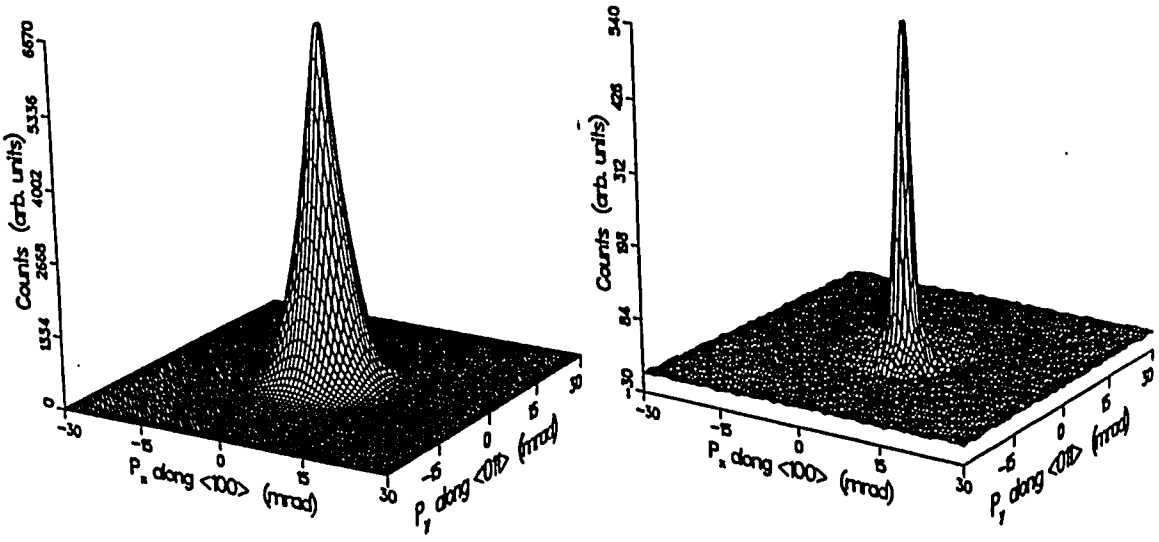

(a) (b)

Figure 5.18: The 2D-ACAR spectrum for a p-type SiO_2-Si sample at beam energy of 2 keV at which over 90% of incident positrons sample the oxide. (a) The original spectrum.(b) The fine structure spectrum

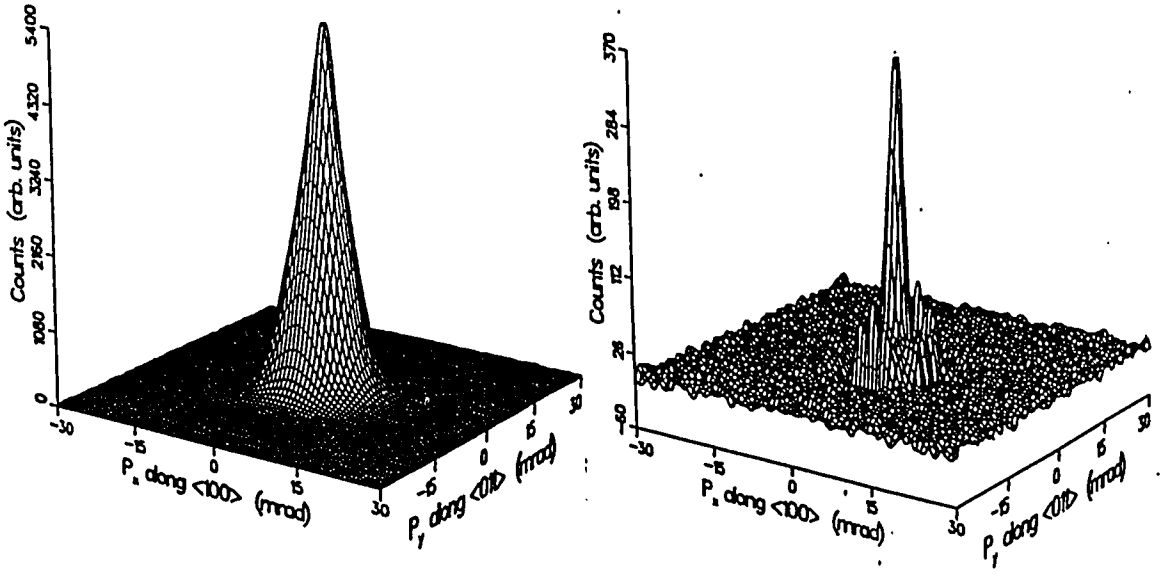

Figure 5.19: The pure interface spectrum for the p-type sample and its fine structure spectrum

of aluminum is coated on the back of the Si side. Thus, the electric properties of the sample can be controlled by applying appropriate electric field across the oxide and bulk Si through the Al gate. About the physics and technology of the MOS, there is a very detailed and comprehensive description by Nicolian and Brews[124]. The major advantage of using MOS sample in positron annihilation study of the SiO_2-Si interface is that the interface signal can be enhanced significantly by field-assisted diffusion of those positrons implanted to the bulk Si back to the interface. The effect of applying gate-voltage on the positron annihilation had been demonstrated by the S-parameter measurement (Doppler broadening)[147]. But the origin of the variation of the interface signal with the gate-voltage was not quite clear due to the limit of the technique. Positron 2D-ACAR technique is a proper probe to reveal the detailed information about the status of positron annihilation. In this section, the result of positron 2D-ACAR study of the n-type MOS sample will be presented. To avoid the contribution from the surface and the aluminum gate which is rather difficult to measure in the 2D-ACAR setup, higher beam energies were used to sample the interface region. The sample used in this experiment was an n-type MOS (SiO_2-Si) with a layer of aluminum evaporated on the surface of the oxide. The thickness of the aluminum gate is $\sim 600\mathring{A}$. The silicon single crystal was taken from the same wafer as n-type SiO_2-Si sample studied above and with a layer of $\sim 1170\mathring{A}$ thermal oxide grown under the same condition.

5.7.1 2D-ACAR Spectrum at Beam Energy of 6 keV

Figure 5.22 shows the spectrum taken at positron beam energy of 6 keV with 0 V bias on the gate (at neutral state of the gate). At that energy, the total contribution from the surface and aluminum gate is less than 5% and is negligible. Again, this spectrum

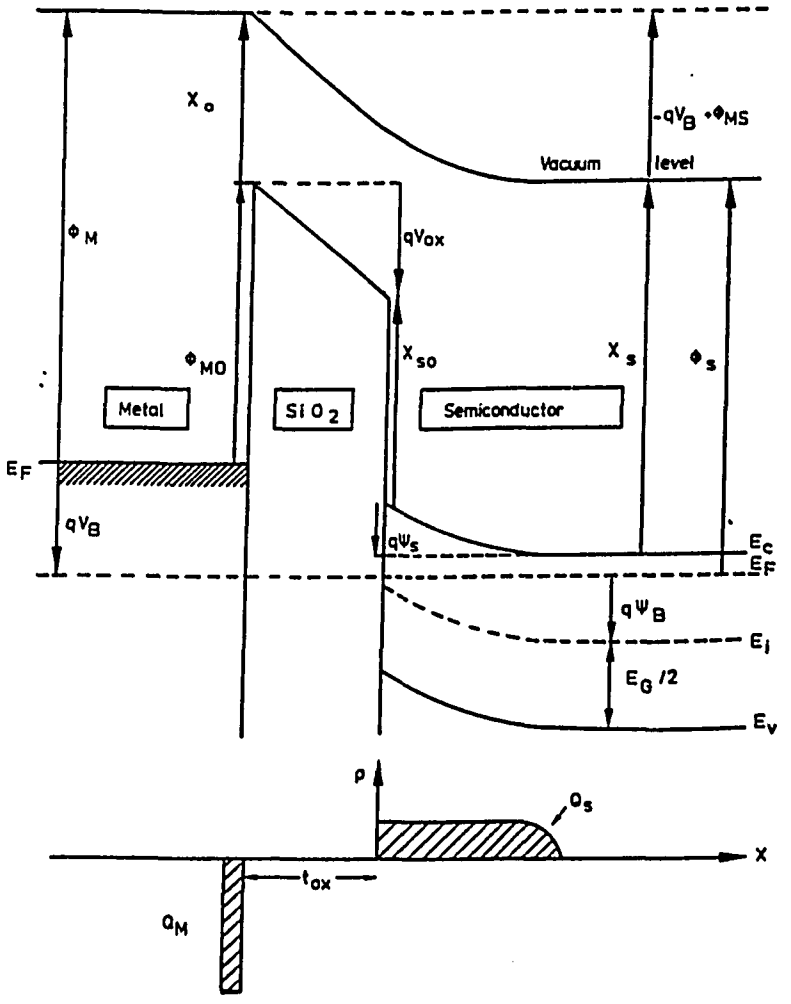

Figure 5.20: The configuration of the MOS sample and the effect of the applied gate-voltage on the band bending. From ref.[146].

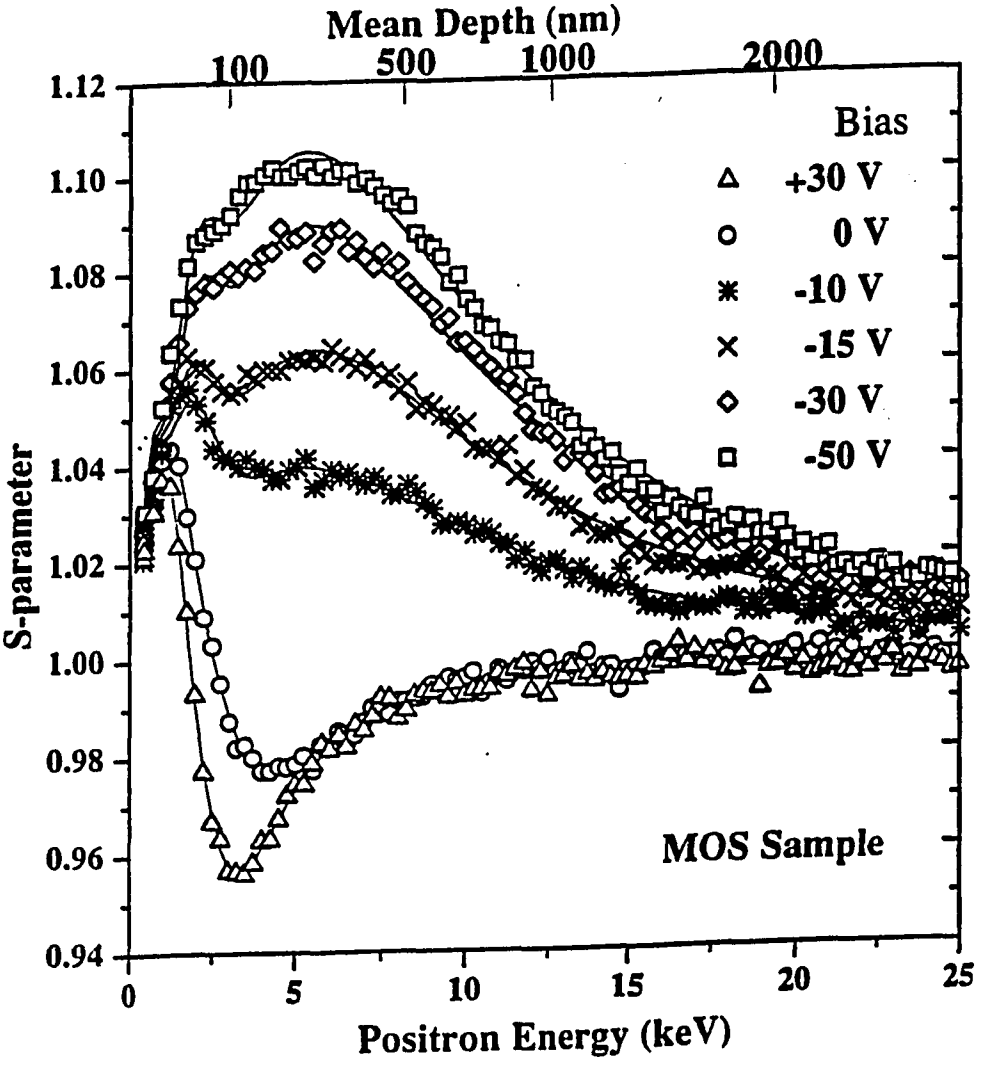

Figure 5.21: Result of Doppler broadening measurement on the n-type MOS–the variation of the interface signal with the applied gate-voltage. after ref[147].

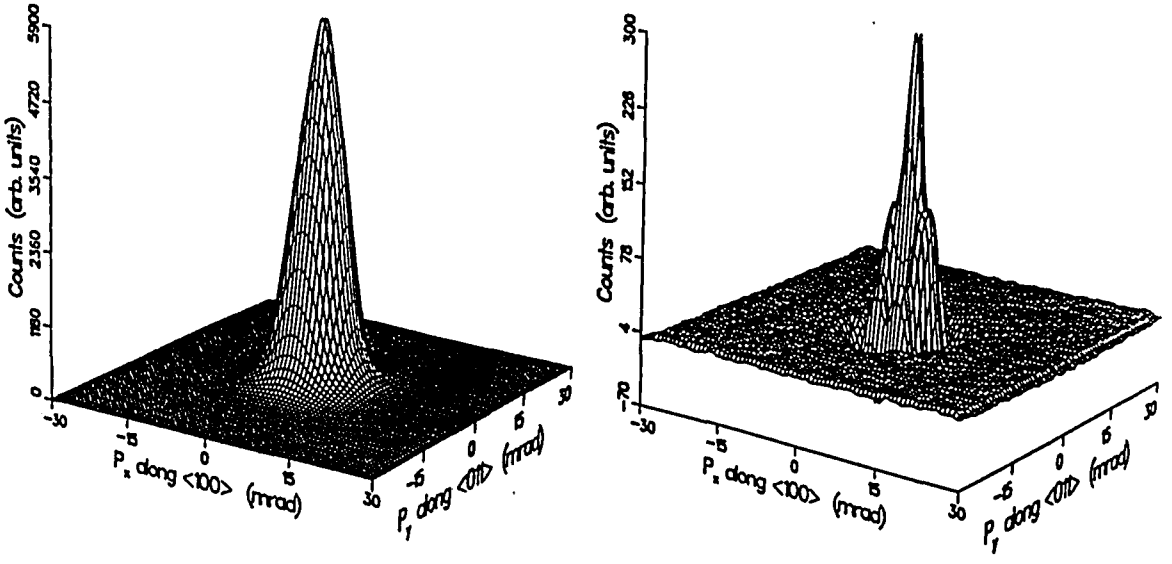

(a) (b)

Figure 5.22: The 2D-ACAR spectrum for the n-type MOS sample at positron beam energy of 6 keV with 0 V bias at the gate. (a) The original spectrum. (b) The spectrum showing fine structure.

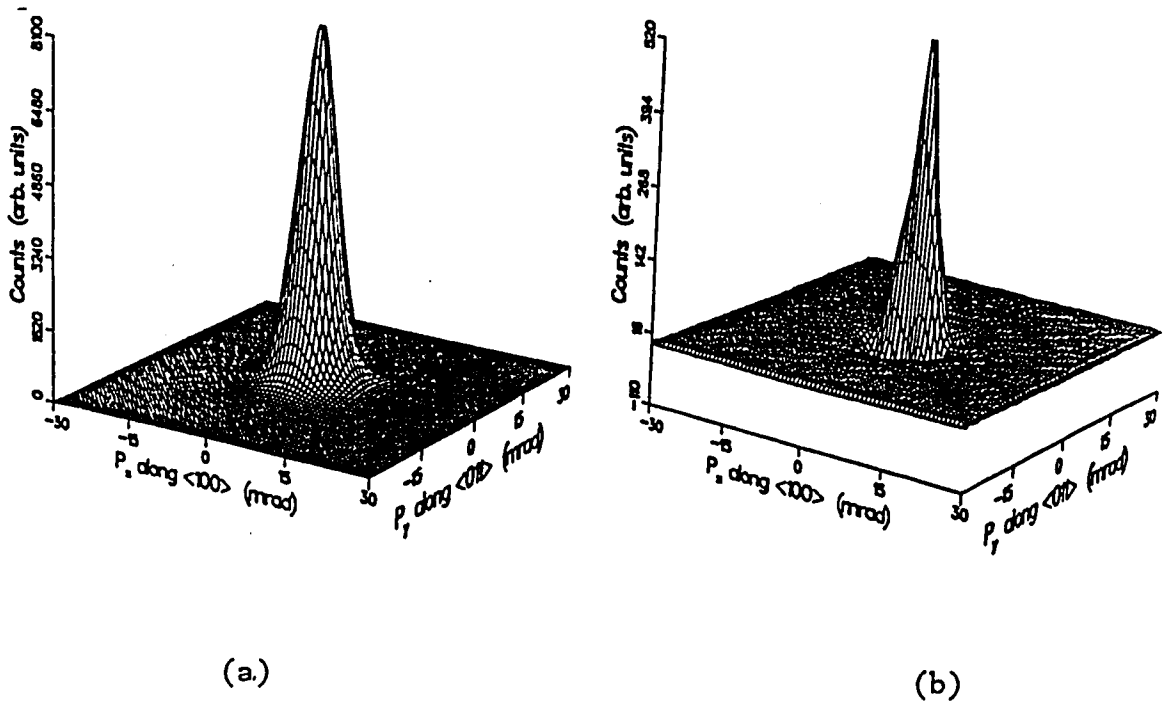

(a.) (b)

Figure 5.23: The 2D-ACAR spectrum at beam energy of 6 keV with gate bias of -15 V. (a) Original spectrum. (b) The fine structure spectrum.

is a mixture of positron annihilation at oxide, interface , and bulk Si single crystal, which can be seen clearly from the fine structure spectrum. Figure 5.23 shows the spectrum at the same beam energy but with a -15 V gate bias. Although this spectrum is still the mixture of positron annihilation at different regions, the contribution from bulk Si is much less than that in the spectrum at 6 keV with 0 V bias, which can be seen from the fine structure spectrum. The contribution from positron annihilation in oxide region is unchanged due to a very short positron diffusion length ($< 100\text{Å}$) and the result from S-parameter measurement had proven this point. The explanation for this change in the 2D-ACAR spectrum with the gate bias is as follows:

When a negative bias was applied to the gate, it would produce an electric field

across the oxide and the bulk silicon, pointing to the oxide direction. For an n-type silicon, this field would expel the electrons near the interface (Si side) towards the bulk Si and produce a depletion region (near the interface) at which minority carrier (hole) would be dominant. While this field attracts positrons in the bulk Si region diffuse back to the interface. Because of the depletion, there was no barrier in the way of positron back to interface. Thus, a large fraction of the thermalized positrons implanted to the bulk Si would diffuse back to interface. That is why the bulk Si signal significantly decreased while the structures characteristic of interface feature (Ps formation and trapping in microvoids and positron annihilation in the vacancy-like defects –probably the P_b centers) increased. By taking the difference between the spectrum with -15 V bias and the one with 0 V bias, the remaining spectrum would contain no oxide (and aluminum gate) fraction. Figure 5.24 shows the difference spectrum (the one with -15 V bias minus the one with 0 V bias with the two spectrum normalized to the same volume). The sharp central peak in difference spectrum indicates the Ps formation and trapping in microvoids and positron annihilation in the vacancy-like defects. This further confirm our previous interpretation of the information obtained from the bare SiO_2-Si sample. It is worthwhile to mention that there is a different opinion about the field-assisted diffusion of positrons in MOS samples originated recently from the S-parameter measurement[148]. To explain the results from S-parameter measurement, the authors concluded that the diffused positrons from bulk Si do not stop at the SiO_2-Si interface, instead, they stop at the Al-SiO_2 interface. Although there is no evidence from our measurement to support this idea (even from the point of view of leakage current measurement), it could be possible, depending on the quality of the oxide.

Figure 5.25 shows the spectrum taken at 6 keV with a gate-bias of +15 V. At

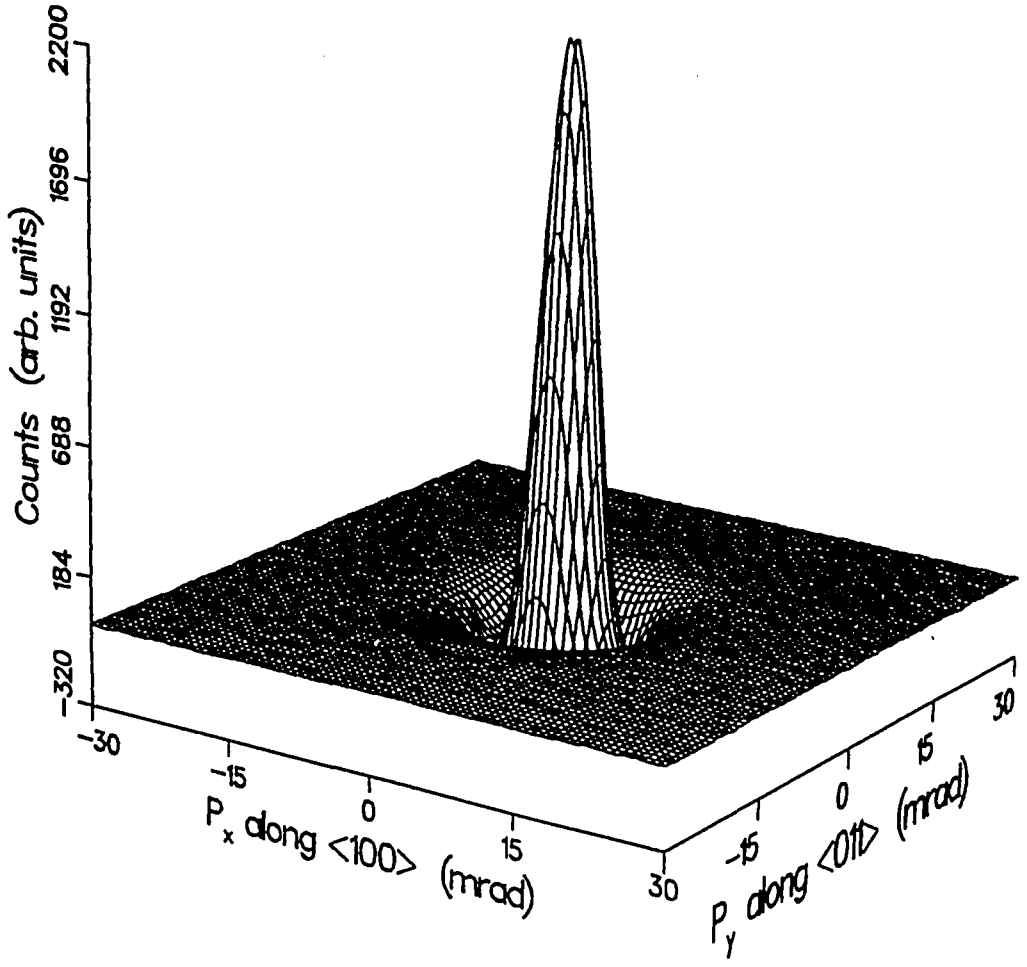

Figure 5.24: The difference spectrum between the spectrum with -15 V gate-bias and the one with 0 V gate-bias.

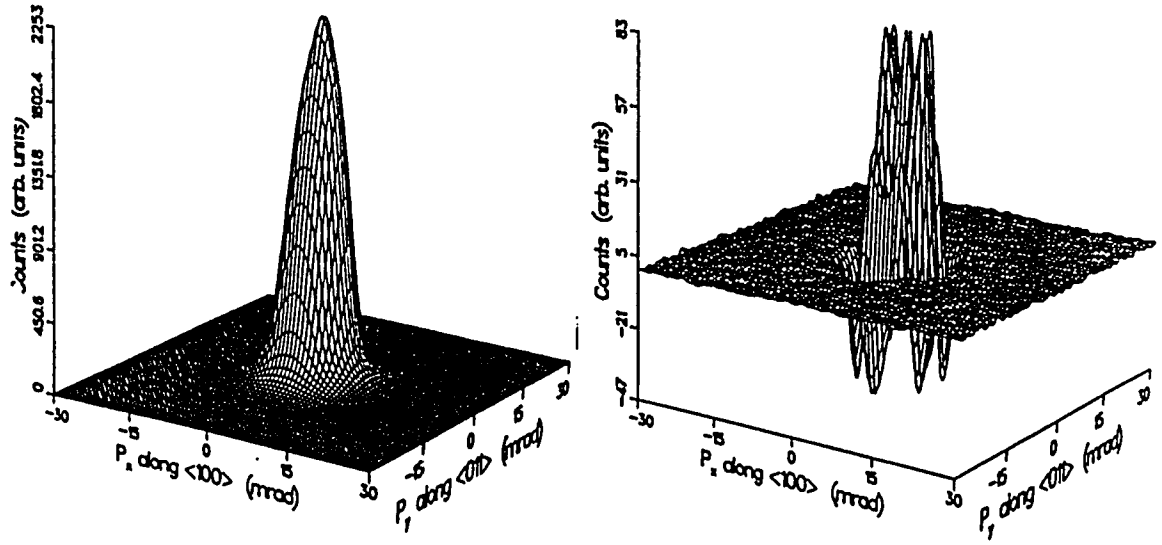

(a) (b)

Figure 5.25: The spectrum at beam energy of 6 keV with a gate-bias of +15 V. (a) The original spectrum. (b) The fine structure spectrum.

that bias, the electrons in the bulk Si would be attracted to the interface region and formed a accumulation layer which would hinder the thermalized positron diffusion from bulk Si to the interface. Thus, in this spectrum, the major feature is that of bulk Si and a small feature from positron annihilation in oxide (which contributes an small central peak characterizing Ps formation and trapping in microvoids.), while the contribution from interface is very small because the interface signal depends largely on the diffusion of the positrons in the bulk Si.

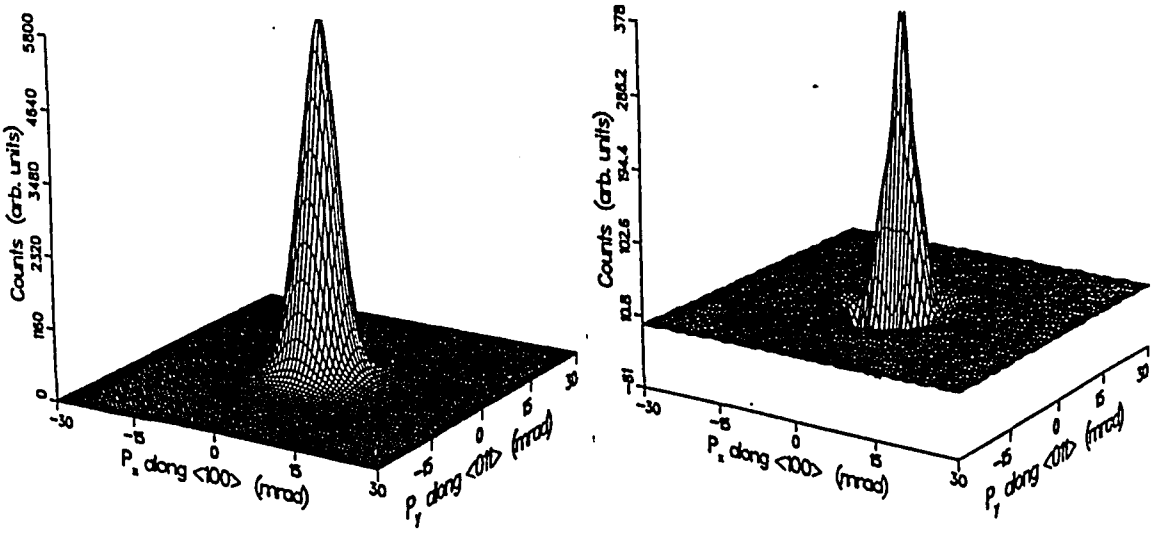

(a) (b)

Figure 5.26: The spectrum at beam energy of 7 keV with -30 V gate bias. (a) The original spectrum. (b) The fine structure spectrum.

5.7.2 2D-ACAR Spectrum at Even Higher Beam Energies

To study the field effect on the positron diffusion, higher (than 6 keV) beam energies with different biases were employed on the 2D-ACAR study of the MOS sample. Figure 5.26 shows the spectrum taken at beam energy of 7 keV with a bias of -30 V. The spectrum is quite similar to the one taken at beam energy of 6 keV with a bias of -15 V, indicating that almost all of the positrons implanted to bulk Si originally diffuse back to interface in both cases (a saturated interface signal).

5.8 2D-ACAR Study of a SiO_2-Si Sample with Thinner Oxide

As the progress of the Si technology and the requirement of the faster devices, the oxide on the surface of silicon single crystal becomes thinner and thinner. Technically, it will take much shorter time to grow thinner oxide than thicker oxide and it will be much easier to control the quality of a thinner oxide. In last few years, the thickness of the oxide layer had changed from $\sim 1000\mathring{A}$ to $\sim 100\mathring{A}$. The sample studied above should belong to the last generation, being the state-of-the-art sample.

It would be interesting to know the quality of the SiO_2-Si interface for the state-of-art sample available presently. As a systematic study of the physically and technologically important SiO_2-Si interface, positron 2D-ACAR measurement was performed on a p-type SiO_2-Si sample with a much thinner oxide layer. The state-of-art sample was supplied by AT&T Bell Laboratories. The wafer is a p-type Si(100) single crystal with a layer of gated oxide (the best technology of growing oxide today). The thickness of the oxide layer is $\sim 150\mathring{A}$. Figure 5.27 shows the result of S-parameter measurement. Unlike the thicker oxide sample, the interface signal is inseparable from the surface and oxide signals because of the limit of the spatial resolution of the technique (or due to positron implantation profile). The entangling of oxide and interface signals makes the calculated result on the annihilation fraction by the program VEPFIT unbelievable. Thus, the wise way to obtain the interface signal (if any) would be choosing a proper beam energy to avoid the oxide annihilation but allow a reasonable amount of thermalized positron in the bulk Si diffuse back to interface. The net (or pure) interface signal can be obtained by subtracting the bulk Si contribution (bulk Si spectrum is much easier to obtain.). In this experiment, two spectra were taken.

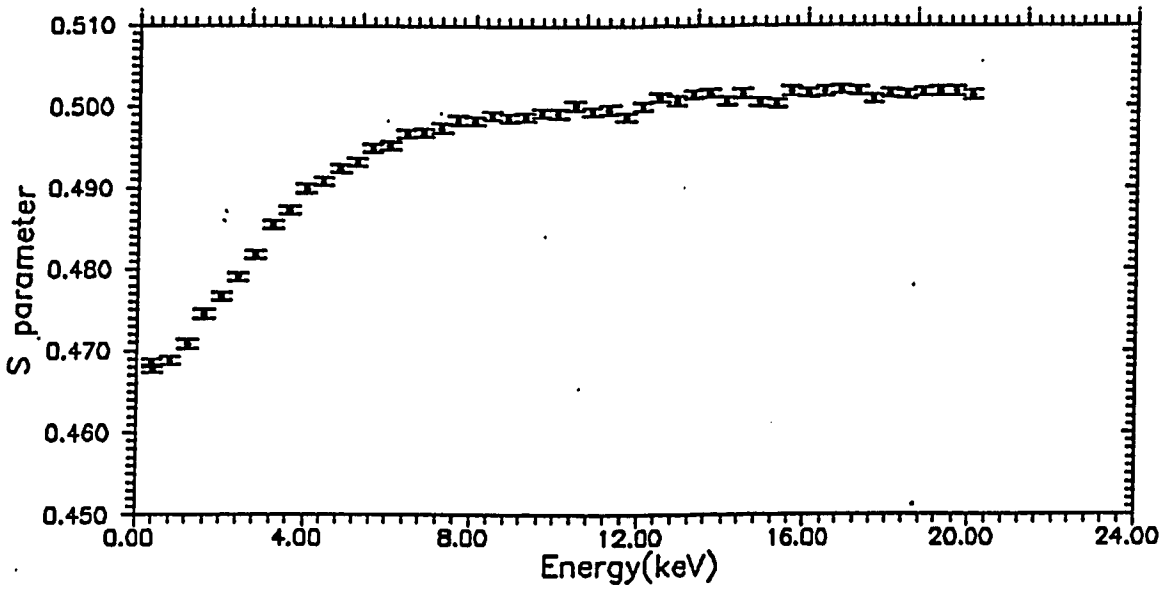

Figure 5.27: S-E curve for a p-type SiO_2-Si sample with a thinner gated oxide.

The first spectrum was taken at beam energy of 2.5 keV at which only 3% of positron annihilating in oxide, calculated by integrating the implantation profile (eq. 1.3) over the thickness of the oxide (assume there is no diffusion of positron from oxide to bulk Si), to get the mixed spectrum from the interface and bulk Si. Then another spectrum was taken at beam energy of 12.5 keV at which $\sim$ 100% of the incident positrons annihilate in bulk Si. Figure 5.28 shows the spectrum at beam energy of 2.5 keV at which the mean implantation depth is $\sim 770\AA$ and the spectrum at beam energy of 12.0 keV at which the mean depth is $\sim 9500\AA$. While the interface signal can be seen by taking the difference between the two spectra.

$$N_\alpha(p_x, p_y) = N_{2.5keV}(p_x, p_y) - \alpha N_{12.5keV}(p_x, p_y) \tag{5.15}$$

where α is the fraction of positron annihilation in bulk Si which is contained in the spectrum at 2.5 keV, $N_{2.5keV}(p_x, p_y)$. Because the feature from bulk Si(100) single crystal is well known, the bulk Si(100) contribution to the spectrum at 2.5 keV can be minimized by varying the fraction α until the bulk Si feature disappears

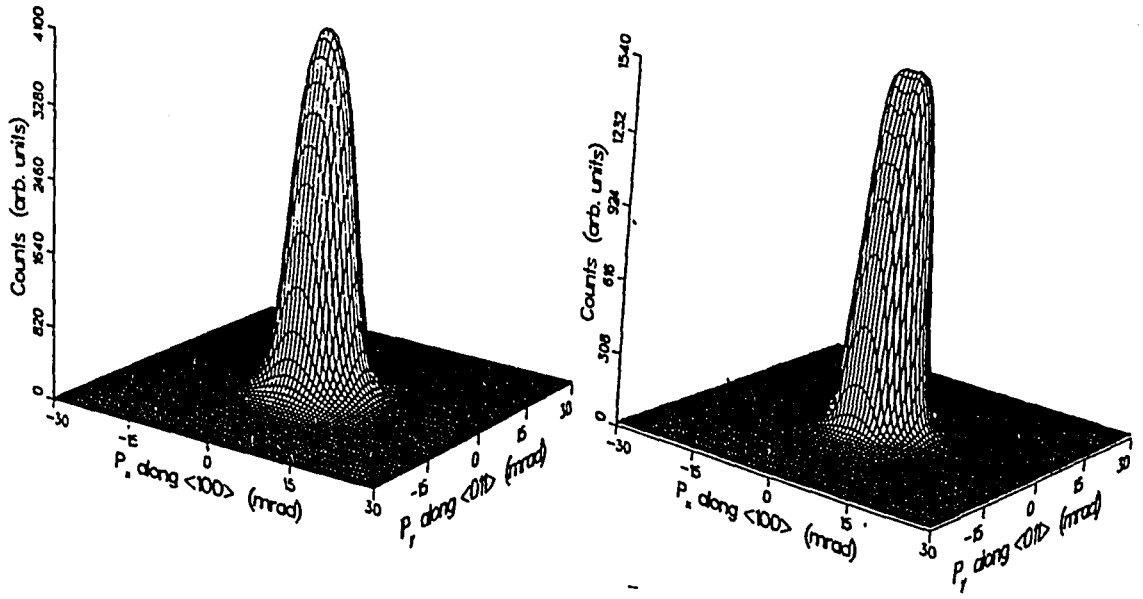

(a) (b)

Figure 5.28: 2D-ACAR spectra for the SiO_2-Si sample with $\sim$ 150Å gate oxide. (a) The spectrum taken at beam energy of 2.5 keV. (b) The spectrum with beam energy of 12.0 keV.

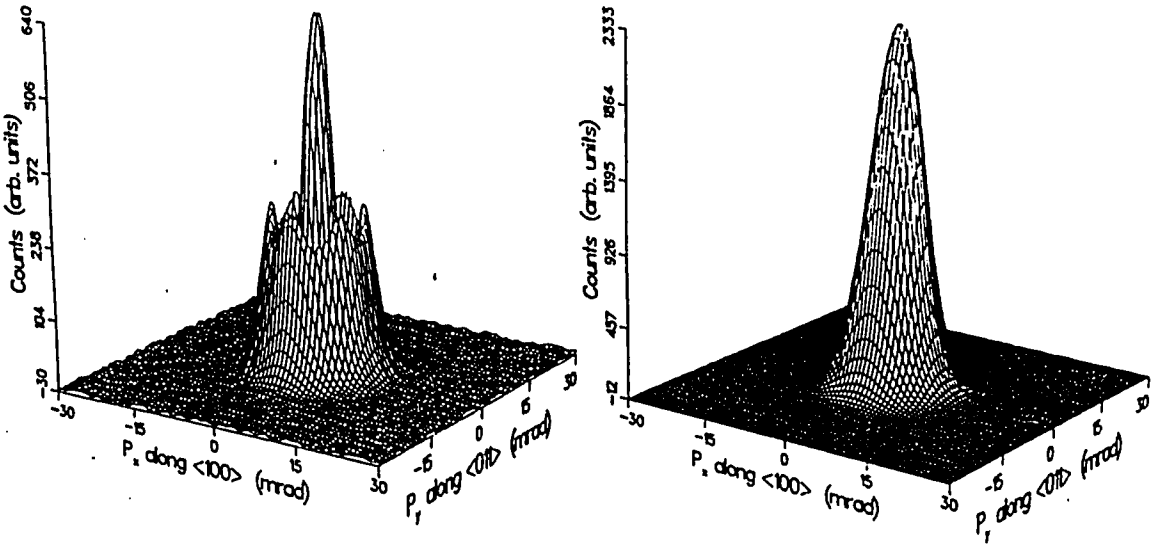

(a) (b)

Figure 5.29: The difference spectra, $N_\alpha(p_x, p_y)$, with different α. (a) α=1.0. (b) α=0.6.

in the remaining spectrum, $N_\alpha(p_x, p_y)$. Figure 5.29 shows the spectra, $N_\alpha(p_x, p_y)$, with α=1.0 and 0.6, respectively. From the spectrum, $N_{\alpha=1.0}(p_x, p_y)$, a sharp peak appears in the center of the spectrum, indicating Ps formation in the interface region. While with α=0.6, the bulk feature almost disappear completely. Thus the spectrum, $N_{alpha=0.6}(p_x, p_y)$ can be considered as the pure (or net) interface spectrum. From its fine structure spectrum, a central sharp peak and a slightly broader component surround it can be seen, indicating Ps formation and trapping into microvoids and

positron annihilation in vacancy-like defects. The result is similar to that for the sample with thicker oxide layer.

Chapter 6

Study of Native Point Defects in Bulk Semi-Insulating GaAs

The experiments on the 2D-ACAR study of the point defects in semi-insulating (SI) GaAs were performed in the bulk chamber (see figs. 3.2 and 3.3). The purpose of the investigation is to reveal the electronic structure of the native point defects[70] in atomic scales. The native defects exclude those caused by foreign atoms or impurities. The simplest native point defects include vacancies, interstitials and antisites. The experimental results will be given in the following sections. A brief introduction to GaAs (Here we follow the discussion given by Blackemore[149].) and the point defects associated with it will be given first.

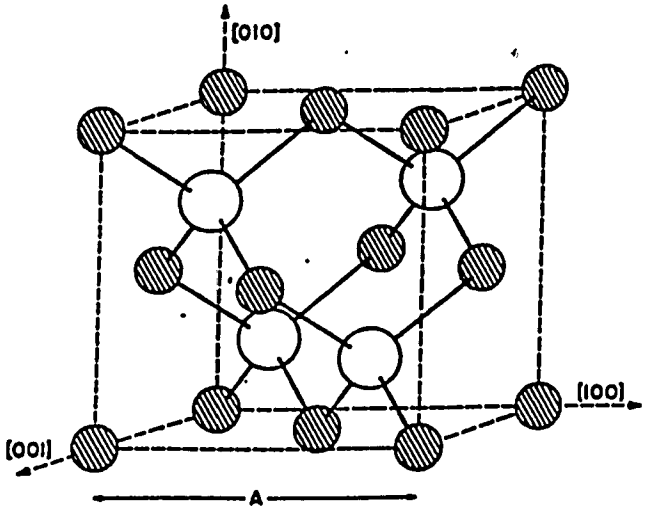

Figure 6.1: The conventional unit cube for GaAs with a volume A^3 that is four times larger than that of a primitive cell.

6.1 The Physical Properties of GaAs

6.1.1 The GaAs Single Crystal

The GaAs single crystal was first created by Goldschmidt[150] in 1920s and was found that it had the structure of zinc-blende lattice, i.e. face-centered-cubic (FCC) translational symmetry. Figure 6.1 illustrates the lattice structure of GaAs. The two interpenetrating FCC sublattice, one is for the gallium atoms (Ga) and the other for the arsenide atoms (As), form the FCC lattice with a basis: one atom (Ga) at (0,0,0) and the other atom (As) at $(\frac{1}{4}, \frac{1}{4}, \frac{1}{4})$. The nearest neighbor bond length is $r_0 = \frac{\sqrt{3}A}{4}$, and such bonds (Ga to four As neighbors and As to four Ga neighbors) are mutually separated by the tetrahedral bond angle $\psi = cos^{-1}(-\frac{1}{3}) = 109.47°$. X-ray diffraction measurements in the 1960s of the unit cell size[151, 152] give that:

$$A_{300} = 5.65325 \pm 0.00002\mathring{A} \tag{6.1}$$

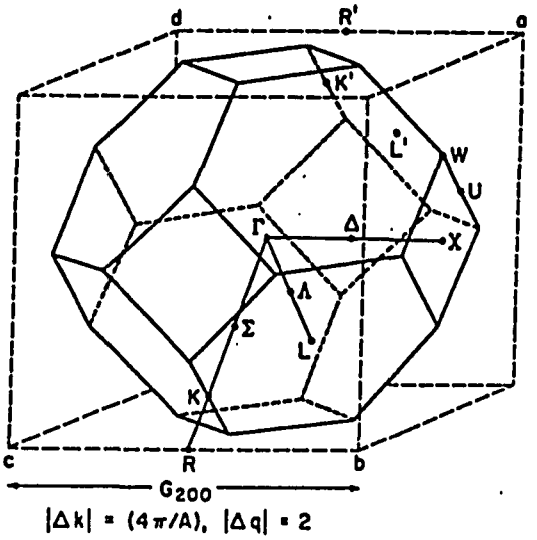

Figure 6.2: The first Brillioun zone for the GaAs lattice: the same as for other solids with diamond, zinc-blende, or FCC lattices.

and the crystal density at 300 K

$$\rho = 5.3174 \pm 0.0026 g/cm^3 \tag{6.2}$$

for stoichiometric GaAs from direct weighing experiments[151].

6.1.2 Reciprocal Space: The Brillouin Zone

The crystal structure of GaAs has imposed body-centered-cubic (BCC) symmetry on the reciprocal space, the coordinates system needed for description of the dispersion of lattice vibrations and of electronic states. Figure 6.2 shows the first Brillouin zone (BZ) of reciprocal space for GaAs. The zone comprises a truncated octahedron, lying

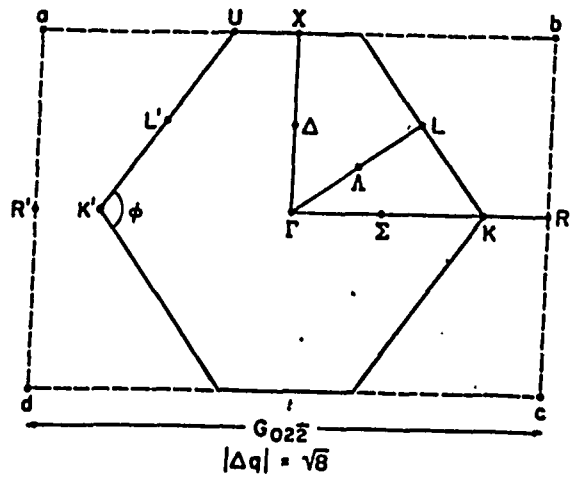

Figure 6.3: The hexagonal cross section of the GaAs first Brillouin zone as intersected by the (011) plane. This is not a regular hexagon.

within a cube (shown with dashed lines) with a wave-vector space ($\vec{k}$-space) side length $(\frac{4\pi}{A}) = 2.223 \times 10^8 cm^{-1}$.

Positron 2D-ACAR measurement in single crystal gives the projection of the first BZ along a selected direction which is usually coincident with a major axis direction. For the sample we studied, the projection (integration) direction is along the $< 011 >$ direction. Thus, we are more interested in the plane section through the zone center. Figure 6.3 shows a (011) plane section of the BZ.

6.1.3 Energy Bands and Gaps

About the models of the bonding of GaAs, there have been expressed differences of opinion concerning the ionic:covalent balance. A partly ionic bond can be considered to resonate between covalent and ionic charge distributions which gives a stronger bond than a strictly covalent one. In principle, the ionicity fraction f_i represented in the energy-minimized wavefunction can be calculated by a variational method, provided the wavefunctions for covalent and ionic limits can be simulated properly. The calculation by Coulson *et al*[153] using atomic orbitals, as in tight binding, gave a charge transfer of 0.46e from Ga to As in solid GaAs. Sirota[154] inferred that the charge transfer from Ga to As would have to be $\geq$0.36e.

The 4s and 4p subshells contribute eight electrons per GaAs primitive basis, three from Ga and five from As. The real bond status lies between the two extreme cases: (1) totally covalent bond, with the eight electrons equally shared , would be $Ga^{-}As^{+}$, with one electron transfer to Ga. (2) The ionic $Ga^{+3}As^{-3}$. Thus, the appropriate bonding model should be $Ga^{+x}As^{-x}$ with $x \approx 0.4$ as mentioned above.

Herman[155] made one of the earliest band calculation for GaAs, using the orthogonalized plane wave (OPW) method which he had employed so successfully for the silicon and germanium band calculations[119, 156, 157], and benefited from the gross similarities of the valence and conduction band systems for the diamond structure Group IV elements and the zinc-blende structure of III-V compounds in general and of isoelectronic Ge and GaAs in particular.

Since then, several workers had made the band structure calculations for GaAs using various methods[120, 158, 159, 160, 161, 162]. Despite some small differences on the scale of energies, the results from different approaches were fairly consistent. Figure 6.4 gives the currently accepted features of the calculated band structure.

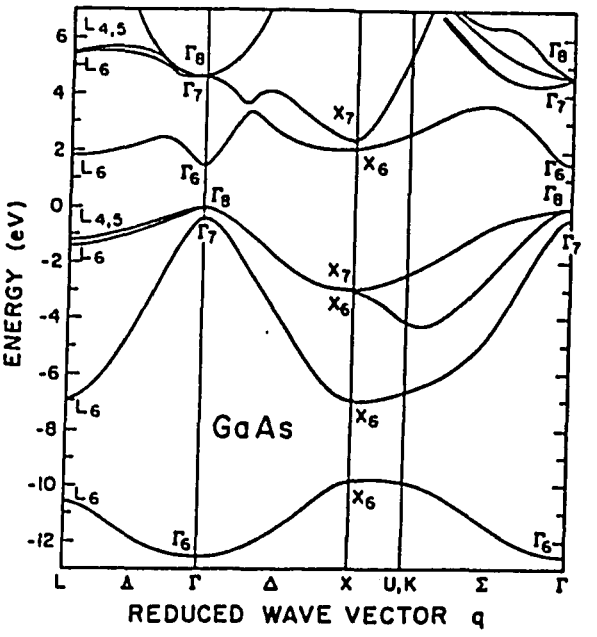

Figure 6.4: Electron energy vs reduced wave vector, for the four GaAs valence bands and the first several conduction bands, calculated by Chelikowsky and Cohen[161] from a nonlocal EPM approach.

The most interesting feature of the GaAs band structure is the direct band gap, i.e. the highest point (in energy) of the valence bands and the lowest point of the conduction band located at the same position in $\vec{k}$ coordinates, which makes GaAs to be one of the best candidates for optoelectronic devices. Figure 6.5 shows more detailed structure of the bands near the zone center in smaller scale. As shown in figure 6.5, the direct intrinsic band gap is 1.42 eV at room temperature. A variety of optical experiments has provided information concerning the direct intrinsic gap and its temperature dependence. The relevant experiment include: room temperature reflectance[163] and absorption[164], absorption extended from room temperature up to 973 K[165], absorption [166] and reflectance[167] extended from room temperature down to liquid hydrogen and liquid helium range. An emperical equation, requiring the choice of three parameters, was proposed by Varshni[168] to represent the

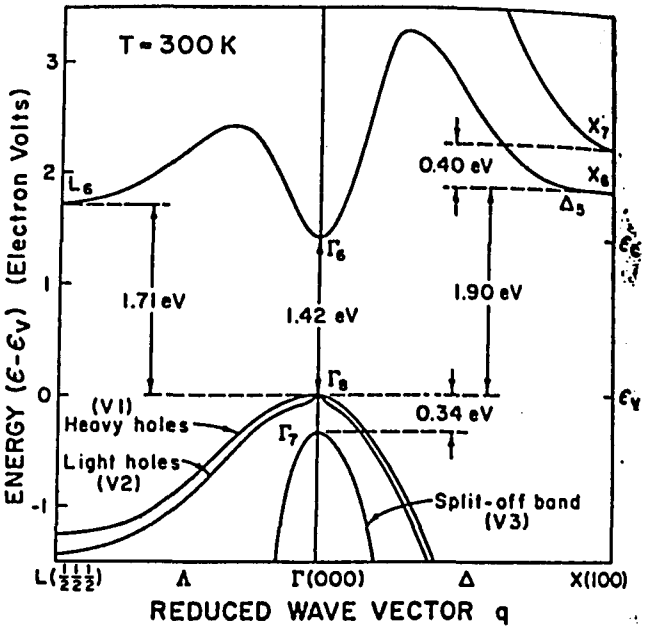

Figure 6.5: Variation of energy with wave vector for the uppermost part of the valence band system and for the lowest sets of conduction band minima. The energy gaps are shown for room temperature. From ref.[149].

temperature dependence of the band gap:

$$\epsilon_i(T) = \epsilon_{i0} - \frac{\alpha T^2}{(T+\beta)} \tag{6.3}$$

The values of the parameters $\epsilon_{i0}, \alpha, \beta$ were reported by several authors by fitting their experimental data[168, 169]. Among which, Thurmond's result[169] were widely used. He suggested the numerical form:

$$\epsilon_i(T) = 1.519 - \frac{5.405 \times 10^{-4} T^2}{(T+204)} eV \tag{6.4}$$

for GaAs in the temperature range of $0 < T < 1000K$ and estimated a standard deviation of $\sim$ 3 meV.

6.1.4 Vacancy Defects in GaAs

Once a GaAs crystal is grown, there must exist some defects in the crystal during the growth, called intrinsic or native defects. Among which, point defects play important

roles because they may form the basis of other defects. The point defects in GaAs include vacancies, interstitials, and antisites in both the As and Ga sublattices. At the first stage of positron 2D-ACAR study of defects in semiconductors, simple point defects are the good subject to begin with as the definition of the experimental data and the theoretical calculation are easier. Generally speaking, the effects of the point defects to the electronic properties of semiconductors are to produce energy levels in the "forbidden region" of the energy spectrum of perfect single crystal. Those levels may change the electrical and optical properties of semiconductors dramatically. Figure 6.6 is the calculated energy levels of point defects within the band gap of GaAs. Because positron annihilation method is sensitive to open volume related defects, we will concentrate our effort on the vacancy defects. About the discussion of other point defects (interstitials and antisites) can be found elsewhere[70]. As shown in fig.6.6, the As vacancy (V_{As}) is a donor with shallow donor levels near the bottom of the conduction band and the Ga vacancy (V_{Ga}) is a acceptor with shallow acceptor levels above the top of the valence band. For the semi-insulating GaAs (SI-GaAs), the Fermi-level (or the chemical potential) which separates the occupied (below it) energy levels and unoccupied (above it) energy levels will stay at midgap in the temperature range of $0 \sim 300$ K. Therefore, at this temperature range, the As vacancies are ionized (positively charged) – one or two electrons from each V_{As} are thermally excited to the nearest conduction band. Because the energy levels of the Ga vacancies locate below the Fermi-level, they will be negatively charged by capturing one or two electrons from the valence band nearby at that temperature range.

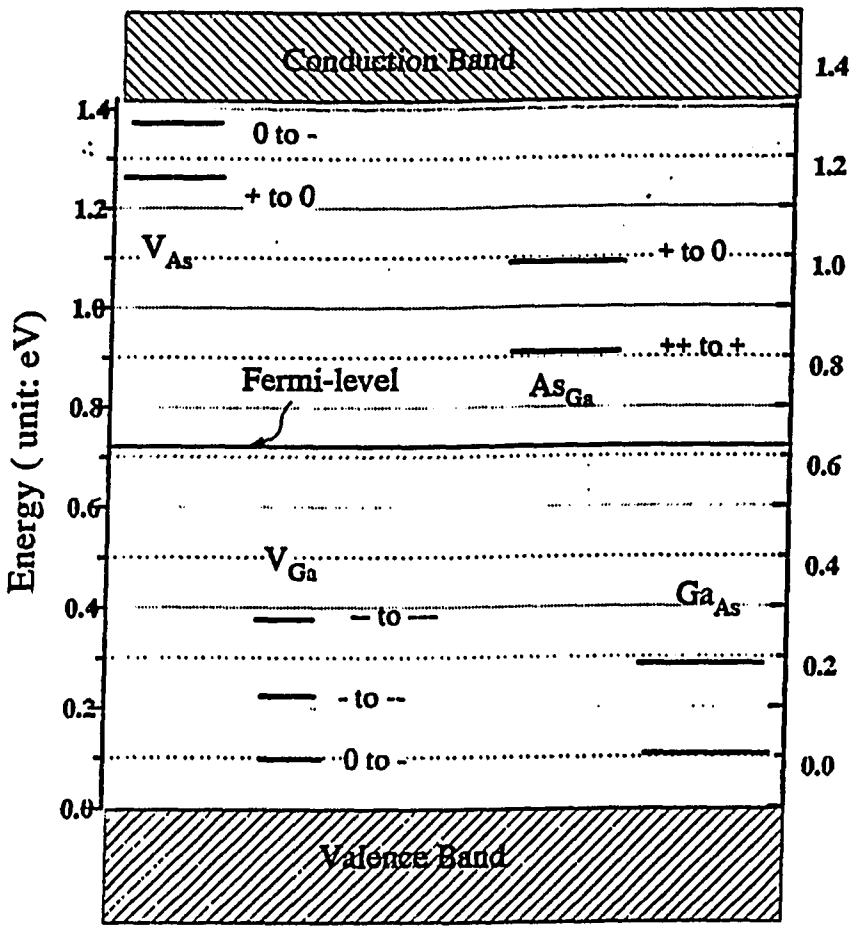

Figure 6.6: The calculated energy levels of point defects in the for GaAs. From Puska *et al*[170].

6.2 Positron 2D-ACAR Study of the As Vacancy in GaAs

In this section, we will present our experimental result in the study of the V_{As} in SI-GaAs using positron 2D-ACAR coupled with *in situ* photoexcitation. The experiment was done at temperature range of 20 K to room temperature. In this temperature range, the As vacancies are positively charged under normal condition. Thus, positrons can not be trapped into the defects due to the Coulomb repulsion. To make positrons trapped into the vacancies, we have to change the charge status of the defects by proper methods. In this experiment, we use infrared light of appropriate wavelength to excite electrons from valence band to the defect levels. In this way, we can get information about the momentum distribution of the annihilating $e^+ - e^-$ pairs at the vacancies by comparing the 2D-ACAR spectrum at darkness with the spectrum taken under photo-illumination.

6.2.1 Experimental Setup

To populate electrons to the V_{As} levels shown in figure 6.6, we mount a light-emission-diode (LED) right behind the sample, inside the vacuum chamber. Figure 6.7 shows the side view of the experimental setup. The LED used here is made of InGaAs which gives a photopeak at 930 nm at room temperature with a bandpass of ~50 nm, corresponds to an photon energy of 1.32 $\pm$ 0.05 eV. As the temperature changes, the energy of the emitted photons changes too, following the same formula as the band gap of GaAs (Eq. 6.4). Therefore, by keeping the sample and LED at same temperature the changes in the energy levels of As vacancy (relative to the band gap) can be compensated by the changes in the photon energy from the LED.

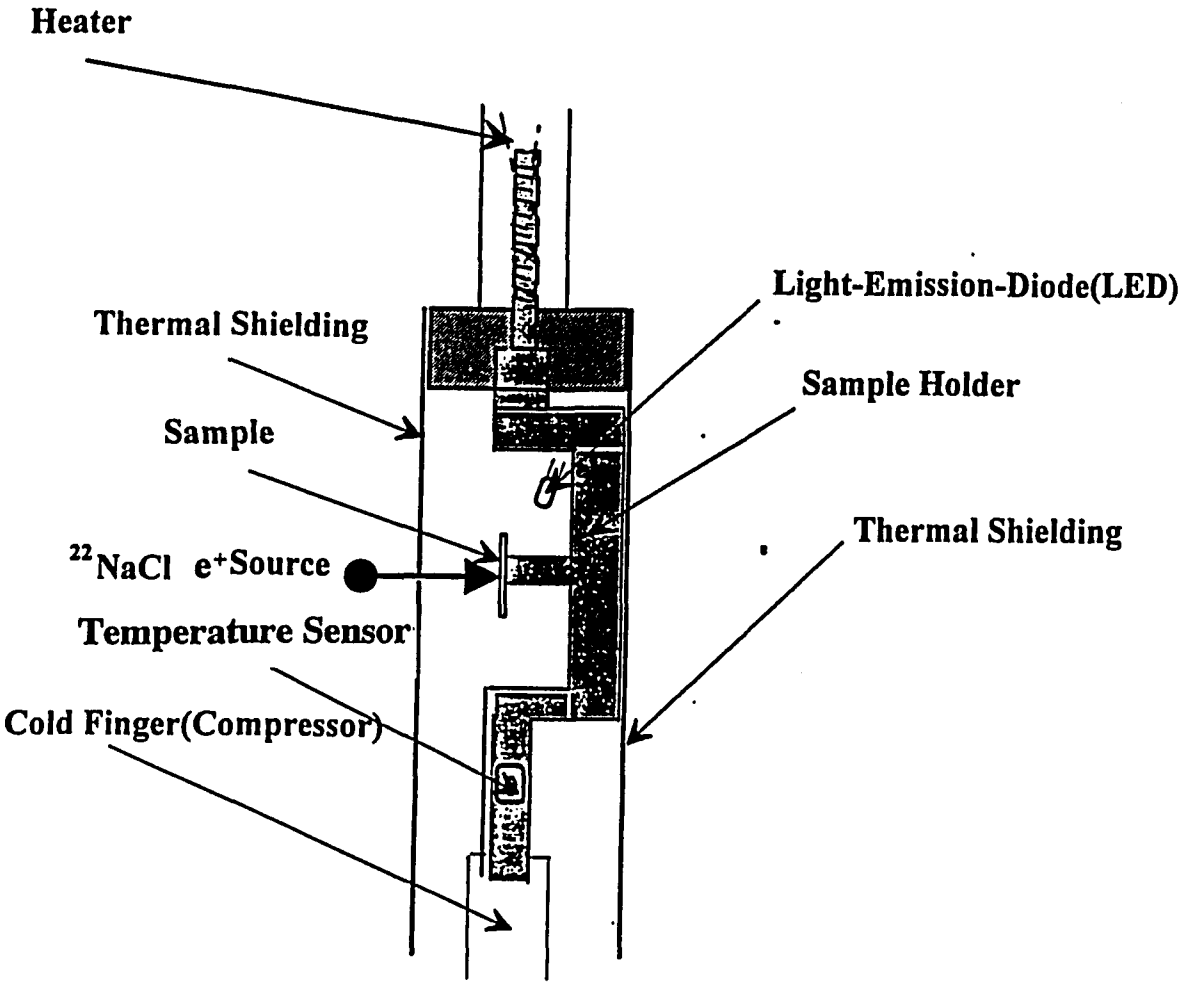

Figure 6.7: The side view of the experimental setup–inside the vacuum chamber.

6.2.2 The Sample–Semi-Insulating GaAs

The sample investigated was an undoped SI-GaAs(100) single crystal, grown with liquid-encapsulated Czochralski method. The EL2 defects concentration is $\sim 10^{16}/cm^3$. The dimension of the sample is $5 \times 10 \times 0.4$ mm^3. The implantation profile of positrons emitted from a radioactive source (for example, ^{22}Na, ^{64}Cu and $^{58}Co\ldots$) is characterized by the semiempirical formula given in sect.1.3 (eqs. 1.1 and 1.2). For the ^{22}Na β^+ source used in this experiment, the endpoint energy , $E_{max} \simeq 0.56$ MeV, and the density of GaAs is 5.6 g/cm^3, the "mean depth", $\frac{1}{\alpha_0}$, is $\simeq$ 49 microns. With a thickness of 400 microns, 100% of positrons implanted will annihilate inside the bulk GaAs (The backscattering from the surface may represent $10 \sim 20\%$[171], which will not cause background to the spectrum due to the strong guiding capability of the magnetic field).

The GaAs(100) sample was oriented such that the positrons impinged on the sample along the $< 100 >$ direction and the integration direction of the momentum, p_z, is along the $< 0\bar{1}1 >$ direction. The resultant 2D-ACAR spectra present a positron-electron momentum density map with $p_x \rightarrow < 100 >$ and $p_y \rightarrow < 011 >$.

6.2.3 2D-ACAR Spectrum in Darkness

As the most of the optical phenomena of GaAs happen at low temperature, we first cool the sample down to $20 \sim 30$ K and then took spectrum after the temperature stabilized (there are some differences between the spectra at room temperature and at low temperature due to the thermal expansion and contraction of the crystal lattice). Figure 6.8 shows the positron 2D-ACAR spectrum of semi-insulating GaAs at $\sim$ 30 K with a vacuum level of $10^{-8} \sim 10^{-7}$ torr. The spectrum comes from positron annihilation with core electrons, valence electrons and conduction electrons.

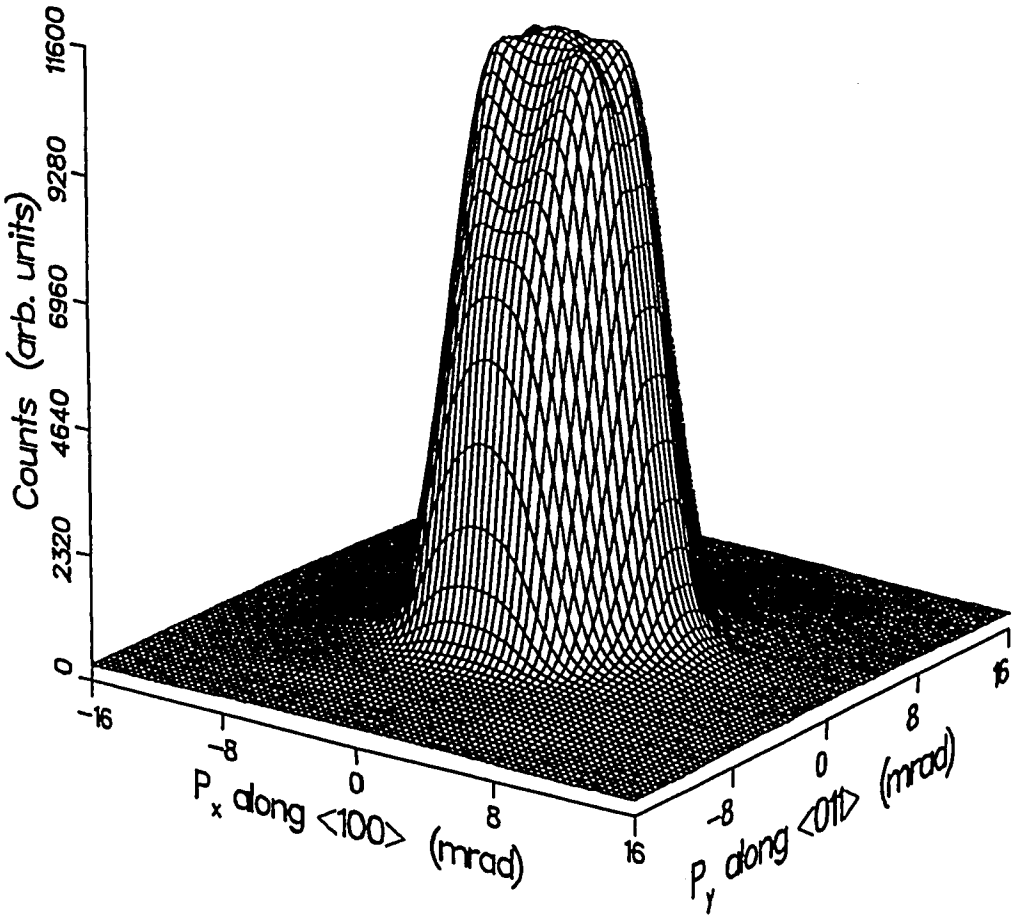

Figure 6.8: Positron 2D-ACAR spectrum for GaAs in darkness at low temperature.

The contribution from positron annihilation with the conduction electrons is negligible because the density of conduction electron is very small ($\leq 10^7/cm^3$). The contribution of positron annihilation with core electrons would be a broad symmetric component due to the large momentum of the core electron and the average of the orientation of the core electron orbits. Besides, the contribution from the annihilation with some of the valence electrons may be isotropic too, if their wavefunctions are spherically symmetric (the wavefunction of the thermalized positron is always isotropic), and should be narrower due to a relatively smaller momentum of the valence electrons. After the subtraction of this broad component, the residue spectrum is the contribution of the positron annihilation with valence electrons which have anisotropic wavefunction. Figure 6.9 shows the anisotropic spectrum of the GaAs at low temperature. Because the shape of the momentum distribution of valence electrons is reflected by the geometry of the first Brillioun zone, and the integration direction for 2D-ACAR spectrum is along the $< 0\bar{1}1 >$ axis direction, the contour plot of the anisotropy spectrum should reflect the geometry of the first Brillioun zone projected along $< 0\bar{1}1 >$ direction. Figure 6.10 gives the comparison of the contour plot of the anisotropy spectrum with the $< 011 >$ section of the first Brillioun zone. The 2D-ACAR spectrum shown in figure 6.9 and the anisotropy spectrum shown in figure 6.10 are typical for the single crystals with diamond or zinc-blende lattice structure, for example, Ge, Si, GaAs and some other III-V compounds[174].

6.2.4 2D-ACAR Spectrum of GaAs with Photo-illumination

After the 2D-ACAR spectrum was taken in darkness, the LED was turned on to illuminate the GaAs sample and a spectrum was taken with the LED 'on' at ~ 30 K. At that temperature the energy of the emitted photons can be calculated using Eq.

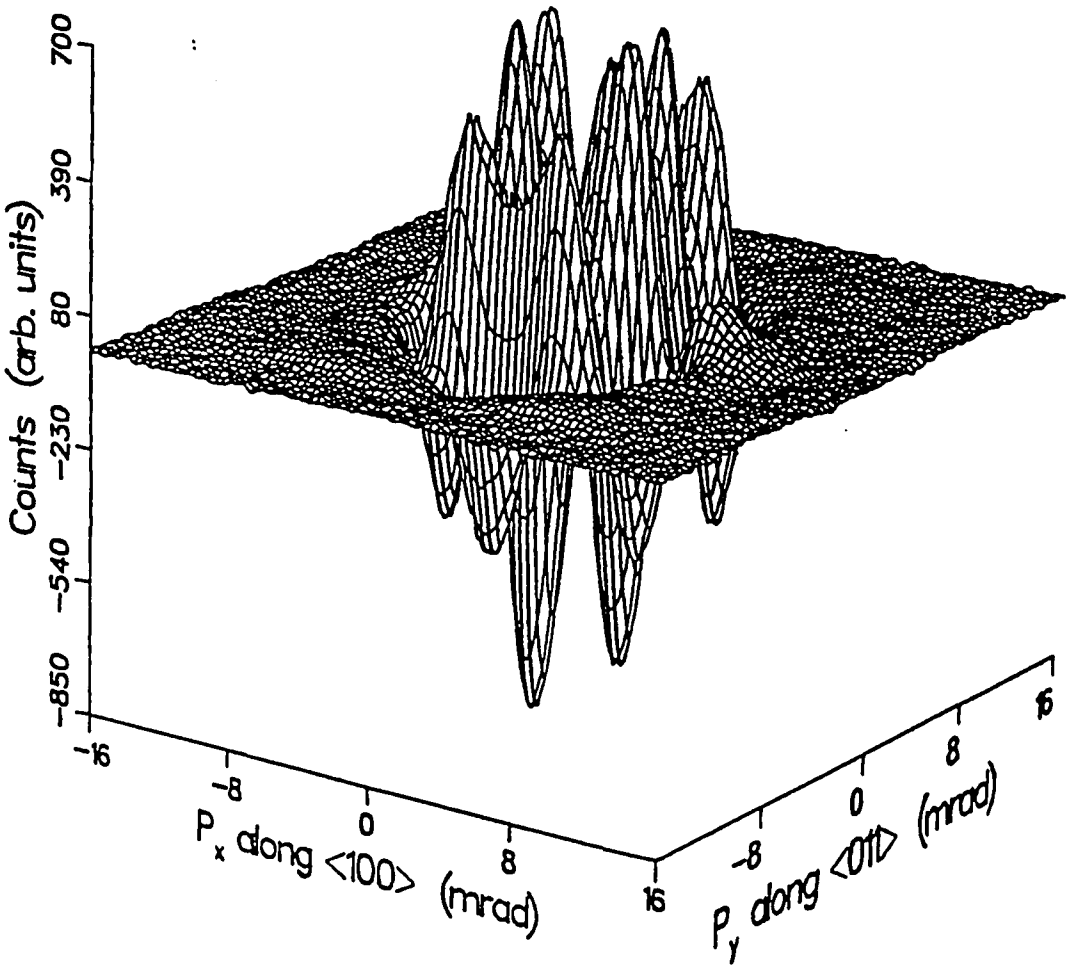

Figure 6.9: Anisotropy of GaAs bulk crystal after the subtraction of the isotropic component from the original 2D-ACAR spectrum shown in figure 6.8.

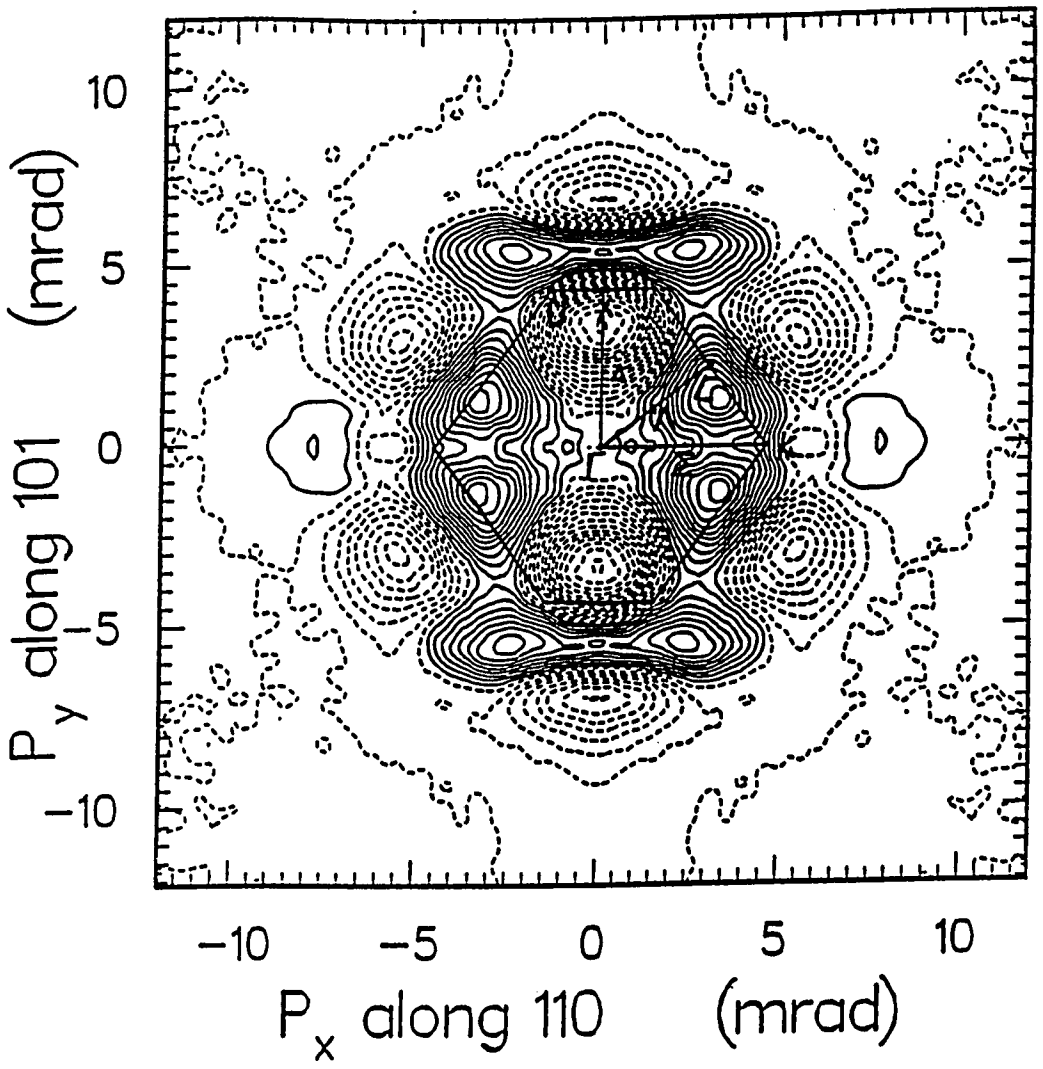

Figure 6.10: The comparison of the contour plot of the anisotropy spectrum with the < 011 > section of the first Brillioun zone.

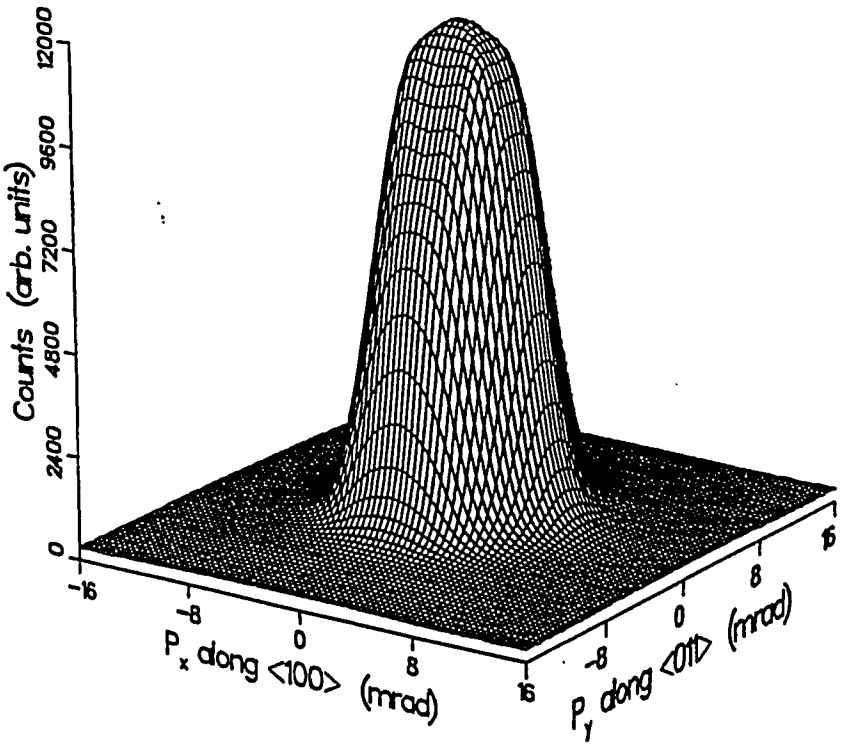

Figure 6.11: Positron 2D-ACAR spectrum of GaAs at low temperature with 1.42 eV photon illumination.

6.10, gives 1.42 ± 0.5 eV or the wavelength of 840 ± 50 nm. Figure 6.11 shows the 2D-ACAR spectrum of GaAs with photo-illumination. Here, the current through the LED is ~ 20 milli-amp (mA) which gives the total output power of ~3 milli-Watts (mW).

6.2.5 Difference between the Spectra with LED 'on' and with LED 'off'

Comparing the spectrum taken in darkness (figure 6.8) and the spectrum taken with photo-illumination (figure 6.11), it can be seen that there are some differences around the central region of the spectra. For the spectrum with LED 'on', there is a small

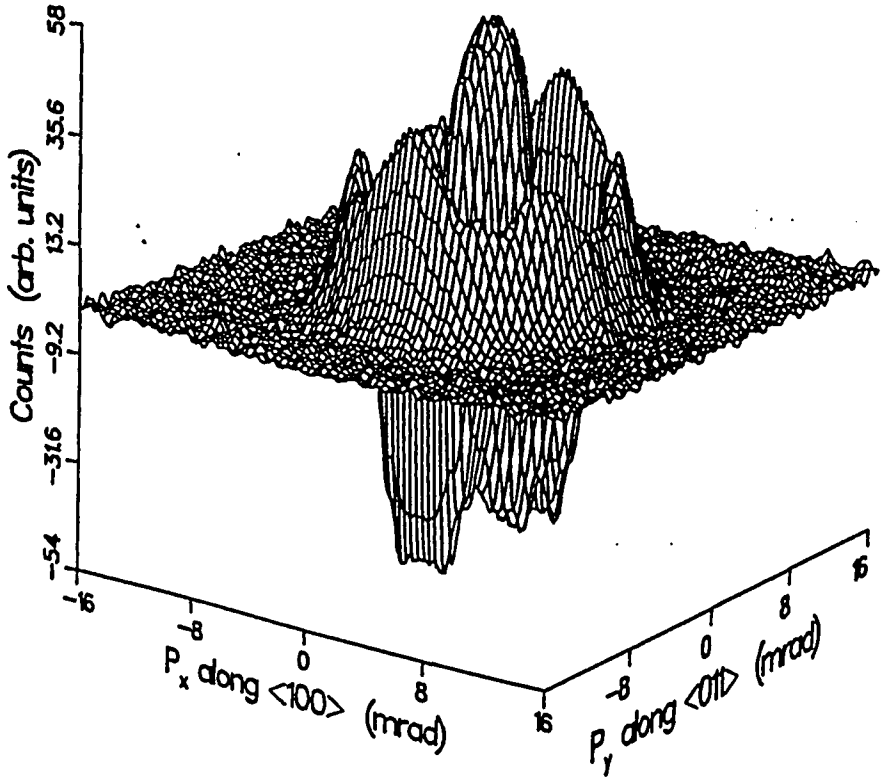

Figure 6.12: The difference spectrum, defined as the spectrum with photo-illumination minus the spectrum in darkness with the volume normalization of the two spectra.

sharp bump around the top of the spectrum while the top of the spectrum in darkness is quite flat. Figure 6.12 gives the difference spectrum which was defined as spectrum with LED 'on' minus the spectrum in darkness with the two spectra normalized to the same total counts (called volume normalization). It can be clearly seen that there is a central peak in the center of the difference spectrum, indicative of more positron annihilation with electrons of smaller momentum when the LED is 'on'. Here, when we take the difference, we make an assumption that the spectrum taken in darkness is a standard spectrum for a perfect GaAs single crystal. The validity of the assumption will be discussed later.

Then a series of spectrum was taken at same low temperature ($\sim$ 30 K) but with

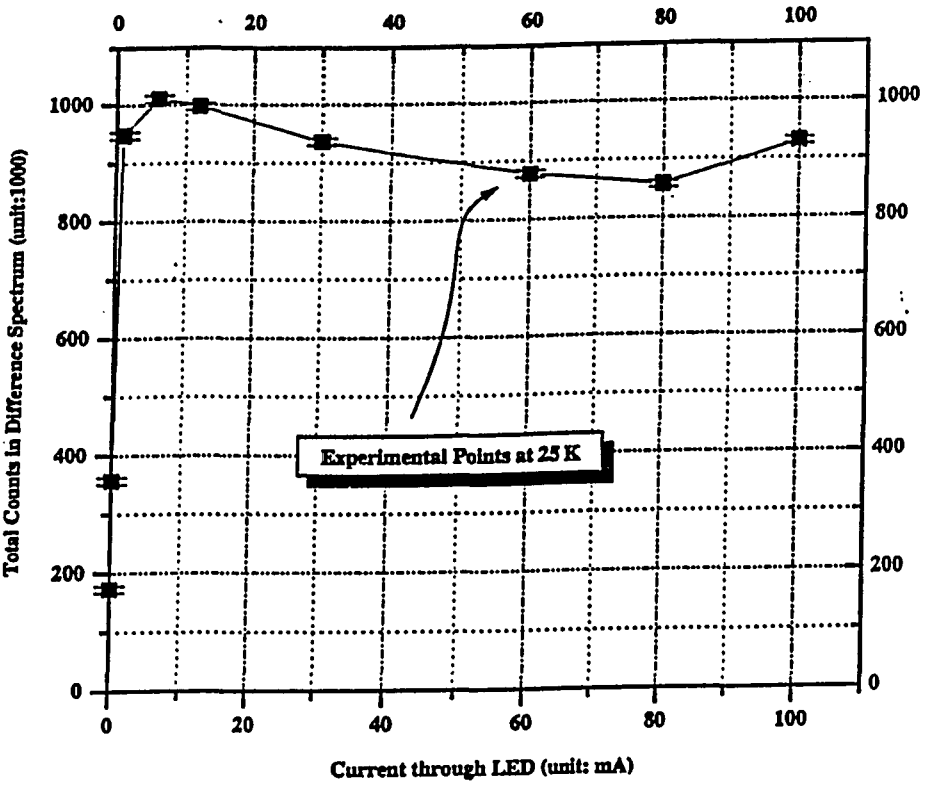

Figure 6.13: The change of the total counts in difference spectrum with the power of the LED (by change the current through the LED).

various light power (by changing the current through the LED). Figure 6.13 shows the total counts in difference spectrum vs current through the LED. From this figure, it can be seen that the curve (or the difference) saturates at the current above 6 mA. Here, the spectrum with LED 'on' means keep the LED 'on' during the data acquisition period. It was found that if we use the LED to illuminate the sample for a few hours and then start to taking data right after turning the LED off, the spectrum taken shows no difference from the spectrum taken without using the LED at all (the spectrum taken right after cooling down the sample). In other words, the effect of the LED is not durable.

To observe the temperature dependence of the difference spectrum, a series of

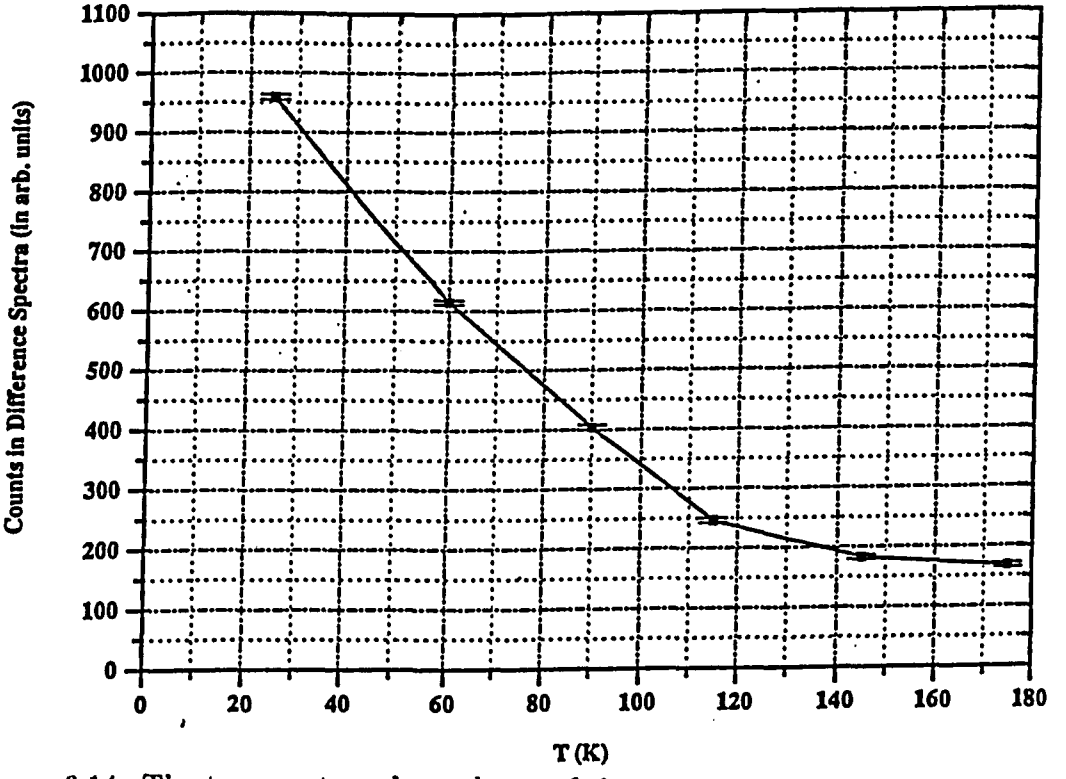

Figure 6.14: The temperature dependence of the total counts in difference spectrum

spectra was taken at different temperatures. At each temperature, two spectra, one with LED 'off' and another with LED 'on' were taken and then take the difference spectrum by volume normalization so that the effect of thermal expansion and contraction of the lattice on the 2D-ACAR spectrum can be minimized. It was seen that the overall shape of the difference spectrum at different temperature are similar but the total counts in the difference spectrum decrease with increasing temperature. Figure 6.14 shows the change of the total counts under the difference spectrum with temperature. From this figure, it can be seen that the difference between the spectrum with LED 'on' and the spectrum with LED 'off' disappeared at the temperature above 150 K.

The curve did not go to zero counts here because the absolute value was taken

when calculating the total counts. A similar phenomenon was observed earlier in semi-insulating GaAs by positron lifetime measurement[176] in which a light-pump of 1.42 eV photons was employed to illuminate the sample and the component of the longer lifetime which corresponded to positron trapping at vacancies disappeared at the temperature of $\sim 170K$. The vacancy was identified as negatively charged As vacancy (V_{As}^{-}) by using a monovacancy trapping model. From the conclusion of the positron lifetime results, we concluded that the difference between the 2D-ACAR spectrum with LED 'on' and LED 'off' was caused by positron trapping at As vacancies.

There is a reasonable explanation to above phenomena. As stated in section 4.2.2 that the Fermi-level of the semi-insulating GaAs will stay at midgap for the temperature range of 20 $\sim$ 300 K. The As vacancies are ionized and positively charge. Positrons will keep away from the positively charged region due to the Coulomb repulsion. Therefore, the positively charged As vacancies (V_{As}^{+}) can not trap positrons and have no effect on the 2D-ACAR spectrum. As we shine the light of proper wavelength or energy ($\sim$ 1.42 eV), those electrons at the top of the valence bands (see figure 6.6) will be excited to the energy levels of the As vacancy (+/0, 0/-). Thus, under the photo-excitation, the As vacancies become neutral or negatively charged and form positron traps. As a positron trapped into V_{As}, it will annihilate with the surrounding electrons. The electron(s) in the vacancy is relatively far away from the nucleus compared with those valence and core electrons (see the discussion about the radius of the 'orbit' of the electrons in defect level, which can be found in the standard solid state physics or semi-conductor physics [177, 178]. Therefore, they have smaller kinetic energy and momentum. The signal of positron annihilation with those electron will appear in the central region of the spectrum (small momentum

region) and thus we see a central peak when take the difference between the spectrum with LED 'on' and the spectrum with LED 'off'. Those electrons which are photo-excited to the vacancy levels prefer to 'jump' back to the valence bands to take lower energies. There is a balanced situation at which the density of electrons in the vacancy levels is constant and determined by the density of the vacancy levels, the trapping coefficient of the electrons to the vacancy, the electrons absorption cross section of the infrared light and the emission power of the LED.

By increasing the emission power (determined by the current through the LED), more electrons are populated to the vacancy level until reach the saturation situation at which the density of the electrons in the vacancy levels is independent of the light power. When the temperature of the sample is increased, the thermal motion of the electrons will be increased and the possibility of an electron to be excited to the conduction bands from the defect levels will increase. Up to some temperature, all the electrons photo-excited from the valence bands to the defect level will either jump back to the valence bands or be thermal-excited to the conduction bands nearby and there are no electrons left in the defects levels and positron will not become trapped anymore. Thus, there is no visible difference between the spectrum with LED 'off' and the spectrum with LED 'on' (for semi-insulating GaAs, this temperature is about 150 K $\sim$ 170 K) at higher temperature. The spontaneous electron emission rate is

$$g_e = c_e \gamma N_c(T) \exp\left(-\frac{E_d}{k_B T}\right) \tag{6.5}$$

where $c_e = \sigma_e v_e$ is the electron capture coefficient, v_e is the electron thermal velocity, γ is the degeneracy factor of the ionization level, $N_c(T)$ is the effective density of states of the conduction band, and E_d is the ionization energy to the conduction band [61]. By assuming that the concentration of V_{As}^- is controlled by the electron emission g_e from the ionization level and the optical transitions between the valence

bands and the vacancy level and further assuming that the electron capture cross section σ_e is independent of temperature, the fraction of negative vacancies can be written as

$$\frac{n_{V_{As}^-}}{n_{V_{As}}} = \frac{A}{[1 + \frac{Bv_e(T)N_c(T)}{\Phi} \exp(-\frac{E_d}{k_B T})]} \tag{6.6}$$

where A and B are constant and Φ is the photon flux. The expression is independent of the number of ionization levels in the band gap, and it assumes that the thermal electron emission occurs only from the highest level of the vacancy, V_{As}. In the simple case of one ionization level we have $A = \frac{\sigma_h^0}{\sigma_h^0 + \sigma_e^0}$ and $B = \frac{A\gamma\sigma_e}{\sigma_h^0}$, where σ_e^0 and σ_h^0 are the optical electron and hole generation cross sections of the ionization level, respectively.

It would have been possible if there were enough experimental points in the temperature-dependence curve shown in fig. 6.14 to fit the curve by Eq. 6.6 with the ionization energy E_d and constants A and B as free parameters. This was not applicable in our case because each point on the curve need two days of data acquisition time. While the fitting was done for the similar curve from lifetime measurement[176], giving the ionization level $E_d \approx 50$ meV.

It is obvious that we over-estimated the contribution of delocalized positron in the spectrum with LED 'on' when we take the difference spectrum described above because the volume of the bulk spectrum (the spectrum with LED 'off') was normalized to the same volume of the spectrum with LED 'on'. If we denote the 2D-ACAR spectrum for bulk GaAs as $N_{bulk}(p_x, p_y)$ and the spectrum for positron annihilation at As vacancies as $N_{vacancy}(p_x, p_y)$, the spectrum with LED 'on', denoted as $N_{LED}(p_x, p_y)$, should be

$$N_{LED}(p_x, p_y) = x \times N_{vacancy}(p_x, p_y) + (1 - x) \times N_{bulk}(p_x, p_y) \tag{6.7}$$

where x is the fraction of positron trapping and annihilation at the As vacancy and

ranged from 0 to 1.0. This fraction can be determined from positron lifetime measurement by comparing the relative intensities of different lifetime components[179, 180, 181]. Indeed, positron lifetime measurements combined with 2D-ACAR measurements[45] had been done at about the same time as this experiment, in which two identical Si-doped GaAs were used to study the Ga and As vacancies and the fraction of positron trapping in As and Ga vacancies had been obtained from the lifetime spectrum. In our experiment, we developed a new method to determine the fraction, x, of positron trapping at As vacancies. The spectrum with LED 'on' consists of two parts: localized positron (trapped into V_{As}) annihilation with the electrons in the vacancy which gives the defect spectrum and the delocalized positron annihilation with valence electrons or core electrons. As the positron get trapped in the vacancy, the wavefunction overlap with core electron wavefunction or valence electron wavefunction should be very small and be negligible because of larger distance from the nucleus than in the interstitial space. Therefore, the contribution from core annihilation in the spectrum with LED 'on' will simply come from the delocalized positron annihilation.

We use positron annihilation with core electron as a key factor. As positrons annihilate with core electrons, the spectrum will be rotational symmetric in the (p_x, p_y) plane due to the average of the orientation of the electron orbitals and the spectrum will be very broad due to the large momentum of the core electrons, and the resultant spectrum for core annihilation can be assumed to be a rotational Gaussian shape. Therefore, the large momentum part in the spectrum can be used to characterize the core annihilation. We made a gaussian fit to the outer skirt of the bulk spectrum (the spectrum with LED 'off') and the spectrum with LED 'on'; then calculate the total counts under each rotational Gaussian shape, denoted as A_{bulk} and A_{light}, and

take the ratio of the counts,

$$R = \frac{A_{light}}{A_{bulk}} \tag{6.8}$$

Then we change the number of points from which the gaussian fit was made to the outer skirt of the spectrum, the ratio, R, becomes smaller and consistently converges to a value of 90%. It means that 90% of the positrons entered the sample still keep delocalized when the LED was 'on' (while in the darkness, 100% of the positrons would be in the delocalized states) and 10% of positrons were trapped in the As vacancies. Thus, the bulk spectrum should be normalized to 90% of the volume of the spectrum with LED 'on' in the subtraction and the residue spectrum is the defects spectrum. Figure 6.15 shows the defects spectrum after the bulk spectrum were subtracted from the spectrum with LED 'on'. As the positron lifetime in the bulk GaAs was well measured, being 228 ps at 20 K, and the fraction of positron trapping at As vacancies is 10% from above discussion, it is possible to estimate the concentration of the defects by using the so-called one-defect trapping model discussed in section 1.8. From Eq. 1.22, it can be calculated that positron trapping rate, $\kappa \sim 5 \times 10^8/sec.$ Positron trapping coefficient, μ, had been estimated to be $\sim 1.5 \times 10^{16}/sec.$ The atomic density of As sublattice in GaAs is $\sim 2 \times 10^{22}/cm^3$. Thus, a concentration of V_{As}^- of $\sim 1 \times 10^{15}/cm^3$ can be calculated using Eq. 1.18. Similar result on the concentration of the vacancies had been reported from the positron lifetime measurement[176].

In optical experiments on bulk GaAs, a strong absorption of monochromatic light within 50 meV of the conduction band edge is observed below 150 K[182, 183]. This near-band-edge absorption has been attributed to an unidentified point defect center, but it is not associated to the EL2 defects[182]. From positron annihilation experiment, as we discussed above, As vacancies has an ionization level situated close to the conduction band at $\sim E_c - 50meV$ and further this level can be effectively populated

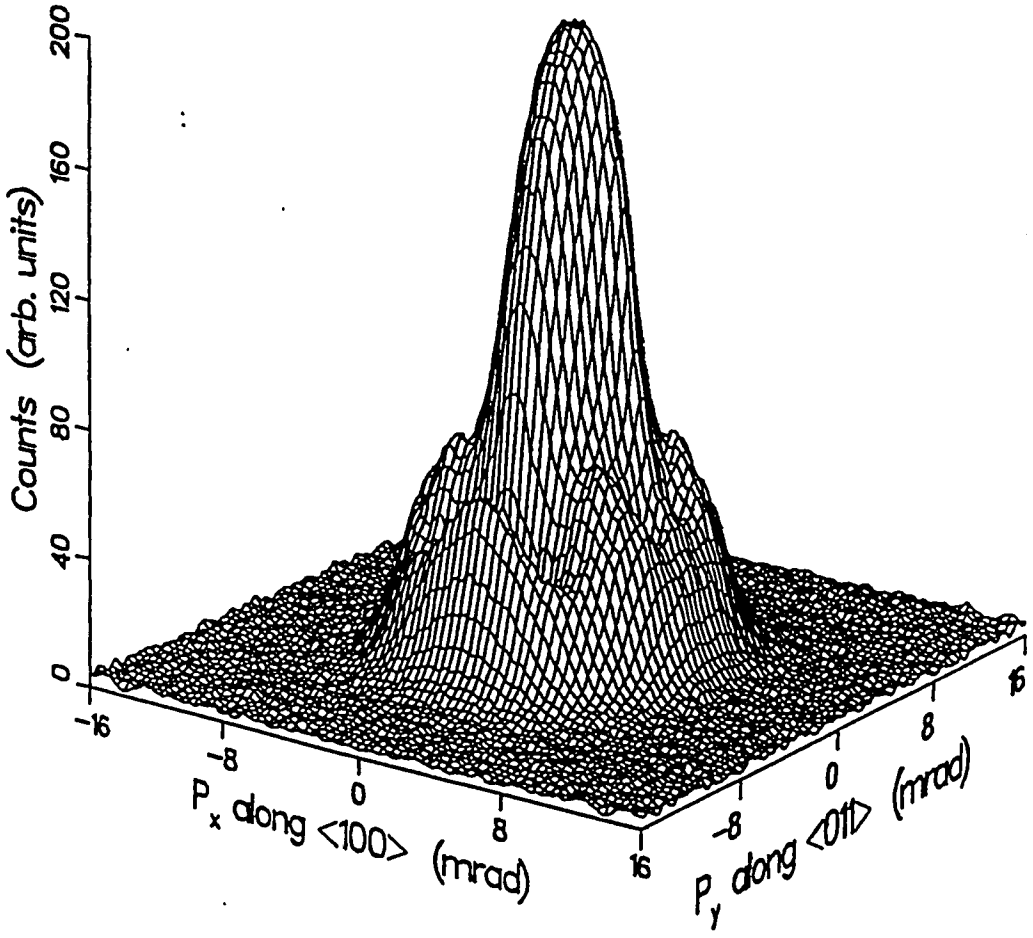

Figure 6.15: The defects spectrum– after 90% subtraction of the bulk spectrum from the spectrum with LED 'on'.

using 1.4 $\sim$ 1.5 eV light. Thus, the result from positron annihilation indicates that the near-band-edge absorption results from the photoinduced electron transition from the valence band to the ionization level of the arsenic vacancy.

6.2.6 The Effect of Other Defects on the Spectrum with LED 'on'

In above discussion, we didn't mention the effect of other defects in the semi-insulating GaAs. Some of them may have contribution to the defects spectrum obtained above. In particular, the Ga vacancy and the famous EL2 defects are also positron traps. Shining the infrared light onto the sample will excited some electrons from the top of the valence bands to the V_{As} level and move the Fermi level towards the conduction band a little. The charge status of the V_{Ga} levels which stay below the Fermi level keep unchanged with or without photo-illumination. Thus, V_{Ga} makes no contribution to the defects spectrum. Generally speaking, neither the interstitials nor antisites defects make any contribution to the defects spectrum due to the same reason as for the Ga vacancy. For the EL2 defects, we can not make similar statement as above because there is a EL2 metastable state after a 1060 nm wavelength infrared light illumination at the temperature below 120 K[70, 184, 185, 186] and there exist vacancies in the EL2 metastable state, EL2*, from positron lifetime measurement [181] on the EL2 defects in semi-insulating GaAs. In the emission spectrum of the LED used in the experiment there is really a small overlap in the long wavelength tail with the EL2 absorption peak (1060 nm). But based on the fact that there is no any observable difference between the spectrum without photo-illumination and the spectrum taken with LED 'off' but after a few hours of illumination, we can claim that there is no significant contribution in the defects spectrum from the EL2 defects. This is why we

can assume that the spectrum taken in darkness is the bulk (single crystal) spectrum.

6.2.7 Comparing the Experimental Result with the Theoretical Calculations

There had been some theoretical calculations on the electron and positron status at the vacancy defects in GaAs[187, 188, 189]. Although the earlier calculations emphasized on the momentum density distribution of $e^+ - e^-$ pair in GaAs[189], the discussion of the anisotropy for positron 2D-ACAR in bulk GaAs spectrum had been given by Panda[190] and Saito *et al*[191] recently, based on group theory. The first self-consistent calculation of positron annihilation characteristics for bulk GaAs and for positron trapping at the V_{As}^- which include positron interaction with the surrounding lattice has been performed recently by Gilgien *et al*[192], using the two-component density-functional theory within the Car-Parrinello approach. Figure 6.16 gives the comparison of our experimental data in bulk Si (spectrum with LED 'off') with the calculated 2D-ACAR spectrum. From this figure, it can be seen that the agreement between the theory and the experimental data is very good, the bone shape structure in the central region of the experimental data was well reproduced by the theory. While figure 6.17 gives the comparison of our defects 2D-ACAR spectrum ($N_{0.9}(p_x, p_y)$) with calculated 2D-ACAR data for positron trapping at the V_{As}^-. The agreement between the theory and the experimental data for positron trapping at defects is reasonably good (in fact, it is very good from the point of view of the reproduction of the diamond shape in the center of both spectrum, which is the major point of our concern) except the small difference in the outer region which may come from the positron annihilation with other defects in the experimental spectrum and calculation cannot take this into account within a simple model. In the calculation,

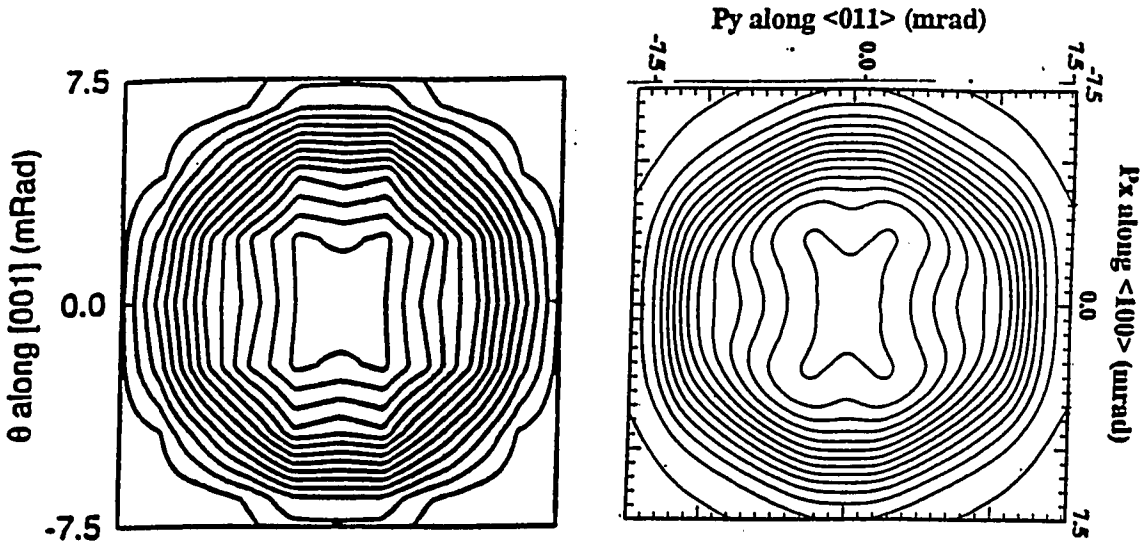

Figure 6.16: The comparison of the experimental data of bulk silicon with theoretical calculation from Gilgien *et al*[192].

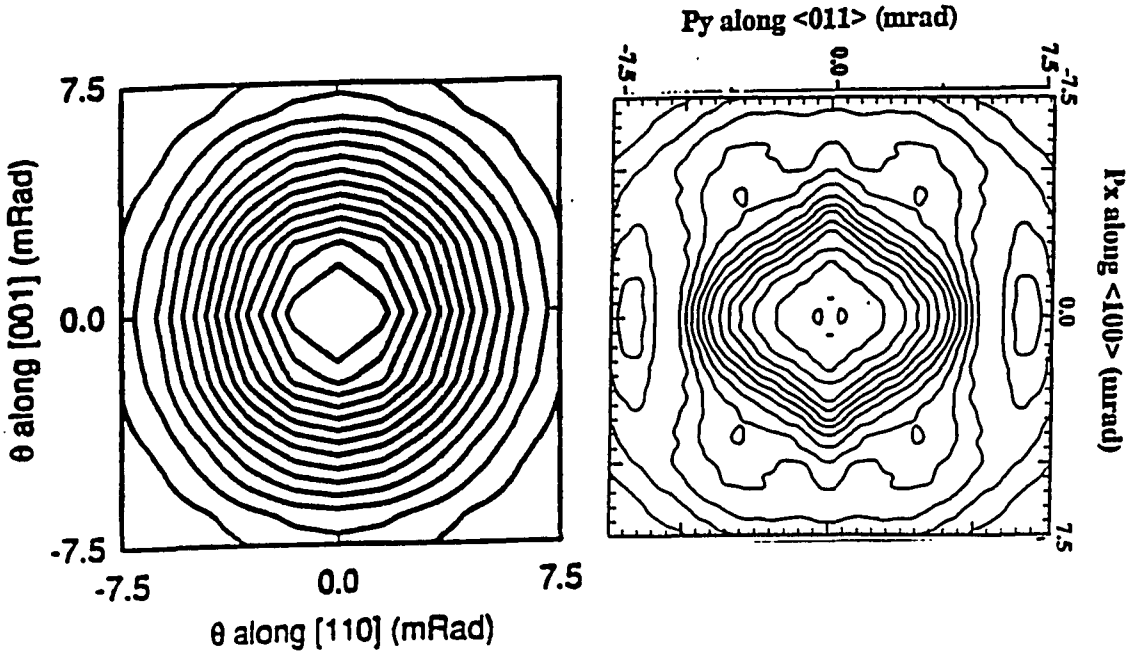

Figure 6.17: Comparison of experimental data with the theoretical calculation (from Gilgien *et al*[192])-positron trapping at negative As vacancies.

a superlattice with 128 atoms has been used to simulated the periodic potential of GaAs lattice and the positron wavefunction in this superlattice was calculated. The As vacancy was produced by taking out an As atom from the superlattice and put an electron and an positron into the vacancy, leaving the wavefunctions of electron and positron self-adjusted and the lattice fully relaxed. It was found that the original symmetry of the vacancy, T_d, was lowered to D_{2d}, due to the interaction between the trapped positron and the surrounding relaxed Ga (nearest neighbors) and As (second nearest neighbors) atoms, and upon the localization of positron, two minima in the total energy were found corresponding to C_{2v} and C_s configurations separated by a maximum barrier height of 0.03 eV. The lowering of the lattice symmetry caused by positron trapping into vacancy was demonstrated by the fact that there is only a two-fold symmetry in 2D-ACAR spectrum which is the lowest symmetry required by the time-reversal symmetry. Although the phenomenon of lattice relaxation caused by positron trapping into vacancy had been discussed earlier by Laasonen *et al*[189] theoretically, this is the first time for the experiment result to show this effect by comparing with theory. In this experiment, we were not able to separate the spectrum of positron trapping at the negative As vacancies from that of positron trapping at the neutral As vacancies (V_{As}^0) due to the limited resolution on the wavelength of the infrared light (the energy spread of the emitted photons from the LED). A similar experiment was done by Ambigapathy *et al*[45] recently by investigating different GaAs samples with known existence of V_{As}^0 and V_{As}^-, respectively (without *in situ* photo-illumination). The spectra for positron annihilation with V_{As}^0 and V_{As}^- were taken separately and the difference between the two spectra reflects the distortion of the motion of the atoms around the vacancy by the positron and the trapped electron.

Chapter 7

Summary and Future Work

The development of high-intensity monoenergetic slow positron beam at Brookhaven National Laboratory makes it possible to use positron 2D-ACAR technique, a well established one and has shown its great capability in the investigation of Fermi surface for metals and high-T_c superconductors in the last decade, to do the depth-resolve study on multilayer systems. As the first 2D-ACAR experiment on interface studies, we choose the well studied but not well understood SiO_2-Si buried interface as the testing target. With the variation of positron beam energy, positrons can be implanted to different layers of the system and the status of positron annihilation at each layer was revealed by 2D-ACAR spectra. In oxide region, a sharp central peak appeared in the fine structure spectrum, indicating positronium (Ps) atoms formation and trapping in microvoids. The discovery of the existence of microvoids in oxide region is coincident with the conclusion from TEM measurement[193] and a recent result of ellipsometry measurement[194]. A model of a spherical-well potential was used to simulate the Ps atoms trapping in microvoids from which the relation between the size of the microvoids and the width (or FWHM) of the Ps signal in

2D-ACAR spectrum was derived. The estimated size of $\sim 10\mathring{A}$ of the microvoids is in a very good agreement with the TEM result[193]. Further, the concentration of the microvoids was estimated using the positron trapping model for monovacancies, with the assumption of the positron trapping coefficient. Similarly, the sharp peak was observed in the center of 2D-ACAR spectrum of interface region, which was attributed to the Ps atoms formation and trapping in microvoids at that region. The size and the concentration of the microvoids were estimated using above models. This discovery is very important because it is beyond our current understanding of the interface structure. Although there is no evidence of the electrical activity of the microvoids, i.e., they may not form electron traps in the interface region, the existence of the microvoids with that size ($\sim 10\mathring{A}$) and that concentration ($10^8 \sim 10^9/cm^2$) may have some important impact on the fabrication of the next generation electronic devices. First of all, the existence of the microvoids in the interface region may cause the electric field breakdown when the oxide layer becomes thinner as required by modern technology. Second, the stress cause by the mismatch between the Si single crystal and the amorphous SiO_2 due to the existence of the microvoids may cause the oxide layer falling off the Si surface when the size of the devices shrinks into submicron scale which is the trend of the Si industry. The samples from IBM Inc. with thicker oxide ($\sim 1170\mathring{A}$) were the best (state-of-the-art) samples available for the last generation ($7 \sim 8$ years ago) and were used in the electronics. And the existence of the microvoids in oxide and interface regions was further confirmed by the investigation on the p-type SiO_2-Si sample and n-type MOS sample. Thus, our result is not only valid for a specific sample but also valid for a series of representative samples. To make the measurement systematic, we studied a p-type SiO_2-Si sample from AT&T Bell Laboratories with thinner oxide ($\sim 150\mathring{A}$) which is the state-of-the-art sample

available currently. The result is consistent with that from thicker oxide samples: A sharp central peak was observed in the interface spectrum, indicating that the Ps atoms formation and trapping in microvoids in the interface region, although the size and concentration of the microvoids were not estimated due to the lack of the information of positron annihilation fractions. Therefore, our conclusion of the existence of the microvoids in the SiO_2-Si region is generally valid and it has not been observed by any other techniques.

Besides, we attributed the small bumps around the Ps peak in the fine structure spectrum of the interface region to positron annihilation with the unpaired electrons in the interface region–the famous P_b centers, from the point of view of the position and the symmetry of the fine structures. Positron annihilation at the P_b centers has been inferred from positron S-parameter measurements before[51], by observing the variation in the S-parameter with annealing and hydrogen passivation which produce the well-known changes in the electrical activity of the P_b centers. Although positron 2D-ACAR coupled with a high-intensity positron beam is a promising microscopic probe for the surface and interface studies, its application is limited by the difficulties of interpretating the data due to the lack of theoretical calculation. Several theorists have shown their interests in calculating positron annihilation in the SiO_2-Si interface, but no satisfied result comes out yet because of the difficulties of selecting an appropriate interface model. The way we estimated the concentration of the defects in the interface region may not appropriate because the positron trapping model is only valid for one dimensional distribution of the defects (in the bulk) , but the interface is a two-dimensional issue. As the first 2D-ACAR study of the interface, the lack of theoretical support in data analysis is possible. Our work should be able to motivate some theoretical work.

Also, using the conventional 2D-ACAR setup coupled with *in situ* photo-excitation, we studied the As vacancies in semi-insulating GaAs. From the symmetry of the defect spectrum, it was found that the original atomic configuration of the vacancy defect changes when a positron became trapped in the defects, due to the interaction of the trapped positron with the atoms surrounding the vacancy. Therefore, a theoretical calculation has to take this interaction into account when dealing with the problem of positron trapping in defects. The concentration of the defects of $\sim 10^{15}/cm^3$ estimated from the 2D-ACAR spectrum reflects the sensitivity of positron annihilation to the relative concentration of the defects ($\sim$ 0.1 ppm), about an order of magnitude better than that of other techniques. The very good agreement between experimental data and theoretical calculation (the first self-consistent calculation which takes the interaction of positron with the surrounding atoms into account) for both bulk and defect spectra indicate that positron 2D-ACAR spectrum can be used as the fingerprint of a specific defects. Also, positron 2D-ACAR plus *in situ* photo-illumination may represent another new direction of applying positron annihilation (PA) technique in the investigation of defects in semiconductors. The major advantage of the *in situ* illumination is to eliminate any artifacts during the comparison of the spectrum without defects and the one with defects, as the properties of the samples may be different even they are claimed to be identical.

Above, we have summarized our current work on positron 2D-ACAR investigation of SiO_2-Si interface using a high intensity beam and of point defects in SI-GaAs using conventional setup plus photo-illumination. Both experiments shed new light on the application of this technique in condensed matter. There is a major limitation on the application of both setups (conventional and beam 2D-ACAR). This limitation is the lack of theoretical support in the data analysis, which makes the current or past

2D-ACAR result stayed more or less at the qualitative instead of quantitative level. For the beam 2D-ACAR, another limiting factor is the beam intensity, which restricts the sample-detector distance and the resolution of the system. Under current beam intensity, there are still some work we can do in the near future: study the famous EL2 defects in GaAs and the DX centers[195] in $AL_{1-x}Ga_xAs$ ($x \geq 0.22$), which will require the cooling capability of the interface chamber. In fact, EL2 defects exist in the bulk, therefore, employing the bulk chamber should be the right choice. From our past experiment, even with the photo-illumination with the right wavelength photons ($\sim$1060 nm, under which EL2 transfers to its metastable state EL2* at the temperature below 120 K), there was no difference between the spectrum of its normal states and the spectrum of its metastable states (There is a monovacancy associated with the metastable state, observed from positron lifetime measurement[181]) using the conventional 2D-ACAR setup, which was attributed to the ionization of the defects by the high energy positron from the radioactive source (^{22}Na). While, using the interface chamber, we can avoid this ionization problem by adjusting the beam energy (to a few keV). To study the DX centers, the positron beam is necessary because the thickness of the layer of $Al_{1-x}Ga_xAs$ is only a few microns on the surface of GaAs substrate. By applying *in situ* photo-illumination (with the right wavelength), we should be able to see the difference between the spectrum of its normal states and metastable states (similarly, a monovacancy associated with its normal states had been observed by positron Doppler broadening measurement[196].).

It is planned to use the beamline chamber to study high-T_c superconductor thin film. Positron 2D-ACAR study of superconductors, examining the Fermi surface, has been an active field of research for a few years using conventional 2D-ACAR setup. But the experiments were limited to those few materials in which bulk sample

with a reasonable dimension were available[42]. Generally, it is much easier to grow thin film superconductors with high quality (crystal) and larger size than to grow bulk superconductors. Because of the nature of the Fermi surface in superconductors (usually a small pocket) a very good angular resolution of the system is required (to about 0.3X0.3 $mrad^2$), which will require higher beam intensity to compensate for the longer sample-detector distance (to $\sim 3 \times 10^8 e^+/sec$). The work in developing a higher intensity positron beam is in progress now. It is feasible to reach the intensity of $\sim 2 \times 10^8 e^+/sec$ in the near future by a better control of the Cu evaporation and Kr injection (moderator), or by introducing a larger Cu source and larger source holder with some focusing mechanism. The major problem in developing a high intensity positron beam is the efficiency of the moderators. The highest efficiency reported is $\sim$ 1% for rare gas moderator. Another potential moderation mechanism is the so-called 'field-enhanced' moderation, originated by Lynn *et al*[15] and later reviewed by Beling *et al*[197]. The basic idea is to increase the diffusion of the thermalized positrons to the surface by applying an electric field across the moderator (It is limited to semiconductors or insulators). The research on developing an GaAs moderator with a thin layer of Au on the surface is still going on. A moderator efficiency of $\sim$ 10% is expected (and possible).

For the bulk chamber, the most possible further experiments in the near future is to investigate all the possible defect level in the upper half of the bandgap of of GaAs, by employing the *in situ* photo-illumination with a monochromator.

Bibliography

[1] P. A. M. Dirac, *Proc. Cambridge Philos. Soc.*, **26**, 361(1930).

[2] C. D. Anderson, Science, **76**, 238(1932).

[3] R. Beringer and C. G. Montgomery, Phys. Rev., **61**, 222(1942).

[4] S. Debenedetti, C. E. Cowan, and W. R. Konnecker, Phys. Rev., **76**, 440(1949).

[5] P. E. Mijnarends, 'Electron Momentum Densities in Metal and Alloys' in *Positron in Solids*, edited by P. Hautojärvi, (Springer-Verlag, 1979).

[6] S. Berko, 'Momentum Density and Fermi-Surface Measurements in Metals by Positron Annihilation' in *Positron Solid State Physics*, edited by W. Brandt and A. Dupasquier, (North-Holland, New York 1983).

[7] P. E. Mijnarends and A. Bansil, 'Theory of electron and positron momentum distributions in solids' in *Positron Spectroscopy of Solids*, edited by A. Dupasquier and A. P. Mills jr., page 25, (IOS Press, Amsterdam 1995).

[8] R. N. West, 'Positron studies of the Electronic Structure of Solids', in ref.[7], page 75.

[9] S. Berko, M. Haghgooie, and J. J. Mader, Phys. Lett. A **63**, 335(1977).

[10] A. A. Manuel, S. Samoilov, O. Fischer and M. Peter, Helv. Phys. Acta., **52**, 255(1979).

[11] R. N. West, J. Mayers, and P. A. Walters, J. Phys., **14** , 478(1981).

[12] R. N. West, *Positron Studies of Condensed Matter*, (Taylors & Francis, 1974).

[13] L. Madanski and F. Rasetti, Phys. Rev., **79**, 397(1950).

[14] K. F. Canter, A. P. Mills, Jr., and S. Berko, Phys. Rev. Lett., **33**, 7(1974).

[15] K. G. Lynn and B. T. A. Mckee, Appl. Phys., **19**, 247(1979).

[16] J. M. Dale, L. D. Hulett, and S. Pendyala, Surf. Interface Anal., **2**, 199(1980).

[17] P. G. Coleman, J. D. McNutt, J. T. Hutton, L. M. Diana, and J. L. Fry, Rev. Sci. Instrum., **51**.

[18] R. H. Howell, P. Meyer, I. J. Rosenberg, and M. J. Fluss, Phys. Rev. Lett., **54**, 1698(1985).

[19] K. G. Lynn, A. P. Mills, Jr, R. N. West, S. Berko, K. F. Canter , and L. O. Roellig, Phys. Rev. Lett., **54**, 1702(1985).

[20] D. M. Chen, 'A 2D-ACAR Study of Positron Interactions with Surfaces of Aluminum and Silicon', a Ph.D thesis, City University of New York, 1987.

[21] D. M. Chen, S. Berko, K. F. Canter, K. G. Lynn, A. P. Mills jr., L. O. Roellig, P. Sferlazzo, M. Weinert, and R. N. West, Phys. Rev. B **39**, 3966(1989).

[22] A. Perkins and J. P. Carbotte, Phys. Rev. B **1**, 101(1970).

[23] R. M. Nieminen and J. Oliva, Phys. Rev. B **22**, 2226(1980).

[24] P. Kubica and A. T. Stewart, Can. J. Phys., **61**, 971(1983).

[25] H. H. Jorch, K. G. Lynn, and T. McMullen, Phys. Rev. B **30**, 93(1984).

[26] T. Hyodo, T. McMullen, and A. T. Stewart, Phys. Rev. B **33**, 3050(1986).

[27] M. J. Puska and R. M. Nieminen, Rev. Mod. Phys., **66**, 841(1994).

[28] W. Brandt and R. Paulin, Phys. Rev. B **15**, 2511(1977).

[29] R. Paulin, in the Proceedings of the V International Conference on Positron Annihilation, edited by R. Hasiguti and K. Fujiwara, Page 601, (Sendai, 1979).

[30] A. F. Makhov, Sov. Phys. Solid State, **2**, 1934(1960).

[31] A. F. Makhov, Sov. Phys. Solid State, **2**, 1942(1960).

[32] A. F. Makhov, Sov. Phys. Solid State, **2**, 1945(1960).

[33] A. Vehanen, K. Saarinen, P. Hautojärvi, and H. Huomo, Phys. Rev. B **35**, 4606(1987).

[34] A. P. Mills, Jr. and R. Wilson, Phys. Rev. A **26**, 490(1982).

[35] K. G. Lynn and H. Lutz, Phys. Rev. B **22**, 4143(1980).

[36] A. I. Akhiezer and V. B. Berestetskii, *Quantum Electrodynamics*, (Interscience, New York 1965).

[37] V. B. Berestetskii, E. M. Lifshitz, and L. P. Pitaevskii, *Relativistic Quantum Theory*, (Pergamon, Oxford 1971).

[38] V. I. Goldanskii, Rev. Atom. Energy, **6**, 3(1968).

[39] M. Bertolaccini, A. Bisi, G. Gambarini, and L. Zappa, J. Phys. C **4**, 734(1971).

[40] W. Brandt, Appl. Phys., **5**, 1(1974).

[41] S. Tanigawa, Y. Mizuhara, T. Kurihara, M. Osawa, Y. Hidaka, M. Oda, Y. Enomoto, M. Suzuki, and T. Murakami, in the Proceedings fo the 8th International Conference on Positron Annihilation, page 933, (World Scientific-Singapore, 1988).

[42] L. P. Chan, 'Positron 2D-ACAR Study of High-T_c Superconductors', a Ph.D thesis, State University of New York at Stony Brook, 1993.

[43] Y. J. He, M. Hasegawa, R. Lee, S. Berko, A. Adler, and A. L. Jung, Phys. Rev. B **33**, 5924(1986).

[44] J. P. Peng, K. G. Lynn, M. T. Umlor, D. J. Keeble, and D. R. Harshman, Phys. Rev. B **50**, 11247(1994).

[45] R. Ambigapathy, A. A. Manuel, P. Hautojärvi, K. Saarinen, and C. Corbel, Phys. Rev. B **50**, 2188(1994).

[46] M. Alatalo, H. Kauppinen, K. Saarinen, M. J. Puska, J. Mäkinen, P. Hautojärvi, R. M. Nieminen, Phys. Rev. B **51**, 4176(1995).

[47] S. Szpala, P. Asoka-Kumar, B. Nielsen, J. P. Peng, S. Hayakawa, K. G. Lynn, and H. -J. Gossmann, to be published in Phys. Rev. B.

[48] K. G. Lynn and A. N. Goland, Sol. State Comm. **18**, 1549(1976).

[49] A. van Veen, H. Schut, J. de Vries, R. A. Hakvoort, and M.R. IJpma, in *AIP conference Proceedings 218, Positron Beams for Solids and Surfaces*, edited by P. J. Schultz, G. R. Massoumi, and P. J. Simpson, 171(1990).

[50] T. C. Leung, 'Study of Si/Si, Si/SiO_2, and Metal-Oxide-Semiconductor (MOS) Using Positrons', a Ph.D Thsis, State University of New York at Stony Brook, 1991.

[51] P. Asoka-Kumar, K. G. Lynn, and D. O. Welch, J. Appl. Phys., **76(9)**, 4935(1994).

[52] P. R. Wallace, Solid St. Phys., **10** 1(1960).

[53] A. Ore, Univ. Bergen Aarbook, Naturvidenskap, Rekke 9(1949).

[54] A. Bisi, A. Dupasquier, and L. Zappa, in the Proceedings of Second International Conference on Positron Annihilation, 1971, Kingston, Ontario, unpublished, page 2.21.

[55] R. A. Ferrell, Rev. Mod. Phys., **28**, 308(1956).

[56] W. Brandt, G. Coussot, and R. Paulin, Phys. Rev. Lett., **23**, 522(1969).

[57] A. Greenberger, A. P. Mills, Jr. A. Thompson, and S. Berko, Phys. Lett. A **32**, 72(1970).

[58] A. P. Mills, Jr., 'Experimentation with Low-Energy Positron Beams', in *Positron Solid State Physics*, edited by W. Brandt and A. Dupasquier, (North-Holland, New York 1983).

[59] K. G. Lynn, 'Slow Positrons in the Study of Surface and Near-Surface Defects', in *Positron Solid State Physics*, edited by W. Brandt and A. Dupasquier, (North-Holland, New York 1983).

[60] M. Lannoo and J. Bourgoin, *Point Defects in Semiconductors* I, Theoretical Aspects, (Springer-Verlag, 1981).

[61] J. Bourgoin and M. Lannoo, *Point Defects in Semiconductors* II, Experimental Aspects, (Springer, 1983).

[62] M. J. Puska, C. Corbel, and R. M. Nieminen, Phys. Rev. Lett., **41**, 10632(1990).

[63] R. P. Gupta and R. W. Siegel, J. Phys. F **10**, L7(1980).

[64] A. M. Ashcroft and N. D. Mermin, *Solid State Physics* Chapter 14, (Holt, Rinehart, and Winston, Philadelphia 1976).

[65] R. J. Weiss, W. A. Reed and P. Pattison, in *Compton Scattering*, edited by B. Williams, page 43, (London, 1977).

[66] P. Platzman and N. Tzoar, in ref[65], page 28.

[67] G. Lancaster, *Electron Spin Resonance in Semiconductors*, (Plenum, New York 1967).

[68] A. Abragam and B. Bleaney, *Resonance paramagnetique Electronique des Ions de Transition*, Presses Universitaires de France, Paris, 1971.

[69] C. P. Schlichter, *Principles of Magnetic Resonance*, volume 1, second edition, (Springer, New York 1980).

[70] J. C. Bourgoin, H. J. von Bardeleben, and D. Stiévenard, J. Appl. Phys., **64**, R65(1988).

[71] R. Rochet, S. Rigo, M. Fromet, C. d'Anterroches, C. Maillot, H. Roulet, and G. Dufour, Adv. Phys., **35**, 237(1986).

[72] S. K. Sinha, E. B. Sirota, and S. Garoff, Phys. Rev. B **38**, 2297(1988).

[73] P. H. Fuoss, L. J. Norton, S. Brennan, and A. Fischer-Colbrie, Phys. Rev. Lett., **60**, 600(1988).

[74] F. Sette, G. Ruocco, M. Krisch, U. Bergmann, C. Masciovecchio, V. Mazzacurati, G. Signorelli, and R. Verbeni, Phys. Rev. Lett., **75**, 850(1995).

[75] M. H. Weber, 'Positronium Reflection', a Ph.D thesis, City University of New York, 1989.

[76] P. J. Schultz and K. G. Lynn, Rev. Mod. Phys., **60**, 701(1988).

[77] D. E. Groce, D. G. Costello, J. W. McGowan, and D. F. Hering, Bull. Am. Phys. Soc., **13**, 1397(1968).

[78] D. G. Costello, D. E. Groce, D. F. Hering, and J. W. McGowan, Phys. Rev. B **3**, 1433(1972).

[79] A. P. Mills, Jr. and E. M. Gullikson, Appl. Phys. Lett., **49**, 1121(1986).

[80] R. Khatri, M. Charlton, P. Sferlazzo, K. G. Lynn, A. P. Mills, Jr., and L. O. Roellig, Appl. Phys. Lett., **57**, 2374(1990).

[81] See for example in ref [64], page 270.

[82] General Electric Medical System, General Electric Company, Wisconsin.

[83] M. Eldrup, in *Positron Annihilation*, edited by P.G. Coleman, S. C. Sharma, and L. M. Diana, page 753, (North-Holland, Amsterdam 1982).

[84] H. Ikari and K. Fujiwara, J. of the Phys. Soc. Japan **46**, 92(1979).

[85] E. Merzbacher, *Quantum Mechnics*, Chapter 16, (John Wiley & Sons, 1970).

[86] A. P. Mills, Jr. and C. A. Murray, Appl. Phys., **21**, 323(1980).

[87] T. McMulllen, in the Proceedings of the VII International Conference on Positron Annihilation, 1985, page 657.

[88] W. Brandt and N. R. Arista, Phys. Rev. A **19**, 2317(1979).

[89] K. G. Lynn and D. O. Welch, Phys. Rev. B **22**, 99(1980).

[90] K. M. Case and P. F. Zweifel, *Linear Transport Theory*, Chapter 8, (Addison-Wesley, Reading, Massechusetts 1967).

[91] D. A. Mcquarrie, *Statistical Mechanics*, chapter 20, (Harper & Row Publisher, New York 1976).

[92] K. G. Lynn, B. Nielsen, and J. H. Quateman, Appl. Phys. Lett. **47**, 239(1985.

[93] I. K. MacKenzie, J. A. Eady, and R. R. Ginerich, Phys. Lett. A **33**, 279(1970).

[94] J. L Campbell, Appl. Phys., **13**, 365(1977).

[95] P. J. Schultz, R. W. Ollerhead, P. C. Lightenberger, B. G. Nickel, J. R. Macdonald, and I. K. MacKenzie, Can. J. Phys., **59**, 325(1981).

[96] H. L. Au, P. Asoka-Kumar, B. Nielsen, and K. G. Lynn, J. Appl. Phys., **73**, 2972(1993).

[97] G. F. Knoll, *Radiation Detection and Measurement*, second edition, chapter 3, (John Wiley & Sons, 1989).

[98] B. E. Deal and J. M. Early, J. Electrochem. Soc., **126**, 20c(1979).

[99] A. Ourmazd, D. W. Taylor, J. A. Rentschler, and J. Bevk, Phys. Rev. Lett., **59**, 213(1987).

[100] S. M. Goodnick, D. K. Ferry, C. W. Wilmsen, Z. Liliental, D. Fathy, and O. L. Krivanck, Phys. Rev. B **32**, 8171(1985).

[101] A. H. Carim, M. M. Dovek, C. F. Quate, R. Sinclair, and C. Vorst, Science, **237**, 630(1987).

[102] W. J. Kaiser, L. D. Bell, M. H. Hecht, and F. J. Grunthaner, J. Vac. Sci. Technol., **A6**, 519(1988).

[103] P. O. Hahn and M. Henzler, J. Vac. Sci. Technol., **A2**, 574(1984).

[104] M. Henzler and P. Mariechoff, J. Vac. Sci. Technol., **B2**, 346(1984).

[105] D. E. Aspnes and J. B. Theeten, J. Electrochem. Soc., **127**, 1359(1980).

[106] R. A. Cowley and T. W. Ryan, J. Phys. D **20**, 61(1987).

[107] R. Flitsch and S. I. Raider, J. Vac. Sci. Technol., **12**, 305(1975).

[108] M. H. Hecht, F. J. Grunthaner, P. Pianetta, L. J. Johanssonn, and I. Lindau, J. Vac. Sci. Technol., **A2**, 584(1984).

[109] J. M. Hill, D. G. Boyce, C. S. Fadley, L. F. Wagner, and F. J. Grunthaner, Chem. Phys. Lett., **44**, 225(1976).

[110] M. F. Hochella, Jr. and A. H. Carim, Surf. Sci. Lett., **197**, L260(1988).

[111] C. M. Garner, I. Lindau, C. Y. Su, P. Pianetta, and W.E. Spicer, Phys. Rev. B **19**, 3944(1979).

[112] G. Hollinger and F. J. Himpsel, Appl. Phys. Lett., **44**, 93(1984).

[113] W. Braun and H. Kuhlenbeck, Surf. Sci., **180**, 279(1987).

[114] B. Nielsen, K. G. Lynn, Y. C. Chen, and D. O. Welch, Appl. Phys. Lett., **51**, 1022(1987).

[115] P. Asoka-Kumar, K.G. Lynn, T. C. Leung and B. Nielsen, Phys. Rev. B **44**, 5885(1991).

[116] E. H. Poindexter, E. R. Ahlstrom, and P. J. Caplan, in *The Physics of SiO_2 and its Interface*, edited by S. T. Pantelides, page 227, (Pergamon, New York 1978).

[117] K. L. Brower, Appl. Phys. Lett., **43**, 1111(1983).

[118] E. H. Poindexter, P. J. Caplan, B. E. Deal, and R. R. Razouk, J. Appl. Phys., **52**, 879(1981).

[119] F. Herman, Phys. Rev., **93**, 1214(1954).

[120] J. R. Chelikowsky and M. L. Cohen, Phys. Rev. B **14** 556(1976).

[121] T. O. Sedgwick, J. A.Aboaf, and S. Krongelb, IBM J. Res. Develop., **14**, 2(1970).

[122] W. E. Spicer, I. Lindau, P. Skeath, and C. Y. Su, J. Vac. Sci. Technol., **17**, 1019(1980).

[123] H. H. Wieder, J. Vac. Sci. Technol, **19**, 831(1981).

[124] E. H. Nicollian and J. R. Brews, *MOS (Metal-Oxide-Semiconductor) Physics and Technology*, (Hohn Wiley & Sons, 1982).

[125] M. M. Atalla, in *Properties of Elemental and Compound Semiconductors*, volume 5, edited by H. Gatos, page 163, (Wiley-Interscience, New York 1960).

[126] J. R. Monkowski, R. E. Tressler, and J. Stach, J. Electrochem. Soc., **125**, 1867(1978).

[127] R.J. Archer, J. Electrochem. Soc., **104**, 619(1957).

[128] S. Tolansky, *Surface Microtopography*, (Interscience, New York 1960).

[129] C. J. Frosh and L. Derrick, J. Electrochem Soc., **104**, 547(1957).

[130] J. A. Hoerni, IRE Electron Devices Meeting, Washinton, D.C., 1960.

[131] R. Krause, K. Saarinen, P. Hautojärvi, A. Polity, G. Gärtner, C. Corbel, Phys. Rev. Lett., **65**, 3329(1990).

[132] F. J. Grunthaner and J. Maserjian, IEEE Trans. Nucl. Sci. NS-24, 2108(1977).

[133] F. J. Grunthaner, P. J. Grunthaner, R. P. Vasquez, B. F. Lewis, J. Maserjian, and A. Madhuhar, J. Vac. Sci. Technol., **16**, 1443(1979).

[134] F. J. Grunthaner, P. J. Grunthaner, R. P. Vasquez, B. F. Lewis, and J. Maserjian, Phys. Rev. Lett., **43**, 1683(1979).

[135] F. J. Grunthaner, B. F. Lewis, N. Zamini, and J. Maserjian, IEEE Trans. Nucl. Sci. NS-27, 1640(1980).

[136] F. Herman, J. P. Batra, and V. Kasowshi, in *The Physics of SiO_2 and Its Interfaces*, edited by S. T. Pantelides, page 333, (Pergamon Press, New York 1978).

[137] B. E. Deal, J. Electrochem. Soc., **121**, 198C(1974).

[138] B. E. Deal, J. Electrochem. Soc., **127**, 979(1980).

[139] C. M. Svensson, in *The Si-SiO_2 System*, edited by P. Balk, page 221, (Elsevier, Amsterdam 1988).

[140] E. H. Poindexter, Semicond. Sci. Technol. **4**, 961(1989).

[141] L. O. Roellig and T. M. Kelly, Phys. Rev. Lett., **15**, 746(1965).

[142] L. O. Roellig and T. M. Kelly, Phys. Rev. Lett., **18**, 387(1967).

[143] C. V. Briscoe, S. J. Choi, and A. T. Stewart, Phys. Rev. Lett., **20**, 493(1968).

[144] P. Asoka-Kumar and K. G. Lynn, 'Characterization of Defects in Si and SiO_2-Si Using Positrons in ref.[7], page659.

[145] V. I. Goldanskii and A. P. Prokopev, *Ž. Ėksp. Teor. Fiz. Pis'ma Red.*, **4**, 422(1966).

[146] H. Lefevre and M. Schulz, in *The Si-SiO_2 System*, edited by P. Balk, page 273, (Elsevier, Amsterdam 1988).

[147] T. C. Leung, Z. A. Weinberg, P.Asoka-Kumar, B. Nielsen, G. W. Rubloff, and K. G. Lynn, J. Appl. Phys., **71**, 530(1992).

[148] M. Clement, J. M. M. de Nijs, A. van Veen, H. Schut, and P. Balk, preprint,1995.

[149] *Gallium Arsenide*, edited by J. S. Blackemore, (AIP, New York 1987).

[150] V. M. Goldschmidt, Trans. Faraday Soc., **25**, 253(1929).

[151] M. E. Straumanis and C. D. Kim, Acta. Crystallogr., **19**, 256(1965).

[152] E. D. Pierron, D. L. Parker, and B. McNeely, Acta. Crystallogr., **21**, 290(1966).

[153] C. A. Coulson, L. R. Redei, and D. Stocker, Proc. R. Soc. London, **270**, 357(1962).

[154] N. N. Sirota, in *Semiconductors and Semimetals*, volume 4, edited by R. K. Willardson and A. C. Beer, page 35, (Academic, New York 1968).

[155] F. Herman, J. Electron, **1**, 103(1955).

[156] F. Herman, Phys. Rev., **95**, 847(1954).

[157] F. Herman, Proc. Inst. Rad. Engr, **43**, 1703(1955).

[158] C. S. Wang and B. M. Klein, Phys. Rev. B **24**, 3393(1981).

[159] M. L. Cohen and T. K. Bergstresser, Phys. Rev., **141** 789(1966).

[160] F. H. Pollak, C. W. Higginbotham, and M. Cardona, J. Phys. Soc. Jpn. Suppl., **21**, 20(1966).

[161] J. Chelikowsky and M. L. Cohen, Phys. Rev. Lett., **31**, 1582(1973).

[162] K. C. Pandey and J. C. Phillips, Phys. Rev. B **9**, 1522(1974).

[163] D. D. Sell, H. C. Casey, and K. W. Wecht, J. Appl. Phys., **45**, 2650(1974).

[164] H. C. Casey, D. D. Sell, and K. W. Wecht, J. Appl. Phys., **46**, 250(1975).

[165] M. B. Panish and H. C. Casey, J. Appl. Phys., **40**, 163(1969).

[166] M. D. Sturge, Phys. Rev., **127**, 768(1962).

[167] J. L. Shay, Phys. Rev. B **2**, 803(1970).

[168] Y. P. Varshini, Physica, **34**, 149(1967).

[169] C. D. Thurmond, J. Electrochem. Soc., **122**, 1133(1975).

[170] M. J. Puska, J. Phys. C **1**, 7347(1989).

[171] J. Mäkinen, S. Palko, J. Martikainen, and P. Hautojärvi, J. Phys. Condens. Matter 4, L503(1992).

[172] R. E. Bell and R. L. Graham, Phys. Rev., **90**, 644(1953).

[173] L. A. Page, M. Heinberg, J. Wallace, and T. Trout, Phys. Rev. Lett., **98**, 206(1955).

[174] S. Tanigawa, 'Electronic Structure in Semiconductors Studied by Two Dimensional Angular Correlation of Positron Annihilation Radiation' in the Proceedings of the 9th International Conference on Positron Annihilation, edited by Zs. Kajcsos and Cs. Szeles, page 493, (Trans Tech Publications Ltd, 1992).

[175] M. Hasegawa and T. Chiba, private communication, 1995.

[176] K. Saarinen, S. Kuisma, P. Hautojärvi, C. Corbel and C. LeBerre, Phys. Rev. Lett., **70**, 2794(1993).

[177] See for example in ref[64], chapter 30.

[178] R. A. Smith, *Semiconductors*, second edition, Chapter 3, (Cambridge University Press, 1978).

[179] C. Corbel, M. Stucky, P. Hautojärvi, and P. Moser, Phys. Rev. B **38**, 8192(1988).

[180] J. Mäkinen, C. Corbel, P. Hautojärvi, P. Moser, and F. Pierre, Phys. Rev. B **39**, 10162(1989).

[181] R. Krause, K. Saarinen, P. Ilautojärvi, A. Polity, G. Gärtner, and C. Corbel, Phys. Rev. Lett., **65**, 3329(1990).

[182] S. Tüzemen and M. R. Brozel, Appl. Surf. Sci., **50**, 395(1991).

[183] J. Jiménez, A. Avvárez, J. Bonnafé, and L.I. Murin, Phys. Rev. B **39**, 13310(1989).

[184] M. O. Manasreh, D. W. Fischer, and W. C. Mitchel, Phys. Stat. Sol. (b), **154**, 11(1989).

[185] Z-Q. Fang and D. C. Look, Appl. Phys. Lett., **59**, 48(1991).

[186] D. C. Look, in *Semiconductors and Semimetals*, **38**, 91(1993).

[187] J. Dabrowski and M. Scheffler, Phys. Rev. B **40**, 10391(1989).

[188] K. Laasonnen, M. Alatalo, M. J. Puska, and R. M. Nieminen, J. Phys.: Condens. Matter, **3**, 7217(1991).

[189] K. Laasonen, R. M. Nieminen, and M. J. Puska, Phys. Rev. B **45**, 4122(1992).

[190] B. K. Panda, Phys. Rev. B **49**, 2521(1994).

[191] M. Saito, A. Oshiyama, and S. Tanigawa, Phys. Rev. B **44**, 10601(1991).

[192] L. Gilgien, G. Galli, F. Gygi, and R. Car, Phys. Rev. Lett., **72**, 3214(1994).

[193] J. M. Gibson and D. W. Dong, J. Electrochem. Soc., **127**, 2722(1980).

[194] S. Logothetidis and S. Boultadakis, J. Appl. Phys. **78**(9), 5362(1995).

[195] K. J. Malloy and K. Khachaturyan, in *Semiconductors and Semimetals*, **38**, 235(1993).

[196] J. Mäkinen, T. Laine, K. Saarinen, P. Hautojärvi, C. Corbel, V. M. Airaksinen, and P. Gibart, Phys. Rev. Lett., **71**, 3154(1993).

[197] C. D. Beling, R. I. Simpson, M. Charlton, F. M. Jacobson, T. C. Griffith, P. Moriarty, and S. Fung, Appl. Phys., A **42**, 111(1987).

[198] Y. Y. Shan, H. L. Au, C. C. Ling, T. C. Lee, B. K. Panda, S. Fung, C. D. Beling, Y. Y. Wang, and H. M. Weng, Appl. Phys., A **59**, 259(1994).